
GFD3E peptide self-assembling
and functionalization with silver
nanoparticles. Experimental and
theoretical approach.

Master thesis
Andreu Mor Maldonado

Aalborg University
Department of Materials and Production



AALBORG UNIVERSITY

STUDENT REPORT

**Fifth year at Faculty of
Engineering and Science**

Nanobiotechnology

Skjernvej 4A

9220 Aalborg

<http://www.mp.aau.dk/>

Title:

GFD3E peptide self-assembling and functionalization with silver nanoparticles. Experimental and theoretical approach.

Project:

Master thesis

Project period:

September 2020 - June 2021

Project group:

5.319B

Group members:

Andreu Mor Maldonado

Supervisors:

Leonid Gurevich

Peter Fojan

Abstract:

Short self-assembling peptides have been found to have a vast range of possibilities that goes from being part of the nanoelectronics revolution to targeted antimicrobial therapy. In this project a new amphiphilic peptide is proposed to be part of these group of this new trend. F-moc GFD3E (Glycine-Phenylalanine-Aspartic acid-Phenylalanine-Aspartic acid-Phenylalanine-Glutamic acid) capability to self assemble was tested by coarse grain MD simulations and experimentally. Aggregates were seen in the MD simulations but only in the experimental approach amyloid fibers ordered in a ribbon-like manner and of around 15 nm height were detected. Circular Dichroism, AFM visualization and Fluorescence spectroscopy were used to characterize the GFD3E amyloid fibers. A possible silver functionalization of the GFD3E fibers was studied again, by computational methods (quantum chemical simulation and calculations) and experimentally. The calculations indicate a mainly electrostatic nature between the carboxylic acid of the aspartic and glutamic acid and a silver cation. Different approaches were tried in order to silver-coat the amyloid fibers. No single fiber was found to be fully coated, but a large number of aggregates were found in both AFM and SEM images.

PREFACE

This Master's thesis has been written by Andreu Mor Maldonado a student of the master's program from Aalborg University on Nanobiotechnology. The project has been done through the last year of studies, from 02-9-2020 to 03-6-2021.

This project focus on peptide self-assembly and peptide functionalization, two topics that are increasing in relevance in science in the last years due to the challenge of miniaturizing electronic devices and designing medical therapy safer for the human body but still as aggressive towards infectious pathogens. In this frame-work, a new peptide is proposed as a candidate to work in either field. From design of the peptide going through computational simulations and experimental research, all these topics are covered in this project for both the self-assembling characterization as well as for the functionalization of the amyloid fibers obtained. The designed peptide in this project (GFD3E) is designed to be able to conduct electricity through its aromatic rings and to have three anchoring points to interact with metals, being those the carboxylic acid of the side chain of residues aspartic and glutamic acid.

Files used in this project for the all simulations (MD and QM) and quantum calculations can be seen in Files link (https://github.com/AndreuMor/Master_Thesis.git).

For last, this project was made with the kind help of master's students Cecilie Fynbo with whom many evenings had been share fabricating the nanoelectrodes and who invested her time taking SEM images of the samples; and Tami Israeli who together with Serafin Piñol Roma helped on discussing the doubts arose along the project. Not less merit should have Andrei Buglak, who cordially answered all doubts arose for the quantum chemical computation. To all of them who kindly help in moving this project forward.

Aalborg University, June 2, 2021



Andreu Mor Maldonado

Author 1

<Amorma19@student.aau.dk>

LIST OF ABBREVIATIONS

AFM	Atomic Force Microscopy
amu	Atomic Mass Unit
AO	Atomic Orbital
BCP	Bond Critical Point
CDA	Charge Decomposition Analysis
CG	Coarse Grain
CGTO	Contracted Gaussian Type Orbitals
CP	Critical Point
CP-AFM	Conductive Probe Atomic Force Microscopy
CPCM	Conductor-like Polarizable Continuum Model
DFT	Density Functional Theory
Fmoc	Fluorenylmethyloxycarbonyl
GGA	General Gradient Approximation
GFD3E	Gly-Phe-Asp-Phe-Asp-Phe-Glu (three letters code)
GTO	Gaussian Type Orbitals
HF	Hartree-Fock
HFIP	Hexafluoroisopropanol
HOMO	Highest Occupied Molecular Orbital
KS	Kohn-Sham
LB	Lysogeny Broth
LCAO	Linear Combination of Atomic Orbitals
LDA	Localized Density Approximation
LOL	Localized Orbital Locator
LUMO	Lowest Occupied Molecular Orbital
MO	Molecular Orbital
MD	Molecular Dynamics
OPDOS	Overlap Partial Density of States
PDOS	Partial Density of States
PGTO	Primitive Gaussian Type Orbitals
QAIM	Quantum Atoms In Molecules
QM	Quantum Mechanics
RDF	Radial Distribution Function
RMSD	Root Mean Square Deviation
SASA	Solvent Accessible Surface Area
SEM	Scanning Electron Microscope
SCF	Self-Consistent Field
STO	Slater Type Orbitals
TDOS	Total Density of States

CONTENTS

Preface	ii
1 Introduction	2
1.1 Self-assembling systems	4
1.2 Metal coating of peptide-based structures	9
1.3 Computational chemistry	18
1.4 Molecular Dynamics simulations	24
2 Materials and Methods	28
2.1 Computational methods	29
2.2 Peptide synthesis	31
2.3 High Pressure Liquid Chromatography (HPLC)	31
2.4 Circular Dichroism	32
2.5 Atomic Force Microscopy	32
2.6 Emission spectrometry	32
2.7 Ag functionalization of GFD3E fibers	33
3 Results	35
3.1 Molecular dynamics simulations	35
3.2 COO ⁻ -Ag ⁺ QM molecular simulation	48
3.3 High Pressure Liquid Chromatography	57
3.4 Circular Dichroism	57
3.5 Fluorescence spectroscopy	59
3.6 Atomic Force Microscopy	61
3.7 Silver coating of GFD3E nanofibers	67
4 Discussion	77
4.1 GFD3E as a self-aggregating peptide	77
4.2 Silver functionalization of GFD3E fibers	81
5 Conclusion	86
Bibliography	88
A Appendix	95
A.1 LCAO of a two electron system described by two basis functions	95
A.2 Role of electron density in DFT	97
A.3 Hartree-Fock: Slater determinant	99
A.4 Adiabatic Connection and Hybrid functionals	100
A.5 QMMM orbital interaction analysis	101
A.6 GFD3E synthesis worklist	118
A.7 AFM images of quartz wafers used for solid state fluorescence spectroscopy	120
A.8 Device preparation	120

INTRODUCTION

Today's world is demanding smaller and smaller electronic devices which can be used in the world of nanoelectronics or biosensing among others. In order to fabricate these devices traditional methods fall short regarding reproducibility not mention that they increase its complexity and become prohibitively expensive as size is reduced. New strategies to build electronic devices at the nanoscale have been studied, and organic molecules seem to be a promising alternative [1]–[3]. Some of these naturally existing organic molecules can self-assemble into nanometric structures providing a stable scaffold for the fabrication of nanoscopic materials, such as nanowires. The use of biomolecules in nanoscale fabrication not only will provide stable scaffolds but also molecular recognition and increased stability of the materials. Molecules often used to decorate these self-assembled organic structures are metals, so most of the trials done so far aimed for the fabrication of conductive nanowires or antimicrobial structures with an increased specificity regarding cell targeting [4].

Research on the use of self-assembling organic molecules as scaffold for metal nanostructures synthesis has been quite large. Moving the focus more to the topic of this project; both, small self-assembling peptides and fairly large oligomers, have been used to grow metal nanostructures on them. Thomas Scheibel and co-workers, for example, used a modification of the Sup35 protein from *Saccharomyces cerevisiae* (NM peptide) that proved to self-assemble in β -sheet fibers to create gold and silver nanowires approximately 100 nm wide [5]. This, together with studies conducted by D. Gottlieb and T. Guterman represent an example of the use of bio-inspired peptides as scaffold for the fabrication of metal nanowires [6], [7]. D. Gottlieb et al used a collagen-like peptide as scaffold for the growth of gold nanowires. Their strategy was different from the others in the way that they first incubated the peptide with gold ions and then, once the metal had conjugated with the peptide, they started the self-assembling process to end up with a continuous wire coated with gold atoms. Other studies have used completely synthetic peptides, designed for an easy self-assembling process [8]–[12]. These peptides are rather small, not exceeding the 8 residues and contain hydrophobic and hydrophilic regions to help the self-assembling process while keeping the complex soluble in polar solvents. They can also contain charged residues that will serve as anchoring points for the metal ions.

The interaction between metals and amino acids (ligands) has been poorly characterized since the vast majority of the studies done so far focused on the experimental rather than in the theoretical part. Nonetheless some research can be found where Ab initio calculations has been performed in order to shine some light on the interactions between the amino acid and the metal atoms [13]–[15]. The complexity of such interaction is notable. Crystall field theory (that describes the break of degeneracy of the d orbitals when ligands are incorporated into the system) and the Valance-bond model (that roughly states that electrons from the ligand are placed in the valance orbitals of the metal) fall short on describing the properties of the coordination complexes,

specially regarding transition metals. A new theory was required to fully describe these interactions. The Ligand field theory combines the two above-mentioned theories with the Molecular Orbital theory (that describes how the combination of different atomic orbitals leads to the formation of completely new molecular orbitals) and allow a better understanding of these complexes and predict their properties such as paramagnetism or fluorescence. Quantum-chemistry software such as ORCA, MOPAC and Multiwfn among many others, can describe with fairly good accuracy these transition metals-amino acids interactions, and others, and are used to theoretically describe the properties of these complexes [13]–[15].

These hybrid materials are thought to be a key part for the development of nanoelectronics since they have been proved to conduct electricity. If the coating is continuous, a conductivity similar to that reported for metal nanowires should be expected due to its structural similarity but, if there are areas uncovered by metal atoms or even thin vacuum gaps, the conductivity will be dominated by tunneling steps between metal-rich areas and then a more complex model will be needed to describe the conductivity. Hence, coverage of the peptide is rather important for the conductivity of the complexes. This has been observed by Acar et al, where different surface potentials were measured along the gold-coated fibers, implying that the percolation point had not been reached. Further study on the assemblies with and without gold nanoparticles suggested that the low conductivity values observed on the pristine peptide fibers may be due to the presence of ions in the solvation shell around the peptide, since the measurements showed a difference of around 10^6 units in conductivity between pristine and gold decorated fibers [9]. Gottlieb et al demonstrated that the collagen-like peptide coated with silver had indeed conductivity, which not at first but after a given number of cycles (15 cycles in their study) can be characterized as ohmic. They justified this change of behaviour on the annealing effect of the cycles over the metal clusters, reducing the impurities on both the bulk and the extremes of the metal wire [6]. Again, proving that coverage is pivotal for conductivity characteristics of the complex, the I-V curve observed at low levels of cycles was characteristic of the presence of electron tunneling regime governing the conductivity. Another study, where the difference in conductivity as well as the importance of coverage can be seen, is in Guterman gold coated fibers. There, through a conductive-tip AFM analysis (CP-AFM) was seen that big difference in resistance was achieved based on how much metal coverage the fibers had, to the point of almost no conductivity at all for pristine fibers. Furthermore, the densely decorated fibers showed an increase of conductivity with a decrease on temperature, indicating a metal-like charge conductivity [7].

Not only conductivity enhancement has been seen when peptide fibers has been decorated with metal nanoparticles. Antimicrobial activity, most likely due to interaction with bacterial membranes, has also been reported. Pazos and coworkers studied the effect of metallized peptide nanofibers on bacterial growth introducing these complexes into the LB medium inoculated with *E. coli*. The optical density of the cultures showed a reduction on growth only when the metallized fibers were introduced not when the pristine fibers were used for the analysis. Furthermore, they tested the toxicity against eukaryotic cells with a mice myoblast cell line (C12C12 cells). The use of these decorated fibers proved to be less toxic to eukaryotic cells than the use of AgNPs alone [10].

The aim of this project is to synthesize a seven amino acid peptide (Fmoc-GFD3E: Fmoc-Gly-Phe-Asp-Phe-Asp-Phe-Glu). This peptide has been designed to self-assemble into β -fibers and to have a strong π - π interactions as an attempt to make it conductive. The fibers formed by GFD3E will be coated with silver atoms in order to create a continuous metal wire of nanometers in diameter. Structural as well as functional

properties will be analyzed with further focus on the conductivity of both the pristine and decorated fibers. Molecular dynamics as well as quantum chemistry simulations and calculations will be performed in order to better understand the interaction of silver atoms with the amino acids, and how these interactions will affect the overall system.

1.1 Self-assembling systems

Self-assembly is a naturally occurring phenomenon for which simple molecules associate in a higher order structure. The process of self assembly has been defined in very different ways, most of them disagreeing in whether the use of an external force is understood as self-assembling or not. Here, the definition given in the book *Self Assembly. The science of things that put themselves together* [16]. It follows as "*spontaneous formation of organized structures through a stochastic process that involves pre-existing components, is reversible and can be controlled by proper design of the components, the environment and the driving force*". The study of self-assembling processes has attracted attention from very different scientific fields. Biologists have been interested in the study of how nature produce these organized complexes almost effortlessly; chemists and engineers have focused on the design of new components capable of self-assembly ranging from the macro to the nanometer scale and mathematicians together with computer scientists have studied self-assembly in order to create models that will help understanding and designing new self-assembling systems. Because giving a proper and in deep explanation of what self-assembly is would require a whole book by itself, a few ideas will be given in this report in order to help the lector understand the formation of the GFD3E fibers.

A good point to start is by describing each of the components found in every self-assembling system, these are four: particles, environment, driving force and binding force. The first component to be described are the particles. In order to lead to a self-assembling process and not a simpler aggregation, particles that self-assemble must possess some special characteristics that will be specific for each one of the components of the system mentioned above. These particles may have an internal complex organization without which the process of self-assembling won't be possible. This is the reason why often particles that will self-assemble are named as *Structured particles*. Bringing this concept to the more familiar field of peptide self-assembly. If the protein/peptide is understood as the self-assembling particles, then these are organized particles composed by smaller particles (amino acids) the nature of which will play a key role on determining the final structure of the complex. Furthermore, these structured particles may require a modification, being a conformational or a structural change before they can self-assemble into larger systems.

Continuing with the other component that can be designed, this is the environment in which the self-assembling process occurs. It is obvious that the environment will always be present in a self-assembling and any kind of system, so its properties will have an important role on determining the organization of the final structure. Because there are a lot of different factors that can be altered modifying the environment, the importance of this component will be highlighted when describing some examples

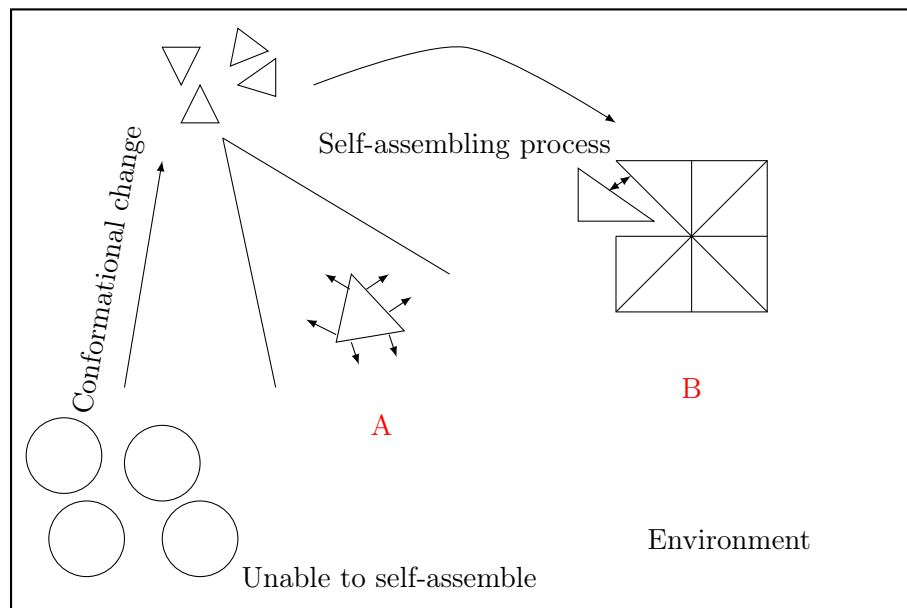


Figure 1.1: Representation of a self-assembling system, where the environment, the particles and both kinds of forces, the driving force (A) and the binding force (B) are represented.

of inorganic and organic self-assembling processes, but for the most eager lectors some traits often used to controlled self-assembly are temperature, concentration of the structured particles and other particles (for example salt), electromagnetic fields among others.

Once the components subjected to be altered in order to drive the self-assembling process towards a desired structure are described, it is the turn for the forces moving together and stabilizing the self-assembled structure. These forces cannot be changed, although the design of the particles as well as the environment can change which one of the different forces will dominate. One important characteristic to define a system as self-assembling is that the structured molecules must be placed randomly in the environment. Hence, the driving forces are those that will move the system until the structured particles are close enough for the short-range binding forces to trap them and stabilize them. An obvious driving force is the thermal noise, where by increasing the temperature of the system the motion of the molecules inside is increased. When the structured particles are close enough, the binding forces get in act. It is difficult to draw a clear line between driving and binding forces, but a honest attempt can be done by distinguishing these two kinds of forces by categorizing the binding forces as those that hold the system in a stable and ordered state. As stated above, the self-assembling process is characterize for being reversible thus, in order to maintain the system stable the binding forces must be larger than the repulsive forces. Some binding force can be the capillary force or meniscus forces. The capillary force is caused by the condensation of liquid (often water) in the meniscus formed by two hydrophilic particles interacting with a hydrophobic surface. Another example would be the Van der Waals forces which are attractive forces between two charged particles or the steric and depletion interaction, the latest tightly related to the properties of the solvent. Again, as a reminder to the lector, the properties of the structured particles will dictate what kind of binding forces will dominate [16], [17].

The process of self-assembling can be classified into three different groups. Those are: static, dynamic and programmed self-assembly. Their description is trivial. Starting from the static self-assembly the system is characterized to follow an energy minimization path and when it has reached a local or global minimum, the system remains in that thermodynamic equilibrium. The dynamic self-assembly is characterized by the fact that the final structure will only be stable as long as the system is dissipating energy, otherwise the structure will break down. For a better understanding, an example will be given. Let's imagine a homogeneous solution with aluminium nanoparticles. If a voltage is applied from one extreme of the system to another, the aluminium nanoparticles will begin to aggregate in the direction of the applied voltage. Once the voltage is ceased, the nanoparticles will dissipate into the random organization they first had [16]. The dynamic self-assembly do not rely on energy minimization but in altering the properties of the structured particles so the binding forces will be larger than the repulsive ones. The last and probably the more abstract one is the programmable self-assembly. It is understood as the link between computation and self-assembly, where each of the structured particles contains information of how the self-assembly process must end, that is, based on small differences on the structured particles, different ending structures will be created leading to a sort of input-output working method as in computer science.

Different structures can be obtained from a self-assembling process, although they can be resumed to monolayers and complex organizations [18], [19]. Monolayers are formed by a single layer of atoms/molecules deposited on a substrate. The simplest design of the structured particle for it to be able to form a monolayer can be described by three different regions, a functional head that will be used to functionalize the monolayer, an anchor group that will interact with the substrate and a linker that will link these two groups. The linker, although its description seems trivial, plays an important role in determining the strength of the interaction. The higher order organizations are formed when molecules are amphiphilic, that is to present a hydrophilic and a hydrophobic group. If the solvent is hydrophilic, these molecules will maintain the hydrophilic region in contact with the solvent and will protect the hydrophobic region from the solvent. Based on how the structured particles are designed the final structure will be different.

Moving towards a more interesting part for the scope of this report, some key aspect of peptide self-assembly will proceed. Peptide self-assembly into higher order peptidic structures is not rare to find in nature in the form of globular proteins or fibrils. This self-assembly when controlled is beneficial for the growth and well-being of the cells but when it is unregulated it leads to harmful structures that are the cause of many diseases [20]–[22]. Human-designed peptide self-assembled structures have also been studied giving rise to very complicated geometries with a particular interest [23], but for the sake of simplicity only those studies who obtained a similar structure as the one obtained with Fmoc-GFD3E peptide will be analyzed and discussed. A big effort has been put on in understanding how the β -fibers are self-assembled and what forces govern this process since the formation of amyloid fibers is the main cause of Alzheimer's disease [20]. Amyloid fibers are protein aggregates, often insoluble, that consists of a cross- β structure where β -strands are arranged in an antiparallel or parallel manner and stabilized by hydrogen bonds [fig. 1.2], being the antiparallel interaction the more stable, since the centers responsible of forming hydrogen bonds are located perpendicular to one another [24]. They are characterized as unbranched filaments that based on the peptide sequence range on nanometers in diameter up

to microns in length [18]. Fibrilization can occur in two different pathways, I) each peptide nucleate from solution and II) peptide oligomers join an already formed fibril. The choice of which pathway to go when fibrilating is unknown and both of them are assumed to happen simultaneously [25]. What is well known is the structural steps to get to the β -sheet bilayer (the final ordered structure, of which the higher levels of organizations consists of repeats of this unit). Peptides begin in a conformation of extended β -strand in solution, where each side chain is oriented orthogonal to the backbone. This peptides will begin to interact with one-another leading to the formation of a stable β -sheet. These β -sheets in solution will get attracted to each other due to the hydrophobicity and/or coulomb interaction of its residues and form the β -sheet bilayer, where non-polar residues are buried inside and polar residues are in contact with the solvent [26]. The liberation of the polar residues helps in the creation of hydrogen bonds between β -sheets that will give stability to the complex what will lead to a long range order [27]. The intelligent design of these fibers can turn them from insoluble to soluble.

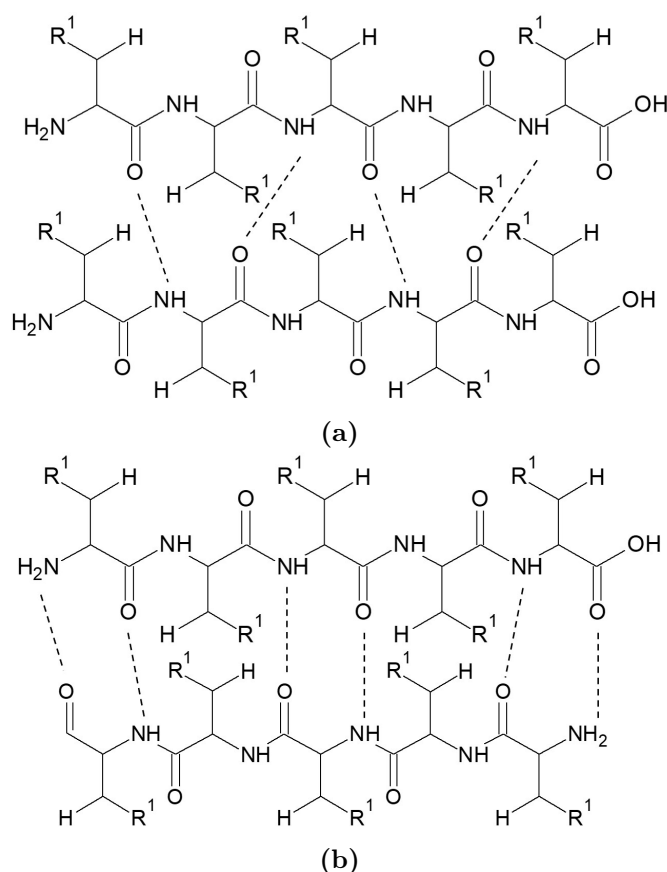


Figure 1.2: Representation of the interaction of two peptides forming a β -sheet. In a) the interaction is parallel and in b) the interaction is antiparallel. Hydrogen bonds are marked by a dashed black line. R^1 represents the side-chain of the amino acid.

The physico-chemical properties of the peptides will dictate the structure and stability of the final complex. Hydrophobicity plays an important role in aggregation. This hydrophobicity can come from non-polar residues as well as from aromatic residues

and its importance in aggregation can be seen when highly hydrophobic clusters are rarely found in naturally occurring proteins [22], [26], [28]. Hydrophobic residues will tend to protect themselves from the polar molecules in the solvent, thus moving closer the peptides in a polar solution. Hence, hydrophobic residues are not governed by a reduction on enthalpy but by a reduction on the entropy of the system [29]. When aromatic residues are present in the peptide, not only they contribute by increasing hydrophobicity but also by introducing another point of interaction, the aromatic rings. Aromatic rings will interact in what is called the π - π interactions. They, unlike only hydrophobic residues, have directional growth [30].

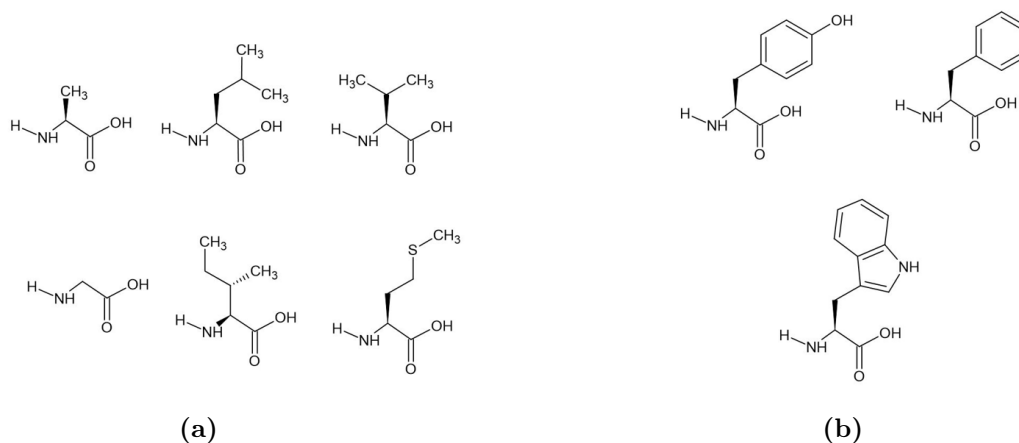


Figure 1.3: Representation of the hydrophobic and aromatic amino acids. a) hydrophobic amino acids and b) aromatic amino acids. The figures have been created with Chems sketch.

The role of aromatic residues in the self-assembling process has been studied by performing point mutations on amyloid peptides. Most of these studies have proved that aromaticity is not essential for self-assembling yet, it is an important factor that will lead to different structures [31]–[33]. An example of such a strategy is the study done by Lakshmanan and coworkers where they synthesised different fragments of naturally occurring peptides known for its implication in different diseases and studied its properties [34]. They found that that even though peptides containing aromatic residues and peptides containing only hydrophobic residues all self-assembled, the KL_7 peptide (KLVFFAE) self-assembled into more rigid *beta*-fibers most likely due to the presence of the diphenylalanine moiety. Lee and coworkers went one step further and studied the effect on the position of the aromatic residues in the peptide on self-assembly. They saw that although the overall hydrophobicity and charge of the peptides under study were the same as well as the constituents, their position inside the peptide led to notable differences in both the self-assembly process and the final morphology, concluding that the alternation of hydrophilic/hydrophobic residue in the fashion $(X - Y - X - Y)_n$ where X is any hydrophilic residue and Y and hydrophobic, led to the best results [35].

Another important property which can be controlled when designing amino acid sequence is the net charge of the peptide. A large charge of the system either positive or negative will hinder the aggregation of the peptides due to electrostatic repulsion [22], [36]. In order to increase the stability of the complex, a design where each peptide possesses both negative and positive charges will allow for attractive electrostatic

interactions which are stronger than the hydrogen bonds created between the peptide backbones [30], [37].

1.2 Metal coating of peptide-based structures

It is not new to grow metal nanoparticles on small peptides or on self-assembled peptidic structures. Some studies have been conducted both by molecular and quantum chemical simulations and experimentally to understand the nature of these interactions and the characteristics of the materials obtained.

Several successful examples can be found where different peptide sequences were tried in order to study the stability and functionality of such complexes. In general, these studies use a rather similar approach when growing the metal particles and when studying the properties and characteristics of the resulting peptide-metal complex. These techniques will be reviewed in the project.

1.2.1 Ag-peptide interaction

Transition metals are characterized by the presence of filled or partially filled d orbitals. They possess a large number of oxidation states what gives them a varied colorimetric as well as paramagnetic properties. Transition metals are known for its ability of binding with other atoms or molecules creating a complex called coordination complex. Description of these interactions is a complicated topic and to give a detailed description of it and in specific of the interaction of silver with amino acids, years of research are required, hence, a small and brief introduction of the most important ideas of ligand field theory will be done in this report. Let's begin with the first theories and how they represented a problem to explain certain properties of the coordination complexes.

Crystal Field theory

Crystal field theory advocates that ligands can be understood as point charges moving towards the metal atom, in any direction. These point charges would represent the electrons of the ligand at its corresponding valance orbitals, hence, the interaction that is being described is mainly ionic interactions. When the ligand will get close to the metal atom, the atomic orbitals of each member of the interaction will interact in such a way that some orbitals will feel a stabilization force and some will feel a destabilization force. Whether the metal orbital feels an increase (destabilization) or a decrease (stabilization) on energy will depend on how the ligand approaches the metal ion. A general case that is often used to describe this splitting of the degeneracy levels of energy of the d orbitals is the octahedral interaction (six ligands with equal energy are approaching the metal ion through the axis). The representation of such system can be seen in fig. 1.5.

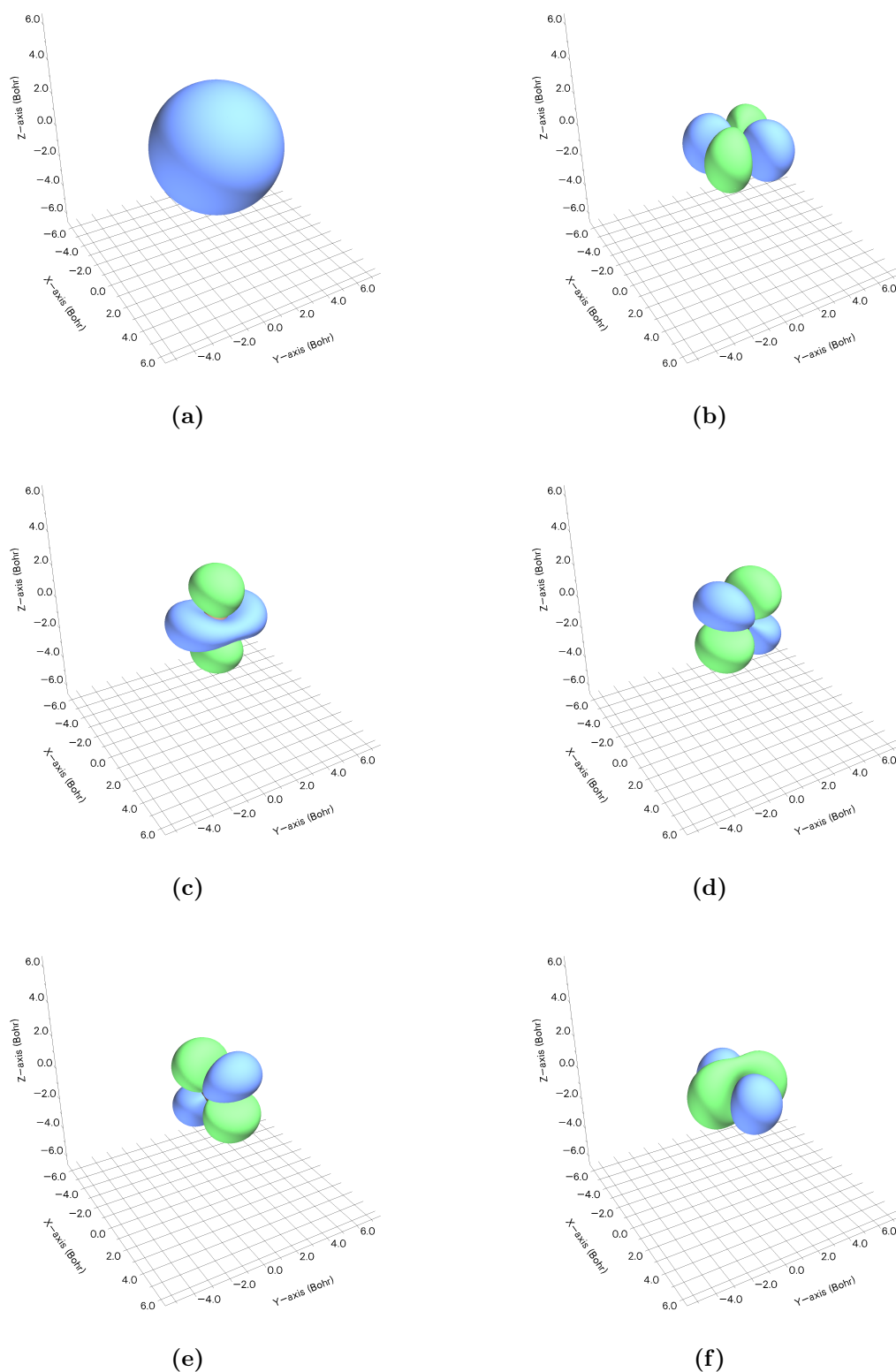


Figure 1.4: 4d and 5s orbitals representation of the silver atom. Figures were done by first performing an SCF calculation on Silver atom in ORCA and then plotting the orbitals in Multiwfn. The orbitals represented are the a) $5s$, $4d_{xy}$ in b), $4d_z^2$ in c), $4d_{yz}$ in d), $4d_{xz}$ in e) and $4d_{x^2-y^2}$ in f).

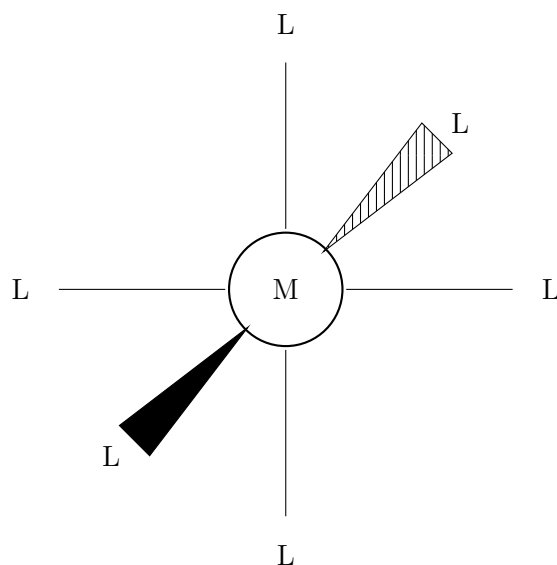


Figure 1.5: Simplification of the octahedral complex interaction between a transition metal (M) and six ligands coming from each on the axis (L).

Regarding the orbitals of the transition metal, those that have more importance are the valance orbitals (those located at the most outer shells of the atom), these are the five d orbitals (two of them are in-axis ($d_{x^2-y^2}$ and d_{z^2}) and three off-axis (d_{xy} , d_{xz} and d_{yz}) and the s orbital of a the next level of energy. A representation of the valance orbitals (five d orbitals and one s orbital) of silver atom can be seen in fig. 1.4.

In the scenario proposed in fig. 1.5, the ligands are approaching the metal atom always through the axis those orbitals that elongate through an axis will suffer and increase of the energy due to the proximity of two negative charges. The orbitals that elongate off-axis (d_{xy} , d_{xz} and d_{yz}) will see a decrease on the energy, fig. 1.6. Accounting for the energy splitting, the electrons will be placed in each orbital based on the energy required for it, since not only the orbital energy must be taken into account but also the repulsion between two electrons populating the same orbital (Pauli exclusion principle). This placement will be done as follows: first the lower energy levels will be filled with one electron (spin now is indifferent), the remaining electrons will be placed in a) lower energy levels if the energy cost of pairing two electrons with opposite spin is less than the energy cost of moving the electron to the levels at higher energy and b) to the higher energy orbitals if these levels are not very different in energy than the lower ones. The placement of electrons at the different d orbitals will lead to the wide ranging of colorimetric properties of the coordination complexes.

As stated above, Crystal field theory serves as a good approximation on how the coordination complexes behave, but is not complete since it doesn't take into account the formation of molecular orbitals upon interaction between two or more atomic orbitals. These molecular orbitals play an important role on the stability and properties of the complex but they are also difficult to describe. The best approach so far is the linear combination of atomic orbitals. This interaction and its properties is described by the Ligand Field Theory.

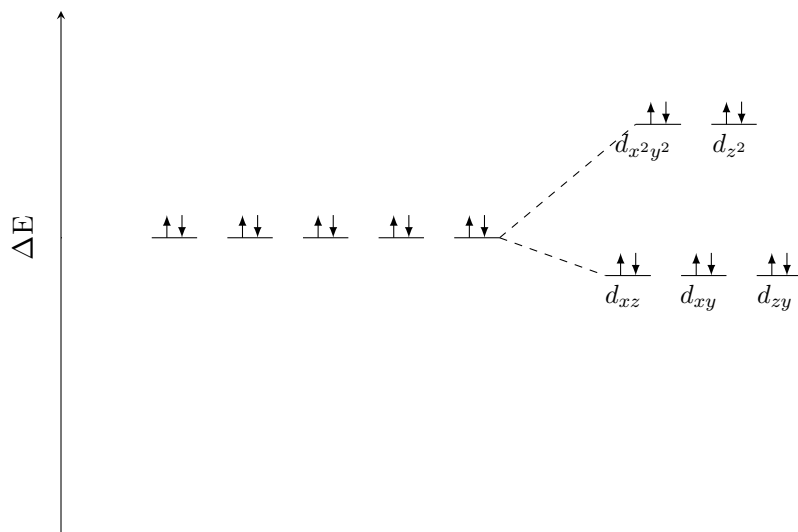


Figure 1.6: Energy diagram of the octahedral complex, where six ligands approach the transition metal from each of the axes, as represented in fig. 1.5. The diagram shows how the d orbitals lose degeneracy and those located in-axes decrease in energy but those located off-axes gain energy.

1.2.2 Ligand Field theory and Linear Combination of Atomic Orbitals

This section is based on the book *Molecular orbitals of transition metal complexes* [38] and *Quantum Chemistry* [39].

When two or more atoms are interacting together their respective atomic orbitals (AO) will feel a change in its properties and combine together to form the molecular orbitals (MO). There will be as many molecular orbitals as atomic orbitals participate in the interaction. When two AO from different atoms or molecules interact, two MOs are formed. One is responsible for the constructive interaction of these orbitals and has the name of bonding orbital (ϕ_+). Two AOs have constructive interaction when they are both in-phase [fig. 1.7]. The physical meaning of the interaction between two in-phase waves is that the probability of finding electrons between the nuclei will increase, hence, the charges of the two nuclei will be screened and the repulsion will be counteracted. At the same time, from the interaction between those two AOs another MO is formed. In this case this interaction will be destructive, since both AOs will be off-phase [fig. 1.7], and the MO formed is named anti-bonding orbital (ϕ_-). These two different MOs (bonding and anti-bonding) can be easily spotted in an energy diagram since the anti-bonding orbital will be high in energy while the bonding will be found in a lower energy state [fig. 1.8].

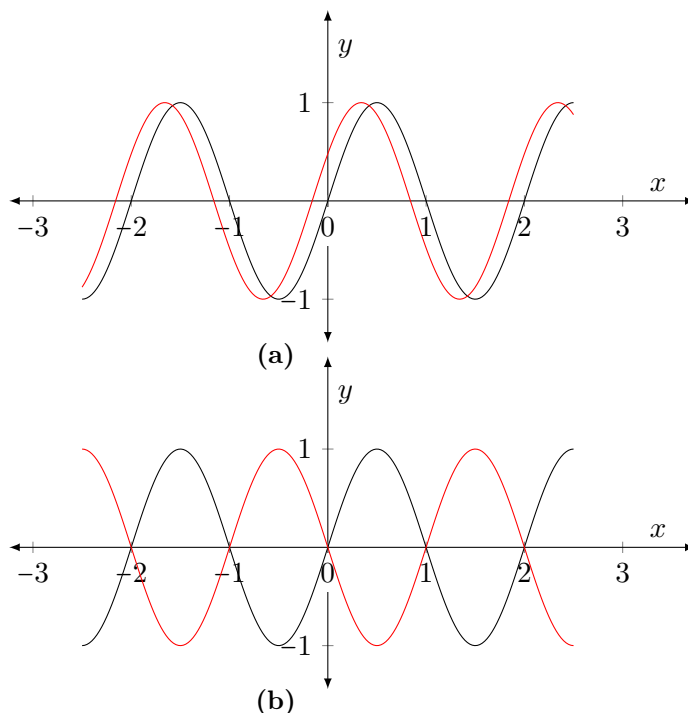


Figure 1.7: Representation of two waves in-phase a) and off-phase b). In the context of the project, a) will lead to a constructive and bonding interaction while b) will lead to a destructive and anti-bonding interaction.

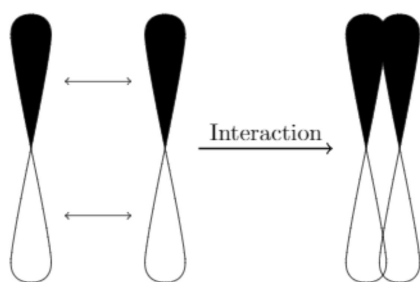
It is easy to see that two AO require some overlapping for the interaction to be done. If this overlap doesn't exist, there will be no interaction. Because of that property, the orbital geometry is rather important, and in particular the symmetry of the orbitals, since only those orbitals with the same symmetry will have constructive interactions. There are four different symmetry groups that are used to describe the valence orbitals of the transition metals. Taking into consideration only the s , p and d orbitals the symmetry groups are as follow. The s orbitals consists of an sphere and are comprised into the A_{1g} symmetry group. The p orbitals (p_x, p_y, p_z) are comprised into the T_{1u} symmetry group, an represented triply degenerated since they prolonged along the three different axis. The five d orbitals are split into two different symmetry groups. The on-axis orbitals ($x^2 - y^2$ and z^2) are represented into the E_g symmetry group, while the off-axis orbitals (xy, yz, xz) can be found in the T_{2g} group, table 1.1.

s	p_x	p_y	p_z	d_{xz}	d_{xy}	d_{yz}	d_{z^2}	$d_{x^2-y^2}$
A_{1g}	T_{1u}	T_{1u}	T_{1u}	T_{2g}	T_{2g}	T_{2g}	E_g	E_g

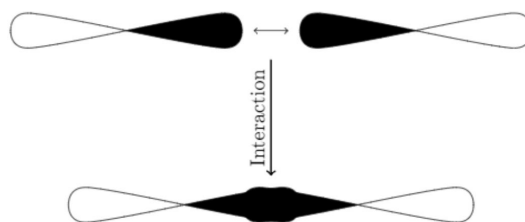
Table 1.1: Symmetry relations for orbitals from s to d .

To illustrate the effect of the symmetry on AO-AO or AO-MO interactions, the interaction between a sigma orbitals and between a sigma and a pi orbital will be used. When two sigma orbitals are close enough and appropriately orientated for them to interact, the overlapping is of the whole orbital, what will lead to a strong interaction section 1.2.2. On the other hand, when two pi orbital are close enough and appropriately orientated to interact, the overlap of these two orbitals is relatively low, leading

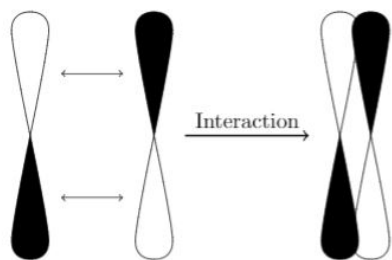
to a weaker interaction section 1.2.2. When a sigma orbital and a pi orbital want to interact, two kinds of overlapping can be seen. On one side there is overlapping of orbitals with the same symmetry and on the other side there is overlapping of orbitals with opposite symmetry section 1.2.2. This construction will lead to a destructive interaction, ergo a non-bonding orbital (molecular orbital that don't stabilize nor destabilize the complex).



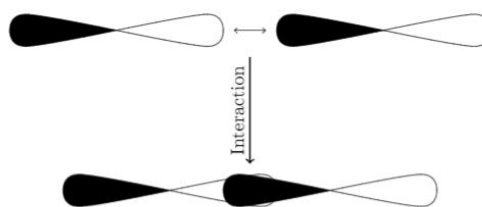
(a)



(b)



(c)



(d)

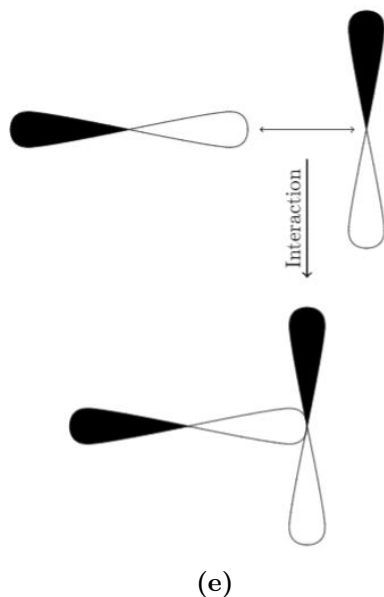


Figure 1.8: Pi-pi and sigma-sigma orbitals overlapping. As can be seen, π - π interaction occurs sideways while σ - σ interaction occurs axially, giving more stability to the complex. Interactions represented in images a) (π - π overlapping) and b) (σ - σ overlapping) will be constructive leading to bonding molecular orbitals. On the other hand, interactions represented by c) (π - π anti-symmetry overlapping) and d) (σ - σ antisymmetry overlapping) will lead to a anti-bonding molecular orbital due to the interaction of opposite symmetries. Interaction represented in e) (σ - π overlapping) will lead to the formation of a non-bonding molecular orbital.

Ligands are rarely composed of a single atom but are most likely molecules themselves, that means that the interaction metal-ligand will be composed of an interaction of atomic orbitals from the metal with molecular orbitals from the ligand. Suddenly the whole systems gets a little bit more complicated since bonding, anti-bonding and non-bonding orbitals must be included in the analysis. If this is the case, only those MOs with energies similar to the metal valance orbitals will have a major role in the interaction and so the other MOs can be ignored. Often the MOs from the ligand that fulfill this requirement are the non-bonding orbitals. The bonding orbitals often are very low on energy and the anti-bonding orbitals are very high on energy so the energy gap between the AOs from the metal and the bonding and anti-bonding MOs from the ligand is too high for them to ever interact. And if there is any interaction, this will be much weaker than for the non-bonding orbitals. Bear in mind that this may not be the case for all coordination complexes, but it is a fairly good assumption.

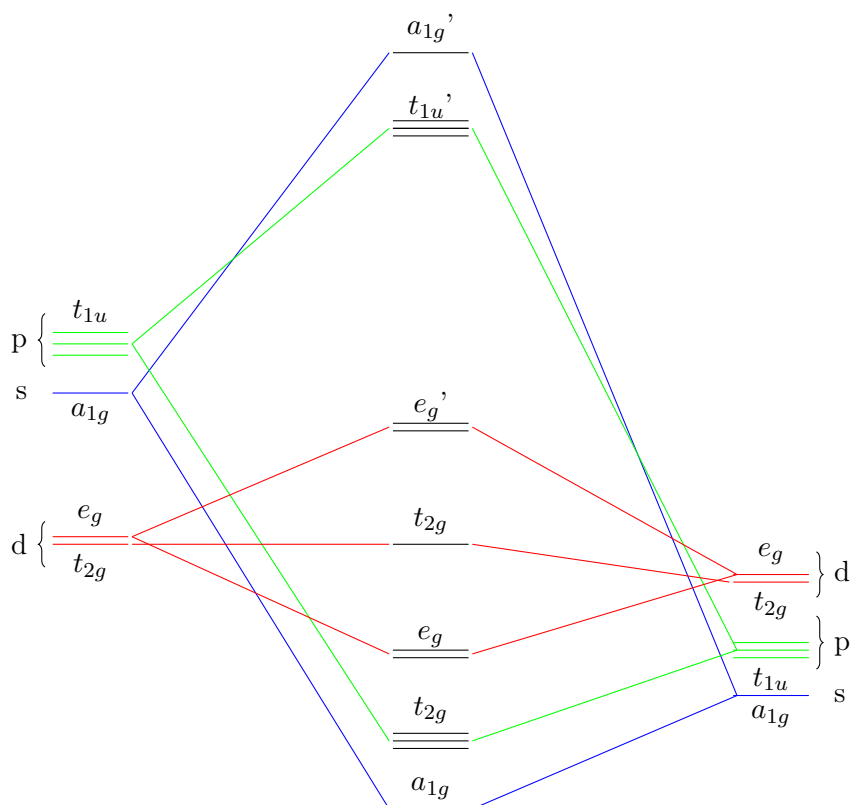


Figure 1.9: Energy diagram of the interaction of a transition metal between six ligands (all with the same energy) placed as an octahedral complex as in fig. 1.5. Each new molecular orbital is associated to its respective preceding atomic orbital by colour code: blue (s from $n+1$), green (p from $n+1$) and red (d from n). Atomic orbitals s and p from the metal (right hand diagram) are totally or partially empty of electrons (LUMO, LUMO+1).

Linear combination of Atomic Orbitals

In order to describe mathematically the construction of molecular orbitals the Linear Combination of Atomic Orbitals (LCAO) technique is required. It consists on a superposition of the atomic orbitals (described by a wave-like function and a coefficient) involved in the interaction. Each molecular is described by a linear combination of a set of approximated functions that represent atomic orbitals (basis functions) [eq. (1.1)].

$$\psi_K = \sum^K C_n \phi_i \quad (1.1)$$

where ψ_K is the wavefunction of the K molecular orbitals, C_n is the weight coefficient that determines how much influence the atomic orbital ϕ_i has.

If the Schrödinger equation is solved to know the energy of the system, the following expression is obtained

$$H\psi_K = E\psi_K \quad (1.2)$$

which integrated over all space can be turned into

$$\left| H - E | \psi_K \rangle \right| = 0 \quad (1.3)$$

ψ_K can be substituted by the expression in [eq. (1.1)] leading to

$$\left| H - E \left| \sum^K C_n \phi_i \right. \right\rangle = 0 \quad (1.4)$$

the expression above is left-multiplied by each of the atomic orbital wavefunction to obtain

$$0 = \begin{pmatrix} c_a \langle \phi_a | H - E | \phi_a \rangle & c_b \langle \phi_a | H - E | \phi_b \rangle & \cdots & c_i \langle \phi_a | H - E | \phi_i \rangle \\ c_b \langle \phi_b | H - E | \phi_a \rangle & c_b \langle \phi_b | H - E | \phi_b \rangle & \cdots & c_i \langle \phi_b | H - E | \phi_i \rangle \\ \vdots & \vdots & \ddots & \vdots \\ c_i \langle \phi_i | H - E | \phi_a \rangle & c_i \langle \phi_i | H - E | \phi_b \rangle & \cdots & c_i \langle \phi_i | H - E | \phi_i \rangle \end{pmatrix} \quad (1.5)$$

the set of equations in [eq. (1.6)] can be separated as

$$0 = \begin{pmatrix} c_a \langle \phi_a | H | \phi_a \rangle - c_a \langle \phi_a | E | \phi_a \rangle & c_b \langle \phi_a | H | \phi_b \rangle - c_a \langle \phi_a | E | \phi_b \rangle & \cdots & c_i \langle \phi_a | H | \phi_i \rangle - c_i \langle \phi_a | E | \phi_i \rangle \\ c_a \langle \phi_b | H | \phi_a \rangle - c_a \langle \phi_b | E | \phi_a \rangle & c_b \langle \phi_b | H | \phi_b \rangle - c_b \langle \phi_b | E | \phi_b \rangle & \cdots & c_i \langle \phi_b | H | \phi_i \rangle - c_i \langle \phi_b | E | \phi_i \rangle \\ \vdots & \vdots & \ddots & \vdots \\ c_a \langle \phi_i | H | \phi_a \rangle - c_a \langle \phi_i | E | \phi_a \rangle & c_b \langle \phi_i | H | \phi_b \rangle - c_b \langle \phi_i | E | \phi_b \rangle & \cdots & c_i \langle \phi_i | H | \phi_i \rangle - c_i \langle \phi_i | E | \phi_i \rangle \end{pmatrix} \quad (1.6)$$

Using the following equivalences

$$\langle \phi_a | H | \phi_a \rangle = \int \phi_a H \phi_a = H_{aa} \quad (1.7)$$

$$\langle \phi_a | H | \phi_b \rangle = \int \phi_a H \phi_b = H_{ab} \quad (1.8)$$

$$\langle \phi_a | \phi_a \rangle = \int \phi_a \phi_a = S_{aa} \quad (1.9)$$

$$\langle \phi_a | \phi_b \rangle = \int \phi_a \phi_b = S_{ab} \quad (1.10)$$

where H_{ii} and H_{ij} are the expectation value of the hamiltonian and S_{ii} and S_{ij} are the overlapping matrices (S_{ii} is equal to 1) the expression in [eq. (1.6)] can be simplified to

$$0 = \begin{pmatrix} H_{aa} - ES_{aa} & H_{ab} - ES_{ab} & \cdots & H_{ai} - ES_{ai} \\ H_{ba} - ES_{ba} & H_{bb} - ES_{bb} & \cdots & H_{bi} - ES_{bi} \\ \vdots & \vdots & \ddots & \vdots \\ H_{ia} - ES_{ia} & H_{ib} - ES_{ib} & \cdots & H_{ii} - ES_{ii} \end{pmatrix} \begin{pmatrix} c_a \\ c_b \\ \vdots \\ c_i \end{pmatrix} \quad (1.11)$$

The above matrix leads to the Secular determinant [eq. (1.12)] which when equaled to zero will lead to the different energy levels of the MOs.

$$0 = \begin{vmatrix} H_{aa} - ES_{aa} & H_{ab} - ES_{ab} & \cdots & H_{ai} - ES_{ai} \\ H_{ba} - ES_{ba} & H_{bb} - ES_{bb} & \cdots & H_{bi} - ES_{bi} \\ \vdots & \vdots & \ddots & \vdots \\ H_{ia} - ES_{ia} & H_{ib} - ES_{ib} & \cdots & H_{ii} - ES_{ii} \end{vmatrix} \quad (1.12)$$

Because the solution depends on the number of AO that are used for the description of the MO, the complexity to solve the secular determinant increases as the number of basis functions are increased. An example of a system with one electron and two basis functions (AO) is given in appendix A.1.

1.3 Computational chemistry

To calculate the electronic properties of a system the Schrödinger equation must be solved. This has been solved for a one-electron body, but the complexity escalates quickly as the number of electrons increase, so it is easy to see that when the electric properties of a molecular system are to be calculated, computational power is required and some approximations are compulsory in order to reduce the cost of it. Regarding the different software prepared to perform quantum chemistry calculations one has a larger-than-expected number of them from where to chose. The selection must be done based on the properties and size of the system to study. Said that, in this study the ORCA software was chosen to perform more accurate calculations on small systems representative of the big system. The approximations used in these software are mainly two, the Hartree-Fock (HF) approximation and the Density Functional Theory (DFT) approximation. Since DFT is more in the scope of this report, a few words will be given so the lector can get an idea of how these calculations are done, and how the LCAO is used by these software. When needed, a few words will also be given from HF approximation, since it will ease the understanding of some DFT basis sets.

1.3.1 Density Functional Theory

This section is based on [40].

DFT is built upon two principles formulated by Hohenberg and Kohn published in 1964. These two principles set the basis for one of the most used theory level in computational chemistry. These two principles, in simple words, state that the electron density has a tight relation to the hamiltonian and thus to the electrical properties of the system; and that the ground state of a system is such that will minimize the energy of the system. That means, since the energy of a system is calculated through the hamiltonian, and that can be related to the electron density; by knowing the electron density, the energy of the system can be studied; and by minimizing its energy, the ground state is found. Put down in other words, what these two principles state is that each electron in the system is affected by an electron density around it, and this electron density is different for every point in the system that is being calculated [appendix A.2]. Based on these two principles and applying the Born-Oppenheimer

approximation¹ DFT uses a variational method to find the electron density that will lead to a minimal energy of the system, and once the electron density is calculated, the geometry of the nuclei will be updated.

The energy functional is affected by the Coulomb interaction between the charged particles (nuclei and electrons), the electron anti-symmetry and the kinetic energy of the electrons, the last two being the most complicated part of the functional to compute. Hence, the energy functional used in DFT follows the same structure as the electron Hamiltonian.

$$H_{el} = T_{el} + V_{eN} + V_{ee} \quad (1.13)$$

$$E[\rho] = T[\rho] + E_{eN}[\rho] + E_{ee}[\rho] \quad (1.14)$$

In eq. (1.13) and eq. (1.14) the first term in both equations (T_{el} and $T[\rho]$) represents the kinetic energy of the electron and are calculated as a function of the electron density. The second term ($V_{eN}, E_{eN}[\rho]$) and third term ($V_{ee}, E_{ee}[\rho]$), represent the potential energy of the interaction between the nuclei and the electron and the potential energy of the interaction between electrons respectively. The equation to compute the potential energies of the interactions between the electron and the nuclei and between other electrons is fairly straight-forward.

$$E_{eN}[\rho] = \sum_A \int \frac{Z_A \rho(\mathbf{r})}{|\mathbf{R}_A - \mathbf{r}|} d\mathbf{r} \quad (1.15)$$

$$J[\rho] = \frac{1}{2} \int \int \frac{\rho(\mathbf{r})\rho(\mathbf{r}')}{|\mathbf{r} - \mathbf{r}'|} d\mathbf{r}d\mathbf{r}' \quad (1.16)$$

It is easy to see in eq. (1.15) and eq. (1.16) that the form of the potential follows the Coulomb interaction between two charged particles. Some notes must be given in order to better understand these two equations:

- $J[\rho]$ is a simplification of the repulsion energy between two electrons. Again, DFT is based on the interaction between two electron densities, so the effect of particle-particle interactions are lost. This is the reason why it has a different name and it is not described as E_{ee} .
- In $E_{eN}[\rho]$, since the position of the nuclei is known, it is only required to integrate over the electronic space. For eq. (1.16), since the position of both electron densities is unknown, a double integral is required.
- The electron density, $\rho(\mathbf{r})$, gives the average number of electrons in a given location, which will be used as an indicator of charge (appendix A.2).
- In eq. (1.16) a correction term of the form $\frac{1}{2}$ appears to account for the interaction between e_i^- and e_j^- and e_j^- and e_i^- , since both will give the same result.
- The summation in eq. (1.15) is done over all atomic nuclei.

The term that is key for the description of the energy functional and that generates more problems to describe is the kinetic energy of the electron being studied as a function of the electron density ($T[\rho]$). To describe $T[\rho]$ the most common approximation used in DFT is the Kohn-Sham approximation (KS), which introduces

¹The Born-Oppenheimer approximation states that the nuclei can be separated from the electrons when calculating electronic structures, since the mass of a nucleus is larger than that of an electron.

the concept of the "non-interacting limit". The idea behind the KS approximation is to compute as accurate as possible the exact kinetic energy of the "non-interacting" system, and then introduce a correction factor to account for these electron-electron interactions that were missing. This idea relies on that the "non-interacting system" is fairly easy to calculate, since it is done through a Slater determinant and is used in the HF [appendix A.3]. In other words, KS approximation states that first, the kinetic energy of a system where the electrons are treated as uncharged fermions that do not interact between them is calculated and over these calculations a correction with name Exchange-Correlation energy ($E_{xc}[\rho]$) is added to account for the electron-electron interaction. This last term, $E_{xc}[\rho]$, will have to be approximated by the functional of choice. Under the KS approximation, the kinetic energy term ($T^{KS}[\rho]$) of the energy functional $E^{KS}[\rho]$ is expressed as

$$T^{KS}[\rho] = -\frac{1}{2} \sum_i^N \langle \phi_i | \nabla^2 | \phi_i \rangle \quad (1.17)$$

The description of the orbitals given by eq. (1.17) is the same given in the HF approximation. The expectation value for the energy of each electron i present in an occupied molecular orbital N is obtained under the "non-interacting" framework. In order to set $T^{KS}[\rho]$ as a functional of the electron density, $\rho^{KS}(\mathbf{r})$ is described as the sum over all the electrons i in each occupied molecular orbital of the probability function of the electron [eq. (1.18)].

$$\rho^{KS} = \sum_i^N \phi_i^*(\mathbf{r}) \phi_i(\mathbf{r}) \quad (1.18)$$

where ϕ_i^* is the complex conjugate of the electron function ϕ_i .² The KS energy functional, $E^{KS}[\rho]$, will then have the following form, where all the parameters, the "non-interacting" kinetic energy and the coulomb interaction between charged particles are present and it incorporate the correction factor $E_{xc}[\rho]$ as well [eq. (1.19)].

$$E_{KS}[\rho] = T^{KS}[\rho] + E_{eN}[\rho] + J[\rho] + E_{xc}[\rho] \quad (1.19)$$

The exchange-correlation term incorporates all the information that it is unknown of the interaction between electrons in such large systems. In eq. (1.19) all terms can be computed but $E_{xc}[\rho]$.

On the KS approximation framework the variational principle must be applied to find the properties of ψ that will minimize the energy of the system.

$$H^{KS}(\mathbf{r})\psi_K(\mathbf{r}) = \epsilon_i \psi_i + K(\mathbf{r}) \quad (1.20)$$

²The complex conjugate (ϕ_i^*) of a function (ϕ_i) is created by replacing the complex part of the function i to $-i$ so when a function is multiplied by its complex conjugate, the result is the real part of the function. This applied to a wave-function means that when an electron wave-function is multiplied by its complex conjugate, the result is a real positive number as the probability should be.

The Kohn-Sham hamiltonian is very similar to that used in the HF approximation but incorporates the exchange-correlation effect as the potential of the exchange-correlation function ($V_{xc}(\mathbf{r})$).

$$H^{KS} = -\frac{1}{2}\nabla^2(\mathbf{r}) + V_{eff} \quad (1.21)$$

where V_{eff} is described as

$$V_{eff} = E_{eN} + \int \frac{\rho(\mathbf{r}')}{|\mathbf{r} - \mathbf{r}'|} + V_{xc}(\mathbf{r}) \quad (1.22)$$

The potential energy of the exchange-correlation interaction (V_{xc}) will be approximated differently based on the functional used to perform the calculations. There are a lot of different families of functionals that will approximate $V_{xc}(\rho)$ in slightly different. A description of all of them will fall far from the scope of this report, so only a description of the functional used to perform the calculations will be given.

To begin with, a representation of the general form of $V_{xc}(\rho)$ will be given. Since the form of the exchange-correlation energy is unknown, it is obvious that the form of the potential of the exchange-correlation energy is also unknown, so it is described as the functional derivative of $E_{xc}[\rho]$ with respect to the electron density [eq. (1.23)].

$$V_{xc}(\mathbf{r}) = \frac{\partial E_{xc}(\mathbf{r})}{\partial \rho} \quad (1.23)$$

As stated before, only a description of the functional family used in the study will be given. A description of other functionals can be found in [40].

Hybrid-functionals

A quick reminder for the lector. The functionals are approximations used to represent the exchange-correlation energy E_{XC} , so it can be introduced in eq. (1.23) and calculate the ψ_K , the wavefunction of the molecular orbital K with eq. (A.19) and approximate the correlation hole. This idea is based on that the two energies are independent from one-another, but when observed in real systems, specially in molecular systems rather than in atomic systems, they are dependent to each-other, ergo the approximations should be done for both of them together.

Hybrid functionals are inspired by the Adiabatic connection theory, where an interpolation between a fictional "non-interacting" system and the real system is done by introducing a factor λ . The E_{XC} is integrated over all the λ values. At $\lambda=0$, the E_{xc} is known since it belongs to the "non-interacting" system and is calculated as in the Hartree-Fock approximation. When λ is equal to one, its value is very good approximated, although in order to get such a precise approximation, a combination of functionals must be used [appendix A.4].

Let us start from a fairly good and basic approximation, and is that E_{XC} has linear dependency on λ

$$E_{XC} = \frac{1}{2}E_{XC}^{\lambda=0} + \frac{1}{2}E_{XC}^{\lambda=1} \quad (1.24)$$

As mentioned before the first term on eq. (1.24) can be exactly calculated. The complexity comes from the second term. Here, the Hybrid-functionals combine other functionals, often the Local Density Approximation (LDA) and Gradient-Corrected approximation (GGA), to approximate its value (no detailed description of each one of them will be given since it falls far from the scope of this project). Roughly speaking, LDA is a localized functional, by means that it calculates the electron density at a given point and uses it to calculate $V_{xc}(\rho)$. Because it only takes into consideration the electron density at a particular point, it overestimates the exchange energy E_x . On the other hand, GGA describes how the electron density varies by calculating the gradient of the electron density at a given point. That gives information of how the electron density behaves around the electron of reference (ρ_1), hence introducing as well the effect of the correlation energy.

1.3.2 Basis sets

This section is based on [41] and notes from Dr. C. David Sherrill.

DFT theory level is less affected by the choice of basis set than other theory levels such as HF for example. That doesn't mean the choice of basis set is trivial for the calculations accuracy, specially if particular properties such as polarization of the orbitals are to be calculated.

Recapitulating to the LCAO, a basis set is a group of basis functions that describe one-electron orbitals in order to approximate the MO wavefunctions. A good basis set should represent with the little number of basis functions as possible the system (it will reduce the computational cost) and should be representative of all elements in the periodic table, or at least of the most common ones (lanthanides and actinides are barely used). There are a lot of different basis sets that with the proper functional can lead to very precise results, although there is an important effort from physical chemists to keep improving and optimizing the basis sets so they will serve as better approximations.

Basis sets are composed by a group of basis functions describing one-electron AOs. This is done by describing a 3-D space where the calculation must be done that resembles that of the real AO. There are two types of ways of describing this 3-D space, 1)Slater-type orbitals (STO) and 2)Gaussian-type orbitals (GTO) [eq. (1.25)].

$$\phi^{STO}(x, y, z) = Nx^a y^b z^c e^{-\zeta r} \quad (1.25)$$

$$\phi^{GTO}(x, y, z) = Nx^a y^b z^c e^{-\zeta r^2} \quad (1.26)$$

Where a, b and c parameters define the angular momentum of the orbital, for s-type orbitals $a + b + c = 0$ and for p-type orbitals $a + b + c = 1$ for example. N is a normalization constant and ζ describes the extend of the radial function. STOs are more accurate than GTOs since the ζ factor is not modified by a r^2 factor. This makes

the GTOs somehow imprecise at very short or very long distances to the nuclei. That is solved by increasing the number of GTOs basis functions. Computationally wise, it is a good strategy since the STOs are rather difficult to compute, so the GTOs are mostly used in front of STOs for quantum chemistry calculations specially when moving far away from the H atom.

An easy classification of the basis sets is to use the number of basis functions they used to approximate each AO. Then if only one basis function is used, the basis set is called single zeta (SZ), if it uses two double zeta (DZ), if three TZ and so on. Often, the zeta classification applies only to the valance orbitals since those are the ones involved in the bonding situations. Core orbitals, since they are very attracted to the nuclei, can be described by little basis functions and usually are described at the SZ level, although they are often neglected when a contracted basis set is used.

Contracted Basis sets

Another way of improving the computational efficiency is to contract the orbitals to calculate, but of course this strategy comes with a price to pay in accuracy. This strategy is followed by the so-called Contracted Basis Sets. Contracting a basis set consists on taking a set of primitive basis functions, often Gaussian, named Primitive GTOs (PGTOs) and modify them [eq. (1.28)] in order to reduce the load on the basis set by creating the contracted basis functions (CGTOs) and complexity [eq. (1.29)].

$$\phi = \sum^B = c_n \phi_n^{GTO} \quad (1.27)$$

$$\kappa_\beta = \sum_{\alpha=1}^M d_{\alpha\beta} \phi_\alpha^{GTO} \quad (1.28)$$

$$\phi_{contracted} = \sum_{\beta=1}^K c_\beta \kappa_\beta \quad (1.29)$$

On the expressions above, eq. (1.27) refers to the non-contracted form of the LCAO and eq. (1.29) to the LCAO initial state with the contracted GTOs (κ_β), described in eq. (1.28). In eq. (1.28) the term $d_{\alpha\beta}$ is the contraction coefficient.

The standard notation to describe contraction on the PGTOs is represented by the primitive basis functions inside a parentheses and the contracted basis functions in square brackets. For example, the contraction form of silver orbitals used for this report is the following (7s7p6d1f)->[4s4p4d2f]. Contraction can be done in two different methods, segmented contraction and general contraction. In segmented contraction methods (def2-TVZP for example) only one or a reduced number of PGTOs (n) participate in each CGTO and seldom PGTOs are duplicated to participate in different CGTOs. This will be done uniquely to describe intermediate orbitals [eq. (1.30)].

$$\begin{aligned}\kappa_1 &= \sum^n d_\alpha \phi^{GTO} \\ \kappa_2 &= \sum^{M-n} d_\alpha \phi^{GTO}\end{aligned}\tag{1.30}$$

On the other hand, in the general contraction method all PGTOs contribute to all CGTOs but with different contraction coefficients [eq. (1.31)].

$$\begin{aligned}\kappa_1 &= \sum^M d_{\alpha 1} \phi^{GTO} \\ \kappa_2 &= \sum^M d_{\alpha 2} \phi^{GTO}\end{aligned}\tag{1.31}$$

Error-wise the general contracted method is preferable, yet, the segmented contracted basis sets are widely used due to its computational efficiency. Although DFT theory level is not very dependable on the basis set of choice, it is important to perform all calculations with the same one in order to be able to compare the results.

1.4 Molecular Dynamics simulations

This section is mainly based on books *Understanding Molecular Simulations: From algorithms to applications* [42] and *The art of Molecular Dynamic Simulation* [43].

In an MD simulation, successive configurations of the system under study are generated by integrating the Newton's laws of motion over time [eq. (1.32)]. This equation is solved by changing the position of the particles (x_i) until the properties of the system are no longer altered. Each particle in the system is given a position and a velocity (to represent a force) at the initial time of the simulation. These two values will be used by the software to start the calculations since with an initial position value and a velocity value, a prediction of the subsequent position (x_2) can be done. This has to be done since the forces affecting each particle will depend not only on its own location but also on the location of the particles around it. That means that every time a particle (an atom) moves, the forces affecting it will change. This escalates the number of forces to take into consideration to such a point that eq. (1.32) cannot be solved analytically so the *finite difference method* is used.

$$\frac{d^2 x_i}{dt^2} = \frac{F_{x_i}}{m_i}\tag{1.32}$$

The basic idea behind the *finite difference method* is to break down the motion laws into very small time steps (duration of which can be tailored to each different system) and to calculate the total force affecting each particle in the corresponding time as a vector sum of its interactions with the surrounding particles. Once the total force affecting each particle is calculated, it is considered to be constant throughout the

duration of the time step. These forces calculated on each of the particles in the system will then be used to determine the new positions and velocities. This methodology is mathematically complex and so the algorithms designed to solve it use Taylor expansions such as the ones shown in eq. (1.33).

$$r(t + \delta t) = r(t) + \delta t v(t) + \frac{1}{2} \delta t^2 a(t) + \frac{1}{6} \delta t^6 b(t) \dots \quad (1.33)$$

Different algorithms approach this Taylor series in a different way. As an example, the Verlet algorithm used to perform the MD simulation in this report will be briefly described. The Verlet algorithm is probably the most widely used due to its simple approach, although some variations as the *leap-frog* algorithm has been created. The Verlet algorithm uses the positions and velocities of the particles at time t and at time $(t - \delta t)$ to estimate the position and velocities at $(t + \delta t)$.

$$\begin{aligned} r(t + \delta t) &= r(t) + \delta t v(t) + \frac{1}{2} \delta t^2 a(t) + \dots \\ r(t - \delta t) &= r(t) - \delta t v(t) + \frac{1}{2} \delta t^2 a(t) - \dots \\ r(t + \delta t) &= 2r(t) - r(t - \delta t) + \delta t^2 a(t) \end{aligned} \quad (1.34)$$

In the Verlet scheme the velocities do not explicitly appear but can be calculated by dividing the difference in position by the time step. This algorithm requires little computational storage since only two sets of positions and one set of accelerations must be stored. Although, the addition of such a small term $\delta t^2 a(t)$ to two very large terms can lead to loss of precision. A variation of the Verlet algorithm is the *leap-frog* algorithm (used in the study). This approach differs a little from the Verlet algorithm. The Taylor expansion is truncated after the second term and the velocities do have an implicit term in the calculations. To do so, velocities are not calculated with the ones obtained at the previous time step but with the $(t - \frac{1}{2} \delta t)$ and the accelerations at time t . Using the newly calculated velocities, the new positions of the particles are estimated.

$$\begin{aligned} r(t + \delta t) &= r(t) + \delta t v(t + \frac{1}{2} \delta t) \\ v(t + \frac{1}{2} \delta t) &= v(t - \frac{1}{2} \delta t) + \delta t a(t) \\ v(t) &= \frac{1}{2} [v(t + \frac{1}{2} \delta t) + v(t - \frac{1}{2} \delta t)] \end{aligned} \quad (1.35)$$

Contrary to the rule-of-thumb of computational algorithms a good molecular dynamics algorithm not only depends on the speed, the memory and simplicity but it has to perform at high level in different aspects. The most challenging part of an MD simulation is the calculation of the forces affecting each one of the particles in the system. If no approximations are used to calculate the inter and intra molecular forces, the time required to perform these calculations escalates as N^2 (where N is the number of particles in the system). An ideal MD algorithm should calculate the forces relatively fast but also keeping the estimations as close to reality as possible. It should also allow for the use of a long time step. This is strongly related on how the forces are

calculated and how much accuracy is expected from the calculations. Longer time steps reflects on fewer evaluations of the forces affecting each particle and hence a shorter computational time. The amount of memory required will also increase, although that do not represent a problem if a small system is studied. Another aspect that is of importance when deciding which algorithm to use (specially when simulating big systems) is whether or not such algorithm is time-reversible, that means, if one is to reverse the calculated momenta of the particles, the "reversed" trajectories must agree with the previous trajectories.

1.4.1 Coarse grain models

As mentioned above, systems with large number of particles are complex to simulate. This specially affects all-atom systems, where molecules are described with all their atoms introducing a large number of degrees of freedom. This is the reason why there has been a lot of effort to come up with a strategy where the number of particles is reduced, but the properties of the molecules are unaltered. This is where the Coarse Grain (CG) models have succeeded. CG models represents fairly well the all atom structures with a group of interacting mass points named CG beads each of which corresponds to a group of atoms form the all-atom configuration (degree of coarse-graining). The process of grouping atoms into this CG beads is called mapping. Hence, the number of particles to compute is drastically reduced but the physico-chemical properties of the molecules are kept as close to reality as possible (there will always be a compromise) [44], [45].

As for the all-atom configuration, CG models must as well describe the bonded and non-bonded interactions. This is not under the scope of this report but some words will be given nonetheless. To begin with, each CG bead is assigned a number of labels that will correspond to a different physico-chemical property [45]. These labels are:

- Polarity: Polar, intermediate, apolar and charged.
- Hydrogen-bonding character: Donor, acceptor, both donor and acceptor or neither of them.
- Degree of polarizability: A scale from 1 to 5.

Bonded Interactions

Bonds and angles in a CG model can be modelled by different methods, although the most common method is the harmonic potential eq. (1.36).

$$\begin{aligned}U_{bond} &= K(r - r_0)^2 \\ U_{angles} &= K_{\theta}(\theta - \theta_0)^2\end{aligned}\tag{1.36}$$

where K is a bond constant, r is the distance between beads and r_0 is the equilibrium bond length. A similar expression will be used for the dihedral and the improper angles, with a small variation for the dihedral angles which are described by a cosine harmonic potential [44].

$$\begin{aligned} U_{dihedral} &= K_\psi [1 + \cos(n\psi - \psi_0)] \\ U_{improper} &= K_\phi (\phi - \phi_0) \end{aligned} \quad (1.37)$$

where K_ψ and K_ϕ are force constants and ψ_0 and ϕ_0 are the equilibrium dihedral and improper angles.

Non-bonded interaction

The non-bonded interactions are usually pivotal in describing some macroscopic properties and thus must be accurately described, what makes it a tedious work, since attractive and repulsive forces have an important long-range component. Two main interactions are described, the electrostatic interactions and the Van der Waals forces [44]. Electrostatic interactions are described by the Coulomb's law [eq. (1.38)] while the Van der Waals forces are typically described by a variation of the Lennart-Jones potential called the LJ 12-6 [eq. (1.39)].

$$U_{electrostatic} = \frac{q_i q_j}{4\pi\epsilon_o\epsilon_R r} \quad (1.38)$$

where q_i and q_j are the charges of the CG beads, ϵ_0 is the permittivity of vacuum and ϵ_R is the dielectric constant of the system and r is the distance between CG beads.

$$U_{LJ12-6} = 4\epsilon_o \left[\left(\frac{\sigma^{12}}{r} - \frac{\sigma^6}{r} \right) \right] \quad (1.39)$$

In the LJ 12-6 expression two terms can be seen, the first term to the power of 12, represents the Pauli repulsion at short ranges while the second term represents the attractive long-range forces. The depth of the potential well is described by ϵ_0 , the collision diameter (distance at which the Van der Waals forces go to zero) [44].

MATERIALS AND METHODS

Compound	Company	Lot number
Fmoc-Gly	Matrix Innovation	10L02-20-08-085
Fmoc-Asp	Matrix Innovation	10K15-20-08-079
Fmoc-Glu	Matrix Innovation	10K16-20-08-080
Fmoc-Phe	Matrix Innovation	10L16-20-08-093
Triisopropylsilane (TIS)	Sigma Aldrich	STBB8496V
Trifluoroacetic Acid (TFA)	Iris Biotech GMBH	40320
N,N-Diisopropylethylamine (DIPEA)	Tokyo Chemical Industry TCI	YBHACGR
Dimethylformamide (DMF)	Iris Biotech GMBH	P9N672020A
Acetonitrile for HPLC	WWR BDH Chemicals	18C291590
Sodium borohydride (NaBH ₄)	Sigma Aldrich	452173-100G
Silver nitrate (AgNO ₃)	AnalaR	10233J
Ascorbic acid	Riedel-deHaen	70390
Bis(trimethylsilyl)amine (HMDS)	Sigma Aldrich	STBK0330
Microposit S1813G2	DOW chemicals	10277862
Hydrogen peroxyde	Sigma Aldrich	STBC2332V
Nitric fumid acid	Honeywell	BCBS6814V
Sulfuric acid	Sigma aldrich	K52505132024
Microposit developer (MF-26A)	Dow Chemical Company	A079E71003
Photoresist Remover (Remover PG)	MicroChem	10060355
Amonium hydroxyde solution	Sigma Aldrich	SZBF3350V

Table 2.1: List of chemicals used in this project.

Instrument	Company	Lot number
Peptide synthesizer	Activotec Activo P-11	
Fluorescence spectrophotometer (peptide synthesizer)	Azura UVD 2.1S	
Capping agent remover	Activotec Activo P-14	
HPLC chromatogram	UltiMate 3000	
Chromatography column (reverse phase)	Biozem 26 μ m Peptide XB-C18	
Atomic Force Microscopy	NT-MDT SOLVER Scannig probe microscope	
Fluorescence spectrophotometer	Chronos DFD Fluoresnce Lifetime Spectrometer	
Circular Dichroism spectrophotometer	Jasco J-715 Spectropolarimeter	
Absorbance spectrophotometer	Holm and Halby Uv-1800	
Sonication bath	Branson 2510	
Filters (Ministart Syringe Filter)	Sartorius	00879103
Spin coater	Polos Spin105i	
Mask aligner	Suss MicroTec MA6 Mask aligner	
Metal evaporator	CryoFox Explorer 600	
Wafer dicer	Disco Automatic Dicing Saw DAD321	
Saw (for wafer slicer)	Disco Diamond Blade	Z09-SD2000-Y1-60

Table 2.2: List of instruments used in this project.

2.1 Computational methods

2.1.1 Molecular dynamics simulations

Molecular dynamics simulations on the Coarse-grained peptide were performed in order to test its ability to form organized fibers. Different attempts were made in order to have clear results of the simulations. Concentrations and the chemical properties of the solvent were the variables selected to be varied [table 2.3].

All-atom molecules were created in Avogadro, where the aspartic and glutamic acid were negatively charged, and saved as *.pdb* file. In order to create the coarse-grain molecule, a script named *Martinize.py* was obtained from [46] and adjusted to GFD3E. The coarse-grained peptide was compared prior to simulations to the all-atom peptide to find possible errors in the conversion [fig. 3.1]. This visualization was done in VMD [47]. Simulations were performed in water and in ethanol as solvent. Ethanol was chosen for its similarity to acetonitrile, since no CG model of acetonitrile was found to be defined in a coarse-grain force field, so a substitute was needed.

All simulations were performed in a $5 \times 12 \times 5$ nm box leading to a volume of 300 nm^3 and solvated a posteriori with its respective solvent (non-polarizable water was used) which had been energetically equilibrated in a simulation box of the same magnitude. NaCl ions were added to the simulation box, enough to screen the negative charges of the aspartic and glutamic acid, that is three times the concentration of GFD3E peptide. A two step simulation was performed. First a steepest descent minimization of 50.000 steps was performed and let run until an energy of $20 \text{ K J mol}^{-1} \text{ nm}^{-1}$ was achieved. Once the potential energy of the system had been minimized, a 20 ns equilibration step with a time step of 10 ps was performed. The final configuration of this step was used for the analysis of the results. All MD simulations were performed in GROMACS [48]–[55]. Martini Force Field v2.2 was used in all simulations [56].

Again, analysis of the simulations was performed in VMD and in the built-in tools of GROMACS. All files used in the simulations can be found in Files link.

	GFD3E	Environment 1	Environment 2	Environment 3
Water	Box volume [nm^3]	300	300	300
	GFD3E concentration [mol/L]	0.08	0.16	0.33
	Salt concentration [mol/L]	0.24	0.48	1
Ethanol	Box volume [nm^3]	300	300	300
	GFD3E concentration [mol/L]	0.08	0.16	0.33
	Salt concentration [mol/L]	0.24	0.48	1

Table 2.3: Concentrations of GFD3E and NaCl used in the simulations. Box size was set to $5 \times 12 \times 5$ nm for all simulations. The number of GFD3E molecules inserted in the simulation box was 15, 30 and 60 respectively for environment 1 to 3.

2.1.2 Quantum Mechanical and Quantum Chemistry calculations

All initial structures prior to any of the calculations or simulations were created using Avogadro [57], with its building tools.

In all calculations and simulations an initial geometry optimization was performed in order to always use the ground state of each of the components. This step was also performed in ORCA.

ORCA QMMM block was used to perform a hybrid simulations that combines molecular mechanics and quantum mechanics calculations. The simulation was intended to test the interaction between a silver cation (Ag^+) with electronic configuration as $[Kr]4d^{10}5s^1$ and a deprotonated carboxylic group emulating the reactive centers of the GFD3E fiber. This system was chosen so it contains the minimum groups for this interaction to be done. Quantum chemical calculations were applied to the whole system. The ORCA force field required to perform the simulation was created by the ORCA program `orca_mm`. The calculations used a hybrid DFT-Hartree Fock functional (PBE0) in the deprotonated carboxylic group and a DFT triple-zeta basis set (def2-TVZP) for all the system. This combination is the recommended when working with fourth row transition metals. In the input file, the keywords `!Slowconv` or `VerySlowconv` were used to warn the software that a difficult convergence on the SCF calculations is expected. Again, it is strongly advised for systems with open-shell transition metals. The initial structure for the simulation was built in Avogadro moving the silver atom from the position given by the energy minimization step performed in Avogadro. Since only the interaction between the carboxylic acid and the silver cation is of interest, first a geometry optimization was performed of only the acid and the structure obtained from this step was used for the simulations. Constraints were applied to the simulation input file to ensure that the configuration of the carboxylic acid won't be altered over the simulation.

Quantum Mechanical (QM) simulations were performed in vacuum, in water (CPCM model) and in 30% acetonitrile. The mixed solvent was introduced to the software by giving the dielectric constant of the solvent at room temperature obtained from [58]. Visualization of the orbitals was done by plotting the isosurface calculated by ORCA. The isosurface of the orbitals can be modified to visualize more or less orbital area. If the isosurface value is reduced, a larger area of the orbital is shown, so the software will plot areas far away from the nuclei where the probability of finding an electron

is rather low. If the isosurface value is increased it will happen otherwise. The value set for the visual analysis in the project had been of 0.4.

All these analysis were performed in Multifwn [59] software using as input file a modification of the ORCA output file (the number of electrons for the silver atom both for the cation and the and the uncharged atom had to be changed to 18 and 19 respectively, using only the valance electrons).

All files used in the MD and QM simulations and calculations can be found in Files link.

2.2 Peptide synthesis

The peptide used in this project is composed of Glycine-Phenylalanine-Aspartic acid and Glutamic acid, in the sequence GFDFDFDE [fig. 2.1]. The Fmoc group on the glycine residue was not removed after synthesis. All amino acids used as well as the resin were produced by Matrix Innovation. Synthesis was done in an Activo P-11 synthesizer from Activotec and monitored by an Azura UVD 2.1 S UV monitor. Work list for the synthesis can be found in appendix A.6.

Cupping of the peptide was done in an Activo P-12 from Activotec with a 5 mL solution of 92.5% Trifluoroacetic acid (TFA) from IRIS Biotech GMBH, 2.5% of water MiliQ quality and 2.5% of Triisopropilsilane (TIS) from IRIS Biotech GMBH. This solution was introduced in the reactor which was shacked by 1 hour. Then cleaned with 5 mL of pure TFA for 1 minute. The cupped peptide was recollected in a 50 mL Falcon tube and precipitated with ice-cold Dietileter by performing 3 cycles of 10 minutes centrifugation at 5000 rpm. The pellet was kept over night at -20 °C. The peptide was vacuum dried next day. Peptide was stored at -20 °C from that point on.

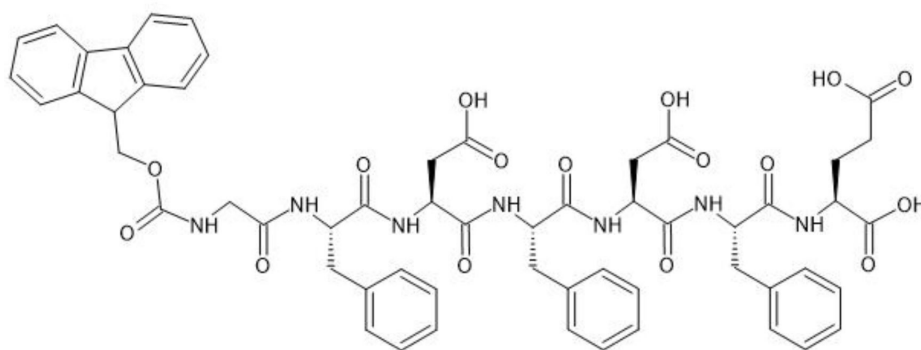


Figure 2.1: Fmoc-GFD3E peptide representation

2.3 High Pressure Liquid Chromatography (HPLC)

Analytical HPLC was performed in a Ultimate 3000 equipment from Dionex with a C18 reverse phased column (*BiozenTM* 26 μ m Peptide XB-C18). The peptide was dissolved to a concentration of 1 g/mL in a solution of 5 % HiPerSolv CHROMANORM acetonitrile from WWR BDH Chemicals and 95 % water MiliQ quality and sonicated for 3 hours at around -25 °C in order to dissolve all the fibers. The injection volume

was set to 20 μL .

2.4 Circular Dichroism

CD analysis was performed in a range of dilutions of the peptide from 0.001 mM up to 3mM (0.001 mM, 0.005 mM, 0.020 mM, 0.025 mM, 0.05 mM, 0.1 mM, 0.25 mM, 0.5 mM, 0.75 mM, 1 mM, 2 mM, 3 mM). Peptide was dissolved in 30% Acetonitrile-70% water quality MiliQ. A mother solution of 1 mM was used from which the smaller dilutions were obtained. Solutions were rested over night before performing the measurements. Measurements were performed first in a 1 mm path length cuvette and later in a 0.1 mm path length cuvette. Cuvette was rinsed after every measurement with water MiliQ and ethanol prior to the introduction of the next sample.

2.5 Atomic Force Microscopy

SiO 100 substrates were used to deposit the samples on. The substrates were clean in a two steps protocol; first acetone was added on a 15 mL Falcon Tube with each substrate and introduced in a sonication bath for 30 minutes. Substrates were then rinsed and immersed in Mili Q water, again in a sonication bath, for 30 minutes. Then the substrates were rinsed one last time with MiliQ water, ethanol and dried with N_2 gas. Sample was deposited in two different ways: 1) 15 μL of sample was deposited on the substrates and let dry over night in a dust-free environment and 2) 15 μL were deposited on the substrates and let dry for 20 minutes. Both methods were followed by a rinsing step with Mili Q water and a N_2 gas drying step prior to observation in the AFM.

2.6 Emission spectrometry

Emission analysis was performed in a Chronos DFD Fluorescence Lifetime Spectrofluorometer with temperature inside the instrument set at 20 °C controlled by a TC125 Temperature controller from Quantum North West. Excitation wave length used was of 280 nm and the emission was evaluated from 250 nm to 500 nm.

Two methods were used to study the emission spectra of the samples:

- Liquid sample from dilutions: A 10 mm light path cuvette was used. Only one dilution (0.75 mM) was used since the fibers are expected to ensemble in the same fashion in all dilutions.
- Solid substrate: three samples were prepared on quartz wafers which were cleaned following the steps mentioned in section 2.5. Concentrations used were 0.5 mM, 0.75 mM and 1 mM. In order to ensure a good coverage of the substrate, peptide dilutions were left for 1 hour to dry in a dust-free environment prior to analysis. A microscope glass plate was used to stabilize the wafers on the holder.

2.7 Ag functionalization of GFD3E fibers

Functionalization of GFD3E fibers with silver nanoparticles was performed using slightly different protocols, where both the reducing agent and the incorporation of silver into the GFD3E solution were modified. Silver nitrate was used as silver ion donor and as reducing agent two different compounds were tried. Sodium borohydride is a very common reducing agent that not only will reduce the silver ions into silver nanoparticles but when in excess will stabilize the complexes as well [60]. The steps followed for the functionalization of GFD3E fibers were inspired by [8] but concentrations and volumes were changed to fit them with the properties of GFD3E fibres. No detailed protocol was found in the literature, in terms of volumes and reaction times so different strategies were tried to assess which one led to better results.

The reducing agent used either NaBH_4 or Ascorbic acid, were always freshly prepared. A 20 mL stock solution of AgNO_3 10mM was prepared and stored in darkness at room temperature. All samples were analyzed in the UV-vis spectra after the process was done.

- **Protocol 1:** To a 5 mL of GFD3E at 0.75 mM 1.25 mL of AgNO_3 at 5 mM was slowly added. After all the AgNO_3 was added, a solution of 1mM of freshly prepared NaBH_4 equilibrated to a pH of 8 was slowly added until the colour of the solution turned to light yellow.
- **Protocol 2:** Two samples were prepared by this method, one was left uncovered for the whole procedure and the other was covered to keep it from light. From a stock solution of 2 mM of GFD3E, 0.5 mL were dissolved in 0.7 mL of a 30% Acetonitrile solution for a final concentration of 0.75mM of GFD3E. On this solution 0.5 mL of AgNO_3 10 mM were added at once and the mix was left under vigorous stirring for 30 minutes. After the 30 minutes, a solution of 0.1 mM of NaBH_4 at pH of 8.6 was added dropwise until the solution turned into a light yellow color. Then, the reaction was stopped.
- **Protocol 3:** From a stock solution of GFD3E 2mM, 0.5 mL were introduced into a flask. This solution was diluted introducing 0.5 mL of AgNO_3 0.5 mM dropwise with a Pasteur pipette. Then the solution was reduced with NaBH_4 0.1 mM until the color turned into a light yellow color. These steps were performed while keeping the solution in light.
- **Protocol 4:** From a stock solution of GFD3E 2 mM, 0.37 mL were introduced in a flask and diluted to 1 mL with a solution of 30% Acetonitrile. To this solution, 1 mL of AgNO_3 3 mM was added dropwise. The resultant solution was then reduced with Ascorbic acid 1mM until the color turned yellow.
- **Protocol 5:** From a stock solution of GFD3E 2 mM, 0.37 mL were introduced in a flask. This solution was then dissolved by adding dropwise 0.3 mL of AgNO_3 10 mM to reach a final concentration of 0.75 mM of GFD3E. This solution was then reduced by adding dropwise with a burette Ascorbic acid 1 mM until the solution turned yellow. These steps were performed while keeping the solution in light.
- **Protocol 6:** From a stock solution of GFD3E 2 mM, 0.37 mL were dissolved to 1 mL with 30% Acetonitrile. This solution was left 1 hour at room temperature. Subsequently, 0.5 mL of AgNO_3 at 5.6 mM was added drop-wise. Once all

the AgNO_3 had been added, a freshly prepared solution of NaBH_4 0.5 mM (equilibrated to a pH of 8.5) was introduced drop-wise until a change of color to a light yellow was observed.

- **Protocol 7:** From a stock solution of GFD3E 2 mM, 0.37 mL were dissolved to 1 mL with 30% Acetonitrile. This solution was left 1 hour at room temperature. Subsequently, 0.5 mL of AgNO_3 at 11.25 mM was added drop-wise. Once all the AgNO_3 had been added, a freshly prepared solution of NaBH_4 0.5 mM (equilibrated to a pH of 8.5) was introduced drop-wise until a change of color to a light yellow was observed.
- **Protocol 8:** A solution of 2 mL of 0.75 mM GFD3E was prepared and stored in the fridge over 3 days. To this solution 1 mL of freshly prepared (equilibrated to a pH of 8.5) 1 mM NaBH_4 solution was added and instantaneously a solution of 1 mM of AgNO_3 was added dropwise. After the addition of 5 mL (considered enough for a complete coverage of the fibers), the solution of 1 mM NaBH_4 was introduced drop-wise until a change of color to light yellow was observed.

RESULTS

3.1 Molecular dynamics simulations

MD simulations were performed to study whether GFD3E self-assembles into ordered structures or not. In order to speed-up the simulations, the peptide was converted from an all-atom system to a coarse grained system [fig. 3.1].

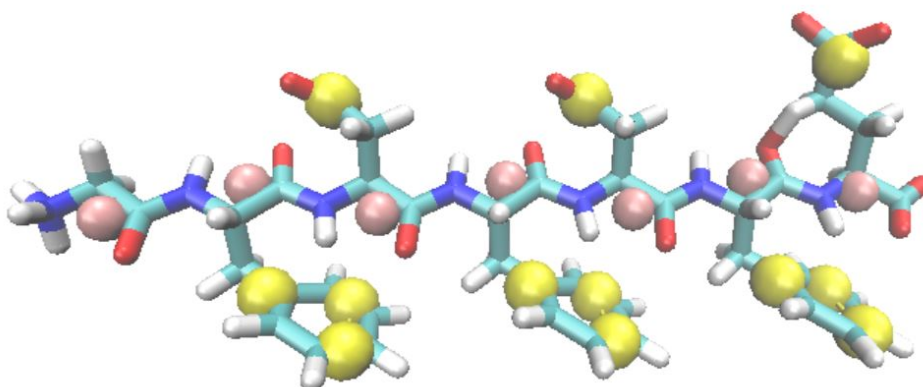


Figure 3.1: Superposition of the all-atom structure and the coarse-grained system used for the simulations.

Molecules were placed in a simulation box of $5 \times 12 \times 5$ nm, solvated and ionized so all the negative charges were screened [fig. 3.2]. The performance of the simulation was checked first by evaluating the energy minimization step and the RMSD of the equilibration step [fig. 3.3].

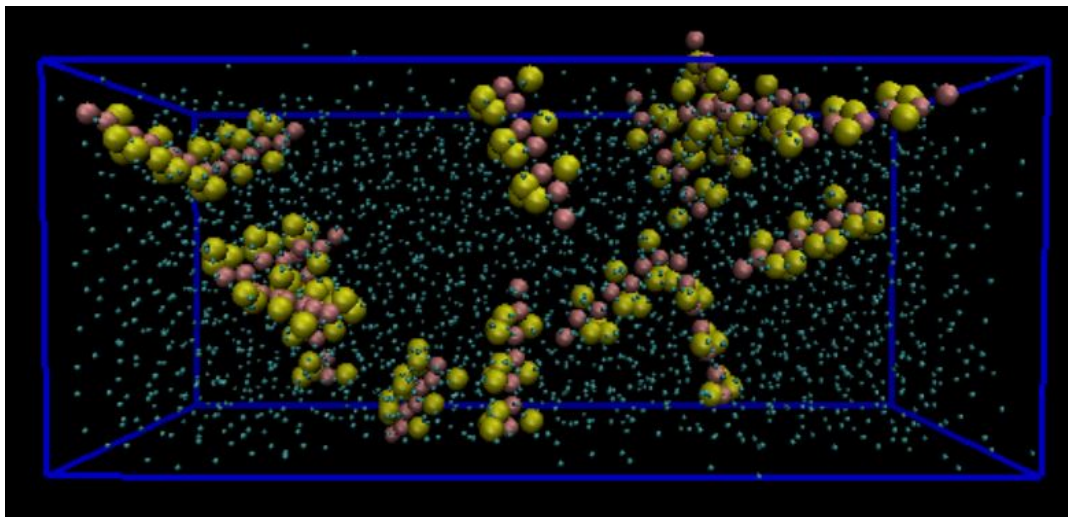


Figure 3.2: Snapshot of the final configuration of the simulation box prior to the simulations. The peptide is represented by its Van der Waals radii, backbone in red and side-chains in yellow. The blue dots are the representation of the water molecules and the Na^+ atoms. The blue frame represents the limits of the box.

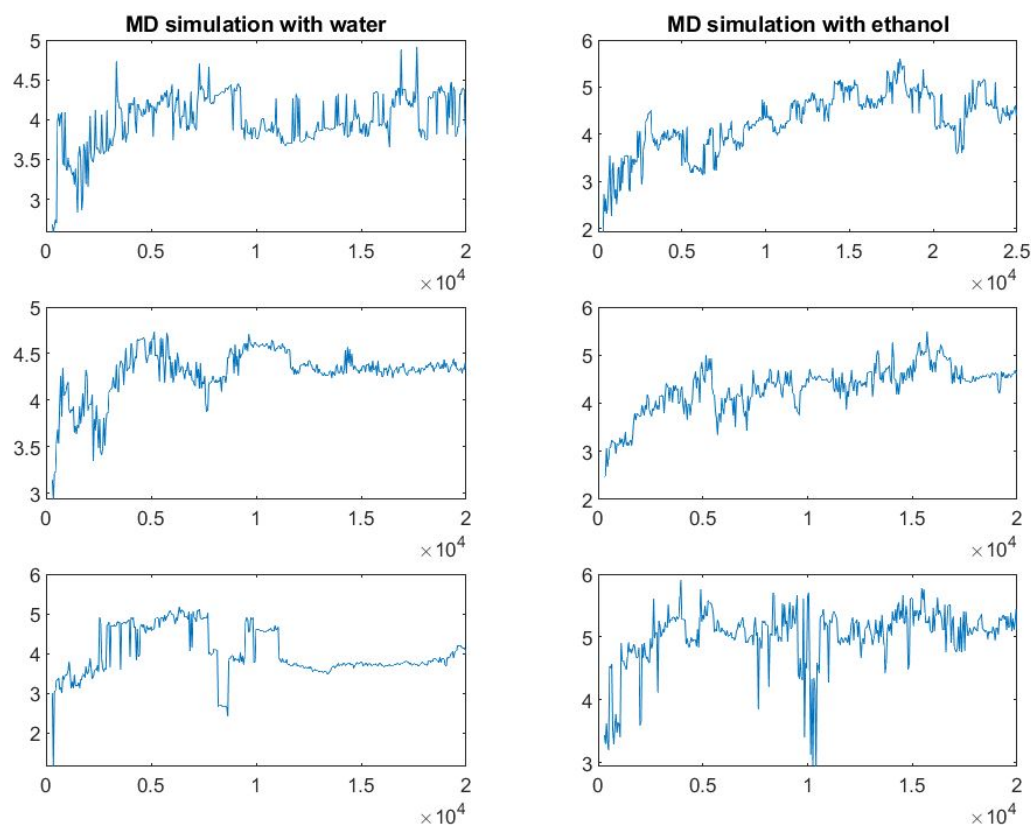
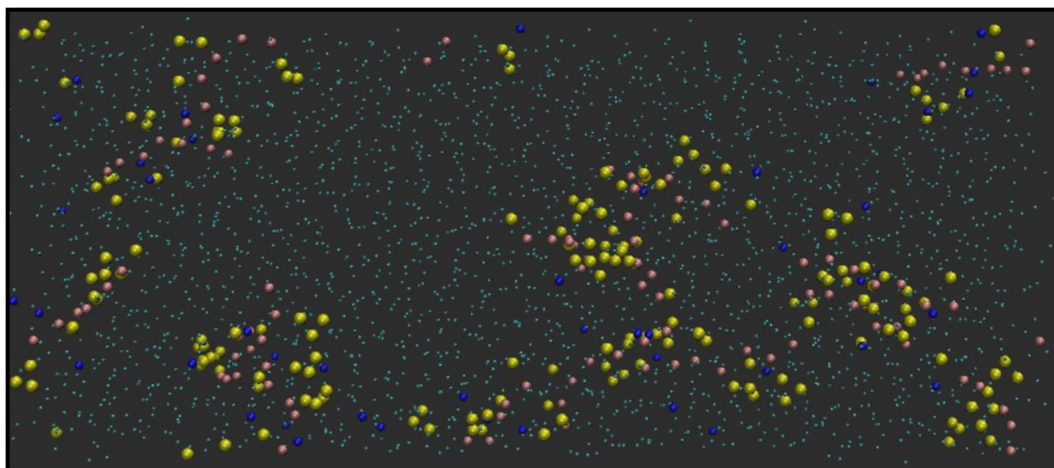
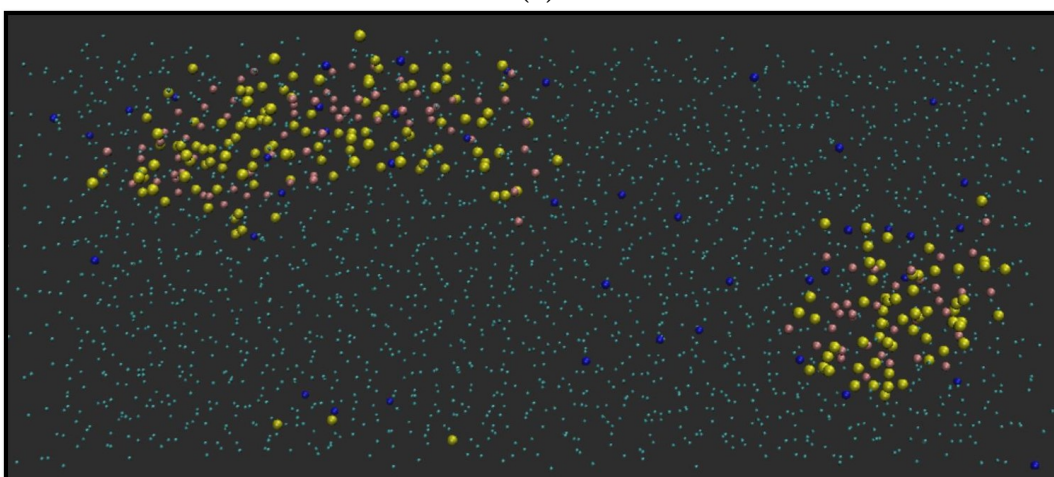


Figure 3.3: Evolution of the Root Mean Square deviation throughout the equilibration step of all three different simulation environments in each of the solvents.

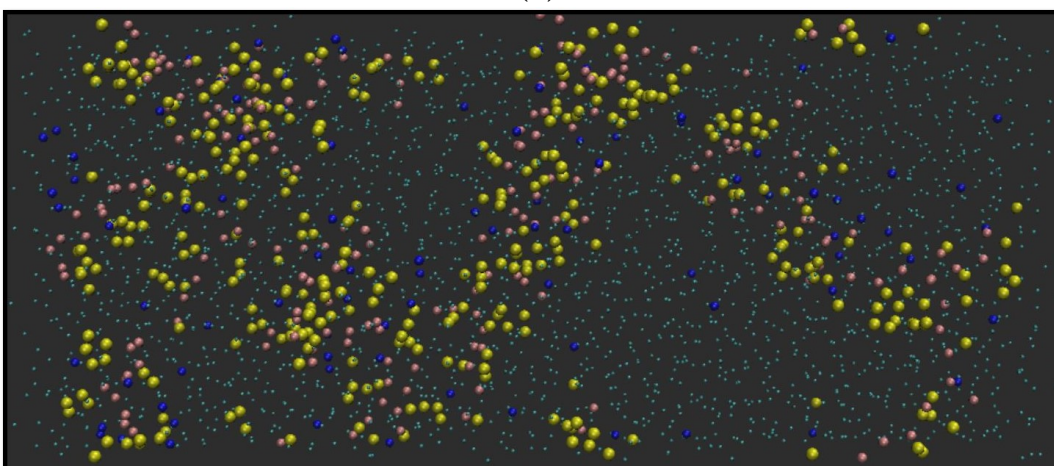
Screenshots of the final configurations of the different simulated environments were taken in VMD. Simulations performed in ethanol led to a more disperse final configuration, while when water was used as solvent, the peptide aggregated more tightly. This can be specially seen at the lowest concentration (Environment 1).



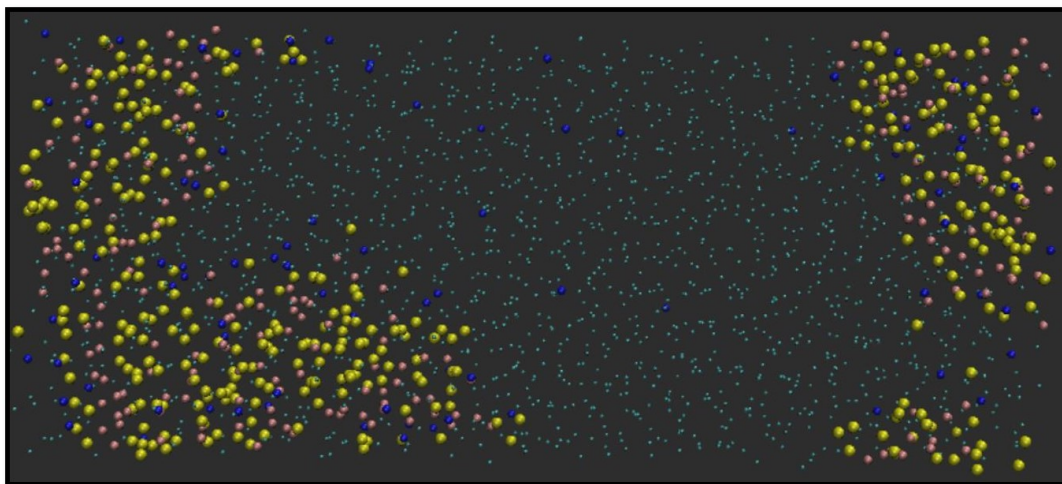
(a)



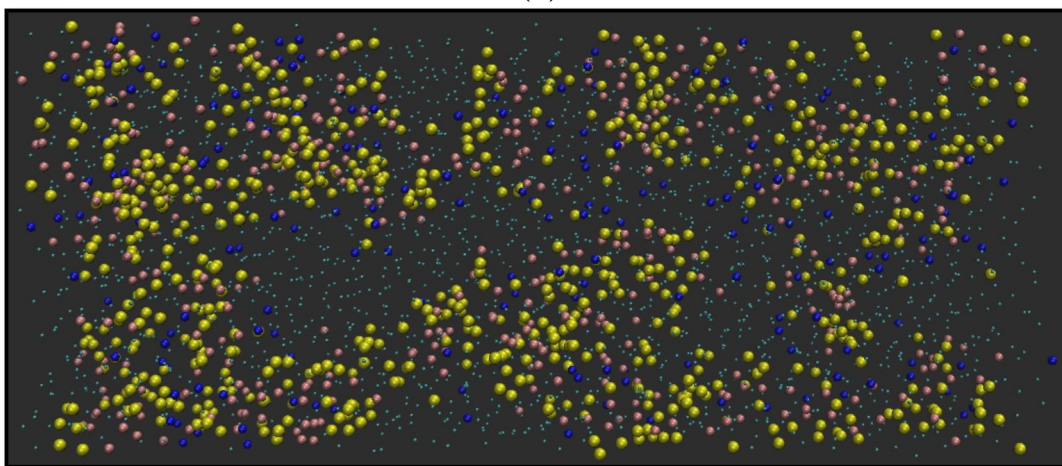
(b)



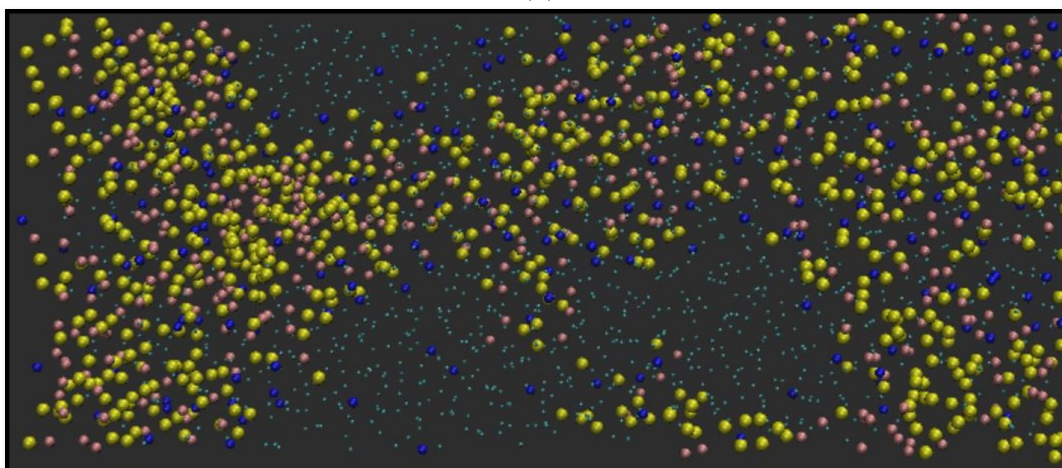
(c)



(d)



(e)



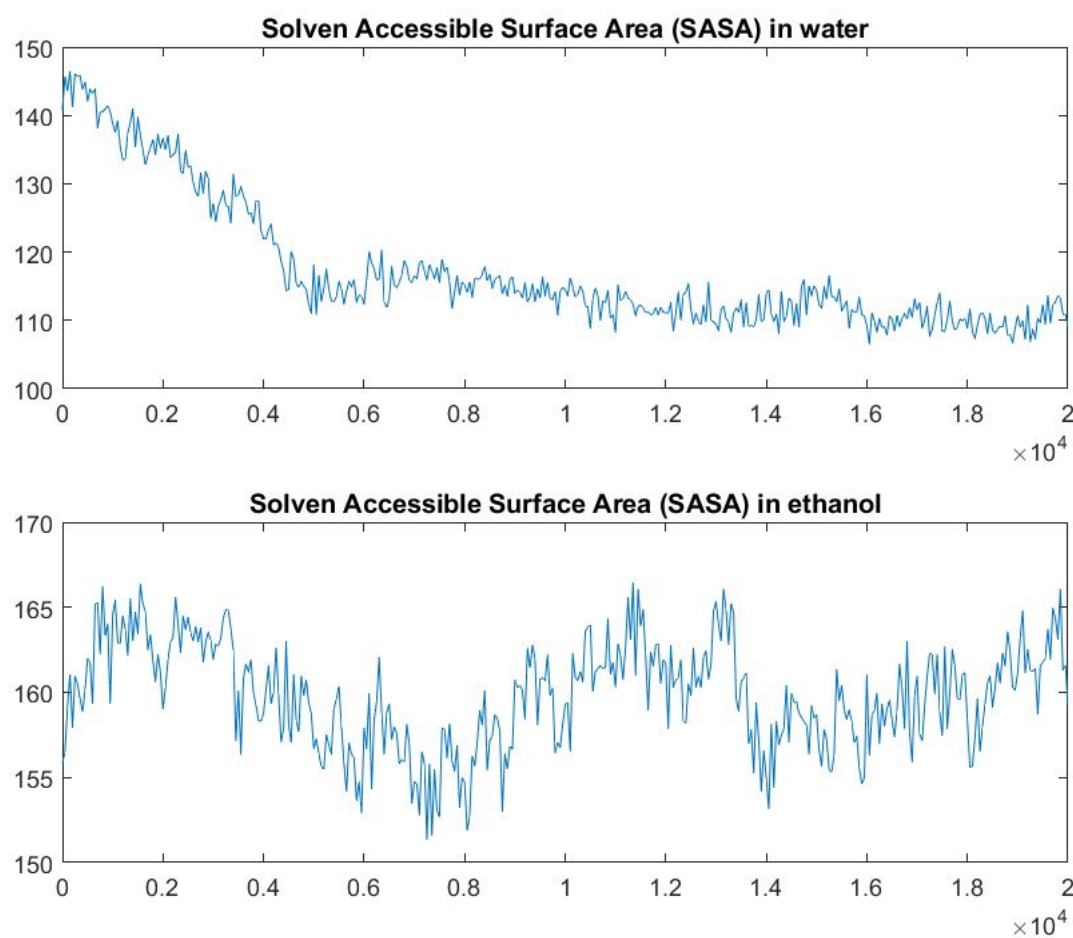
(f)

Figure 3.4: Screenshots of the final configuration obtained after the MD simulations of Environment 1 (0.08 M) in a) for ethanol as solvent and b) for water as solvent, Environment 2 (0.26 M) in c) for ethanol as solvent and d) for water as solvent and Environment 3 (0.33 M) in e) for ethanol as solvent and f) for water as solvent.

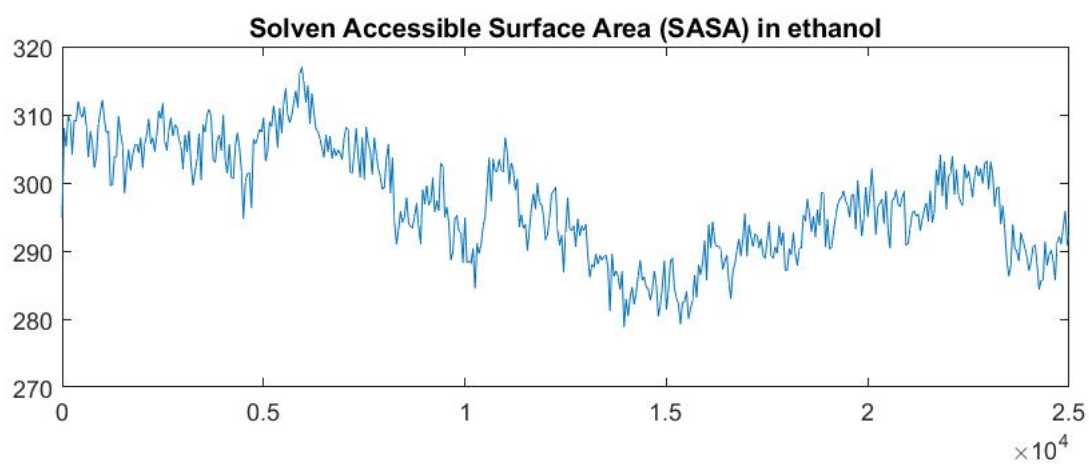
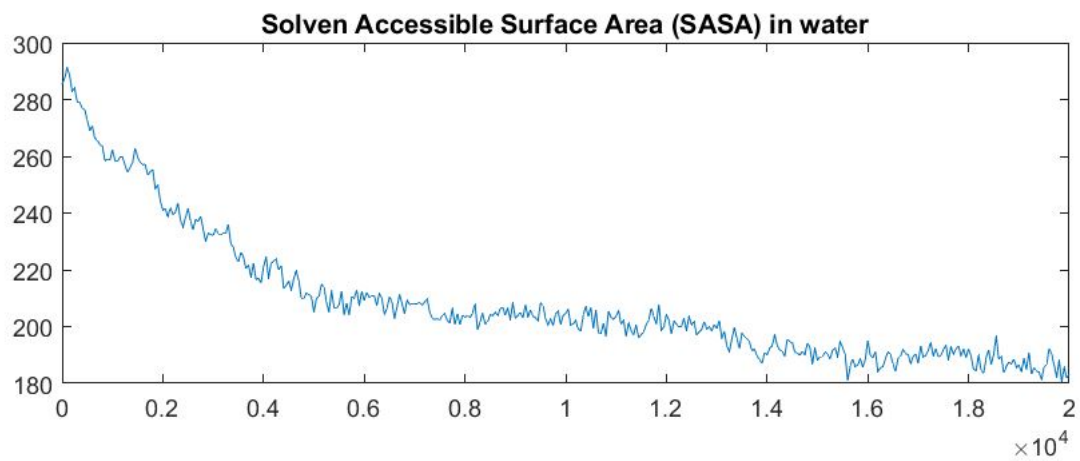
In order to evaluate the ability of GFD3E to assemble into organized structures, five different studies were performed. Each of those will bring information of whether there are aggregates, if so, who these aggregates pack and whether or not they are organized.

The first of the analysis is the study of how the solvent accessible area varies along the simulation. The Solvent Accessible Surface Area (SASA) is calculated by simulating a probe of 0.14 nm and moving this probe along the simulation box and calculating which areas are inaccessible for the probe. This was done only for those peptides belonging to one aggregate; if computed for the whole system, the distances barely vary since while some peptides are getting closer to one another, they are drifting apart from a possible third one.

For a system to aggregate, this area should be reduced, since the buried residues will decrease its contact with solvent molecules. This analysis has been performed in each simulation environment [fig. 3.5]. In order to interpret this data, the absolute value is of little interest since the evolution and the difference between the initial state and the final state will shine some light on the aggregation tendency of the peptide.



(a)



(b)

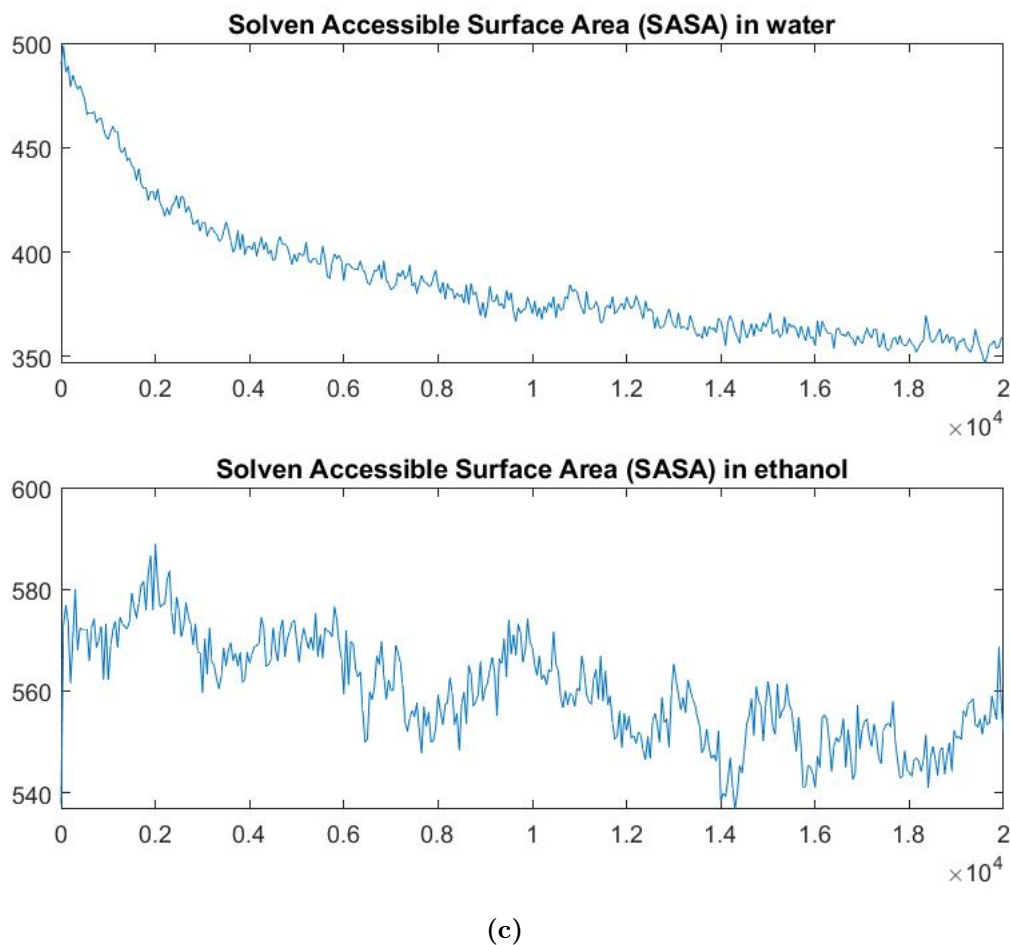
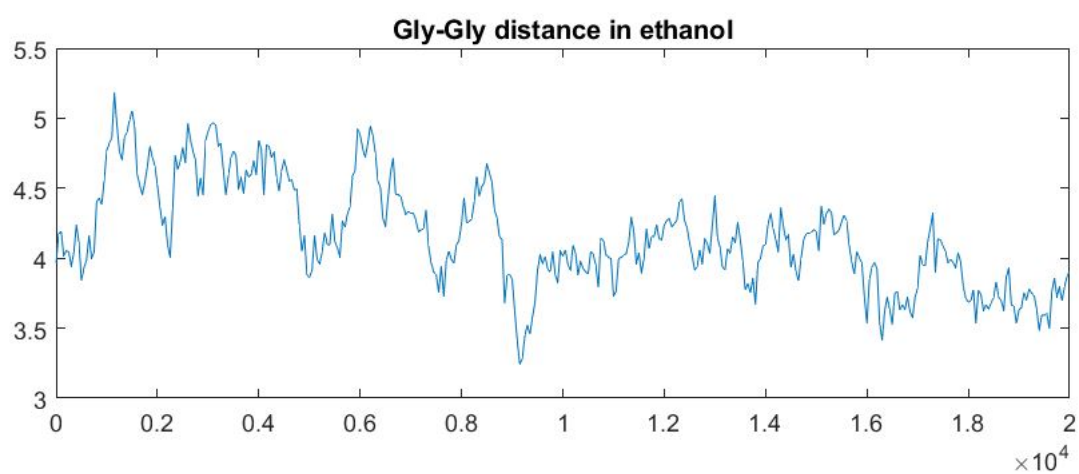
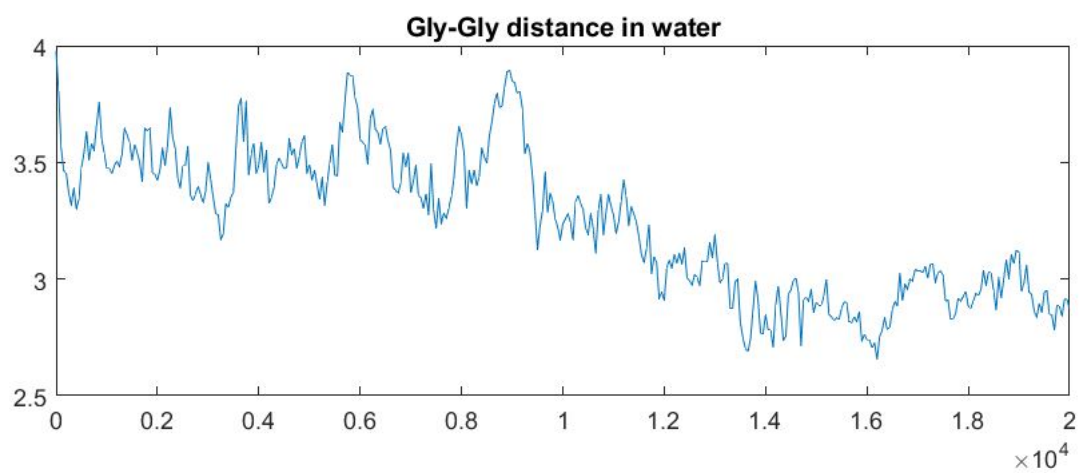
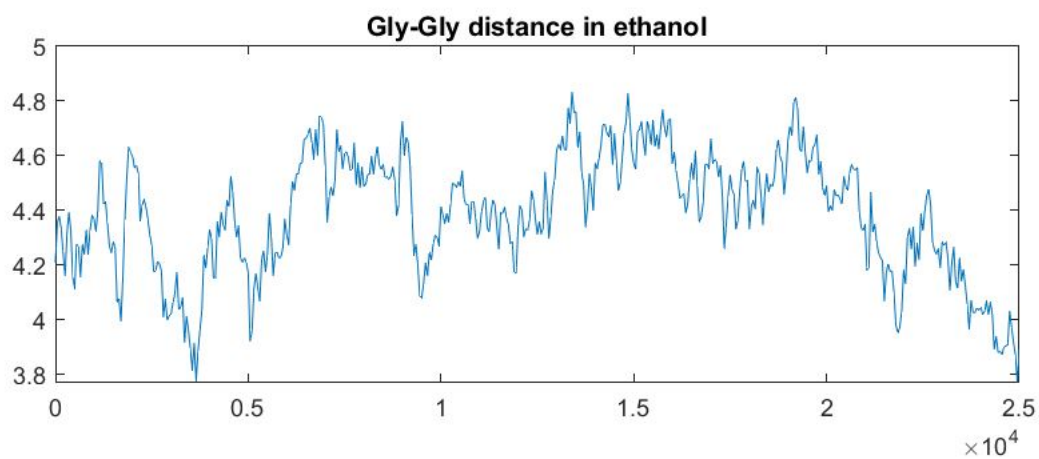
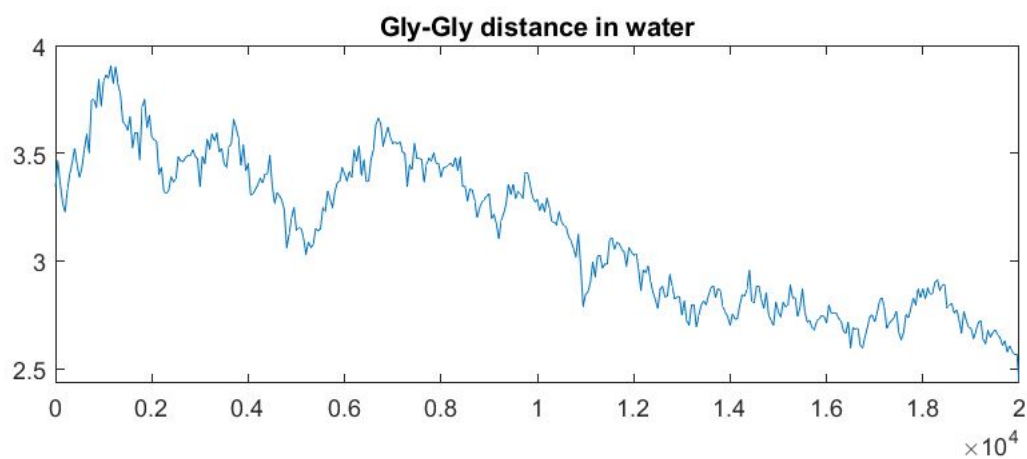


Figure 3.5: Solvent Accessible Surface Area analysis of the different simulation environments. Each GFD3E concentration is compared with either solvent. a) Represents to environment 1 with a concentration of GFD3E of 0.08 M, b) represents environment 2 with a concentration of 0.16 M and c) environment 3 with a concentration of 0.33 M. On the y axes, the solvent accessible surface area is represented in $\text{nm}^2/\text{S}^2/\text{N}$ units, while in the x axis, the simulation time is represented in picoseconds.

To assess how the peptides were moving along the simulation, the distance between the glycine residues was computed [fig. 3.6]. Glycine was selected since there is only one residue in each peptide and it has no side-chain serving as a good reference point to express the location of the peptide. In an aggregating system, peptides should get closer to one another. This study says little about whether the clustering is done in an ordered or disordered way, but it is a good indicator of aggregation nonetheless.



(a)



(b)

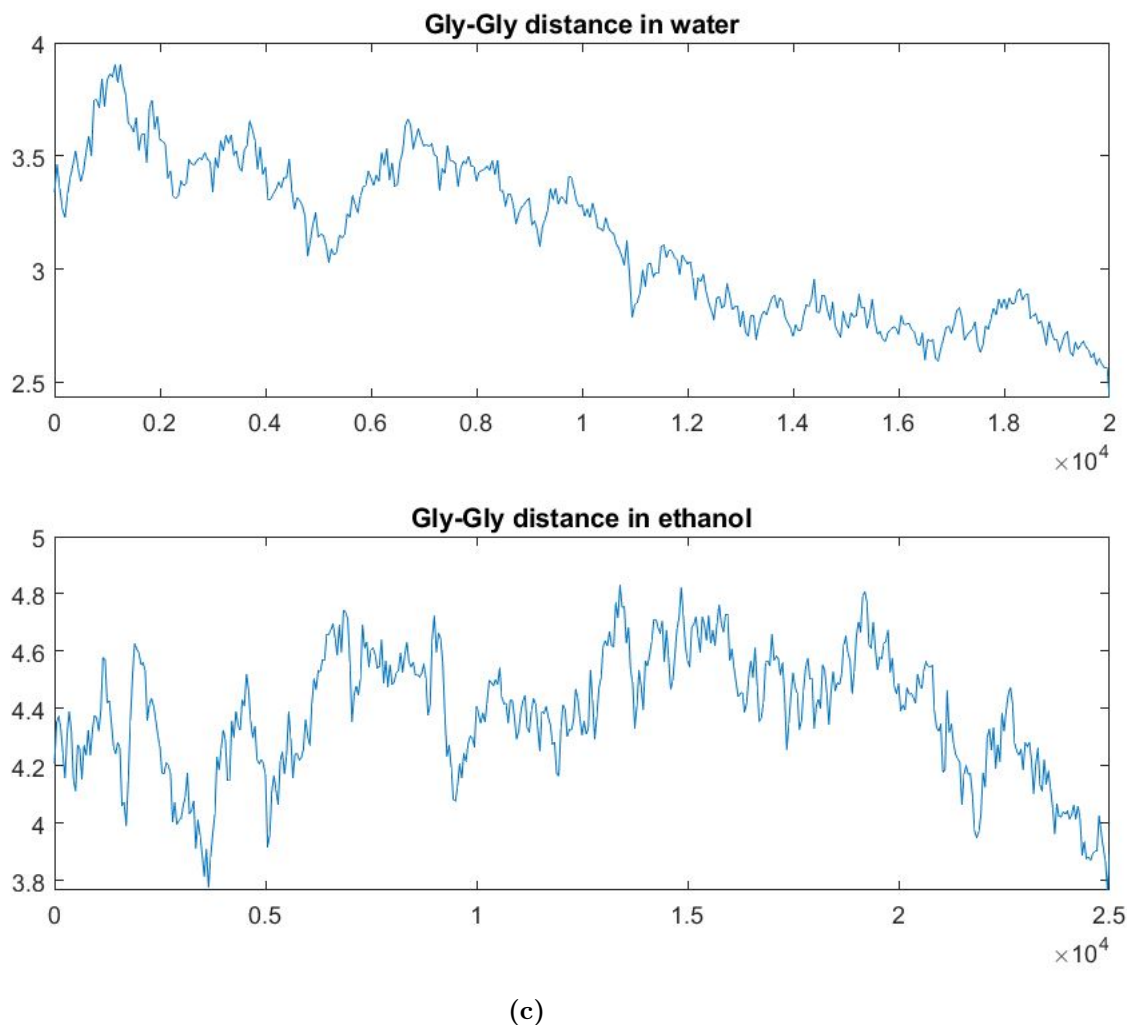
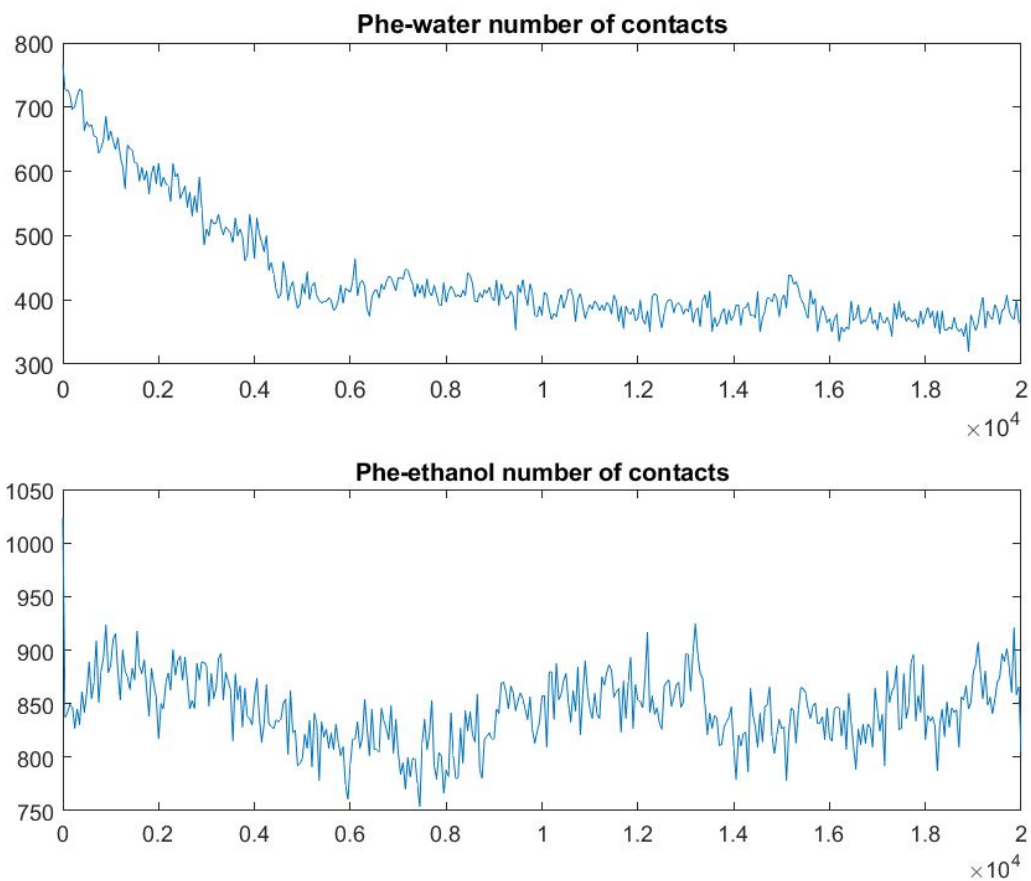


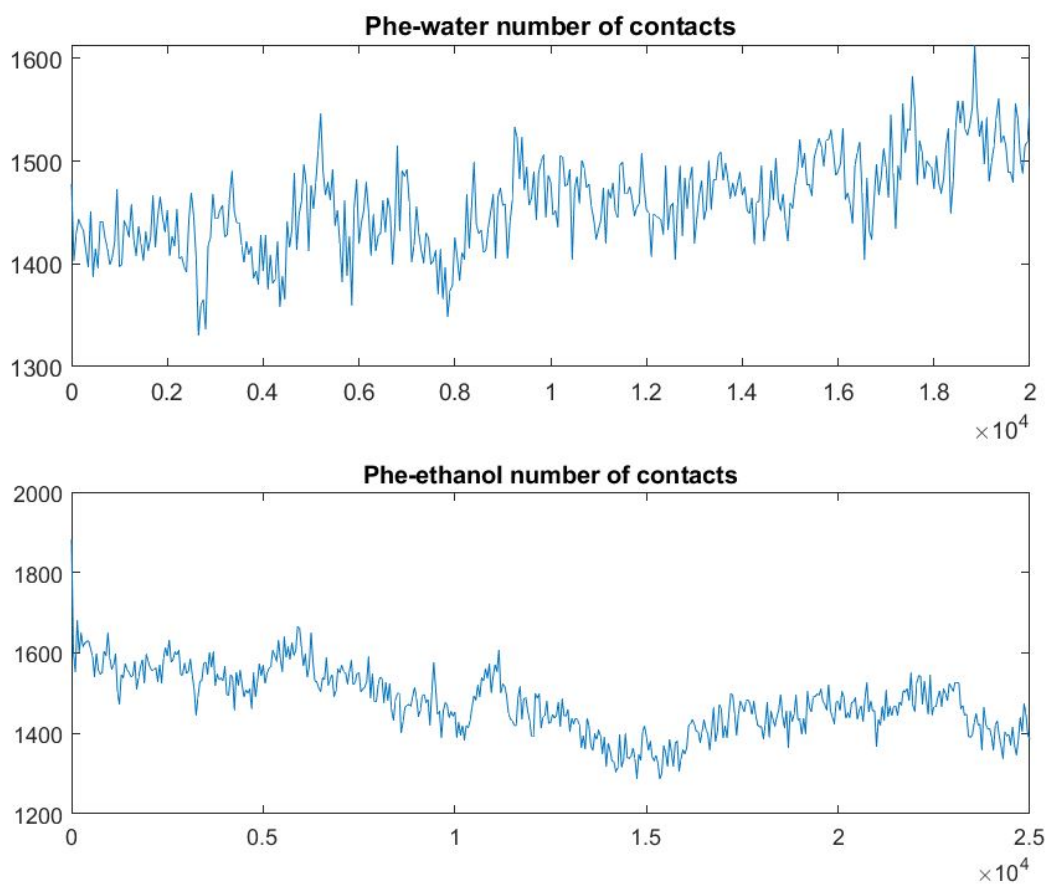
Figure 3.6: Average distance between glycine residues along the simulation. It is calculated by computing the distance between all the glycine residues in the system and calculating the average of the data. a) Represents to environment 1 with a concentration of GFD3E of 0.08 M, b) represents environment 2 with a concentration of 0.16 M and c) environment 3 with a concentration of 0.33 M. On the y axes, the distance is represented in nanometric units, while in the x axis, the simulation time is represented in picoseconds.

Distances between the glycine residues were calculated between all those peptides belonging to the same cluster. A clear attractive effect can be seen for both ethanol and water as solvent, although the strength of this attraction is found to be notably superior when the peptides are dissolved in water than when the peptides are dissolved in ethanol.

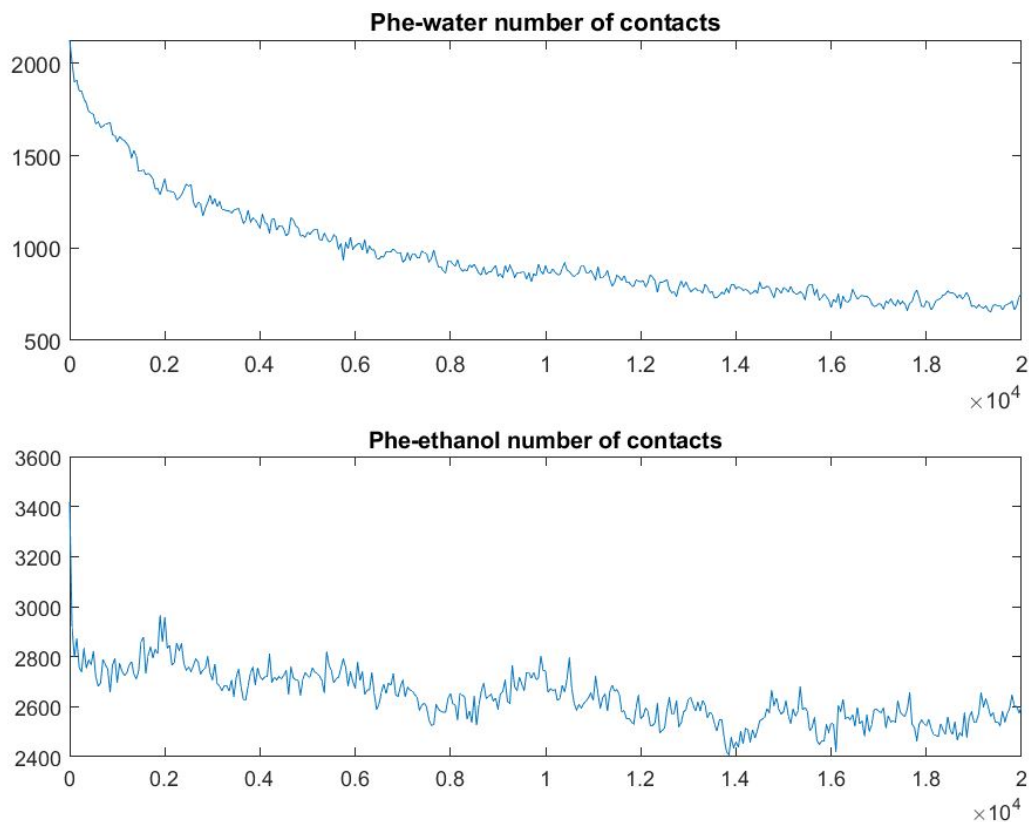
Once the presence of clusters had been confirmed by different methods, the nature of this clusters is evaluated. Aromatic residues are expected to be buried inside the cluster isolated from the solvent molecules. To study whether or not this is the scenario found in the system under study, the distance of the solvent molecules to the phenylalanine residues was compute.



(a)



(b)

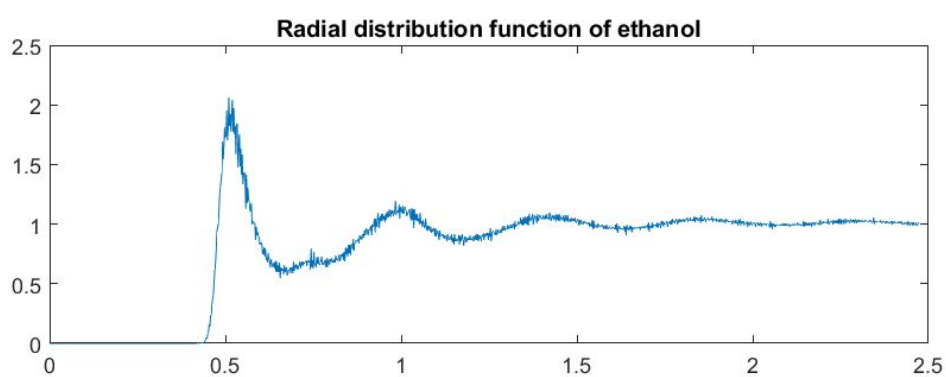
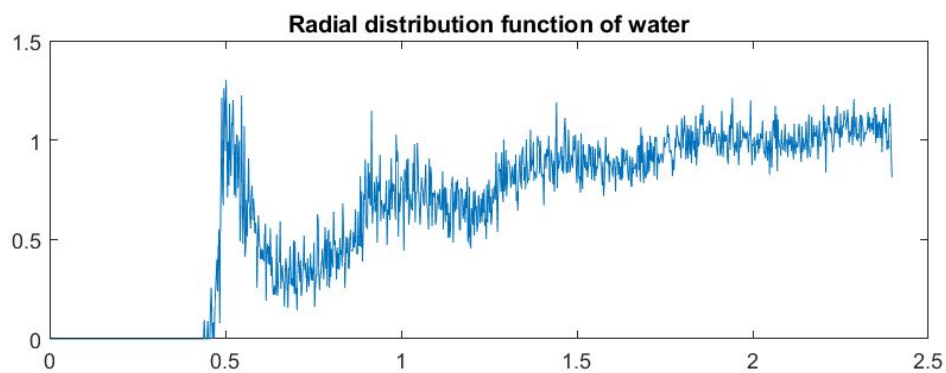


(c)

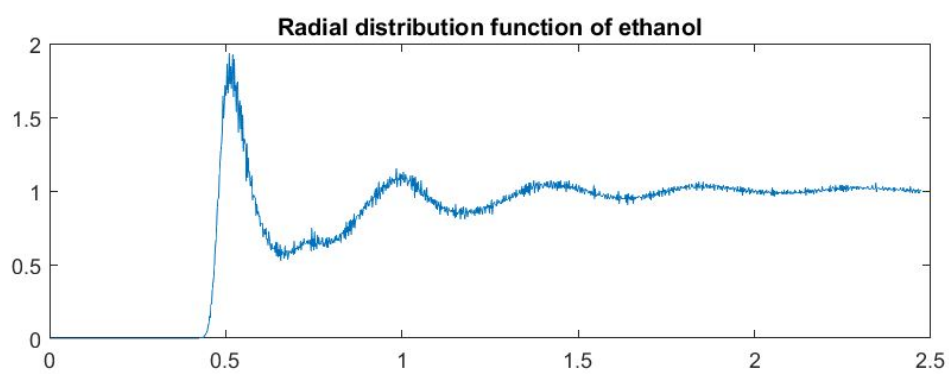
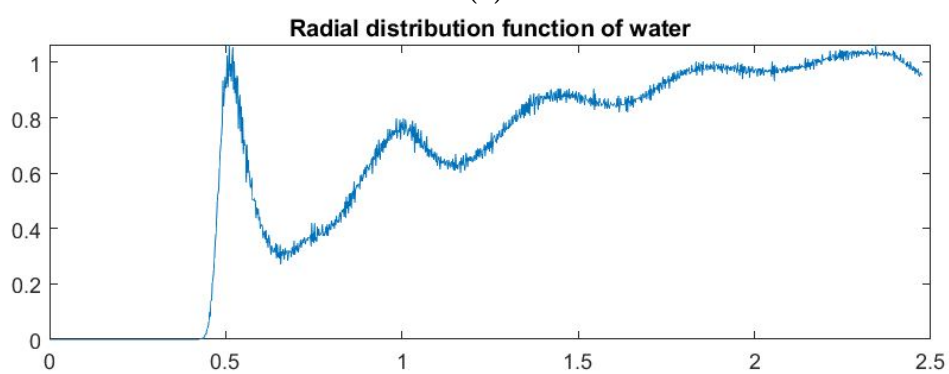
Figure 3.7: Average distance between phenylalanine residues and solvent molecules along the simulation. It is calculated by computing the average location of the group comprising all phenylalanine residues and calculating the distance to the group comprising all solvent molecules. a) Represents to environment 1 with a concentration of GFD3E of 0.08 M, b) represents environment 2 with a concentration of 0.16 M and c) environment 3 with a concentration of 0.33 M. On the y axes, the distance is represented in nanometric units, while in the x axis, the simulation time is represented in picoseconds.

Another analysis that can be done to see how the peptides interact with the solvent along the simulation is by calculation of the Radial Distribution Function (rdf) of solvent molecules having the peptide molecules as reference [fig. 3.8]. The Radial Distribution Function calculates the probability of finding a molecule of a given characteristic at a certain distance from a molecule of reference. In the case of this study, the rdf analysis will give information about the behaviour of the solvent molecules when they are close the peptide.

From fig. 3.8 a different behaviour can be observed between the two different solvents. When the solvent is ethanol, solvent molecules are found closer to the peptide at a higher probability than solvent molecules when this is water. This behaviour is observed as the probability $g(r)$ gets to one at lower distances for ethanol solvent than for water solvent. It is worth pointing out as well that very close to the peptide molecules, the probability of finding water molecules is noticeably lower and at a distance of 1 to 2 nm from the peptides a relatively abrupt increase is seen.



(a)



(b)

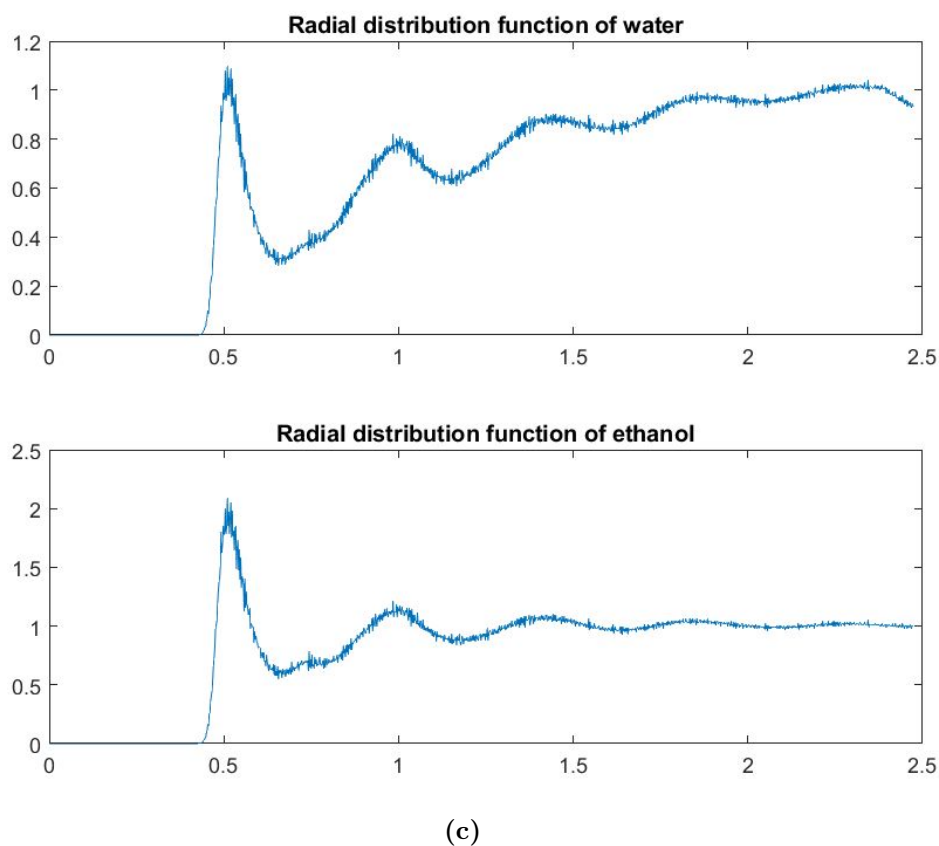


Figure 3.8: Radial Distribution Function of solvent molecules with peptide molecules as reference. a) Represents to environment 1 with a concentration of GFD3E of 0.08 M, b) represents environment 2 with a concentration of 0.16 M and c) environment 3 with a concentration of 0.33 M. On the y axes, the probability of finding a solvent molecule is described as $g(r)$ while in the x axis, the distance from the reference molecule is represented in nanometers.

3.2 COO⁻-Ag⁺ QM molecular simulation

Interaction between a silver cation and a deprotonated carboxylic acid was studied by QM molecular simulations and by a simple geometry optimization and SCF calculation on both fragments in the same system. The results obtained were verified by two steps: 1) In the output file signs of a successful calculation were sought. These are a converged SCF calculation (indicating that the ground state is found), a minimized geometry (not only the electronic but the geometric ground state is achieved) and that the final frame of the atomic/molecular orbitals is that of the expected; and 2) The final energy of the atomic/molecular orbitals was studied taking into consideration the final conformation [fig. 3.9]. Step one can be checked in Files link.

The energies of the molecular orbitals corresponding to the d orbitals of the silver cation are studied in order to understand which orbitals are affected by such interaction. Two different results are obtained. For the structure obtained by the geometry optimization (done with no solvent) and the simulation performed in vacuum, only two orbitals are still degenerate while three of them are split in energies. On the other hand, when the simulations were performed in solvent either water or 30% acetonitrile, only one orbital loses this degeneracy [fig. 3.9]. From higher to lower energy, the order of the orbitals in fig. 3.9 is:

- b) $yz > x^2y^2 > xy > xz > z^2$.
- c) $x^2y^2 > yz > xz > z^2 > xy$.
- d) $xy > xz > z^2 > yz > x^2y^2$.
- e) $x^2y^2 > xz > z^2 > yz > xy$.

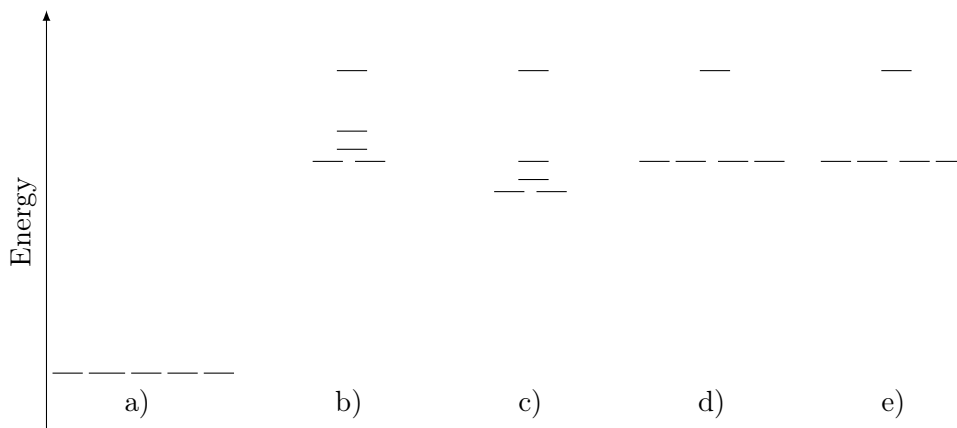


Figure 3.9: Energies of the five d orbitals from the silver cation and of the five molecular orbitals of the COO⁻-Ag⁺ complex corresponding to the five d orbitals from the silver cation. A difference of 1 eV in the results is reflected with a difference of 0.5 cm in the figure, being the lower energy -17 eV and the higher energy -7 eV. Small energy changes are not reflected in the figure. Geometry optimization step corresponds to scenario b) and QM molecular simulations are c) in vacuum, d) in water and e) in 30% acetonitrile.

Distances between the silver cation and both oxygen atoms once the geometry optimization step was done can be seen in fig. 3.10. The silver cation is attracted to an intermediate position between both oxygen atoms of 2.3 Å, agreeing with a possible electrostatic interaction.

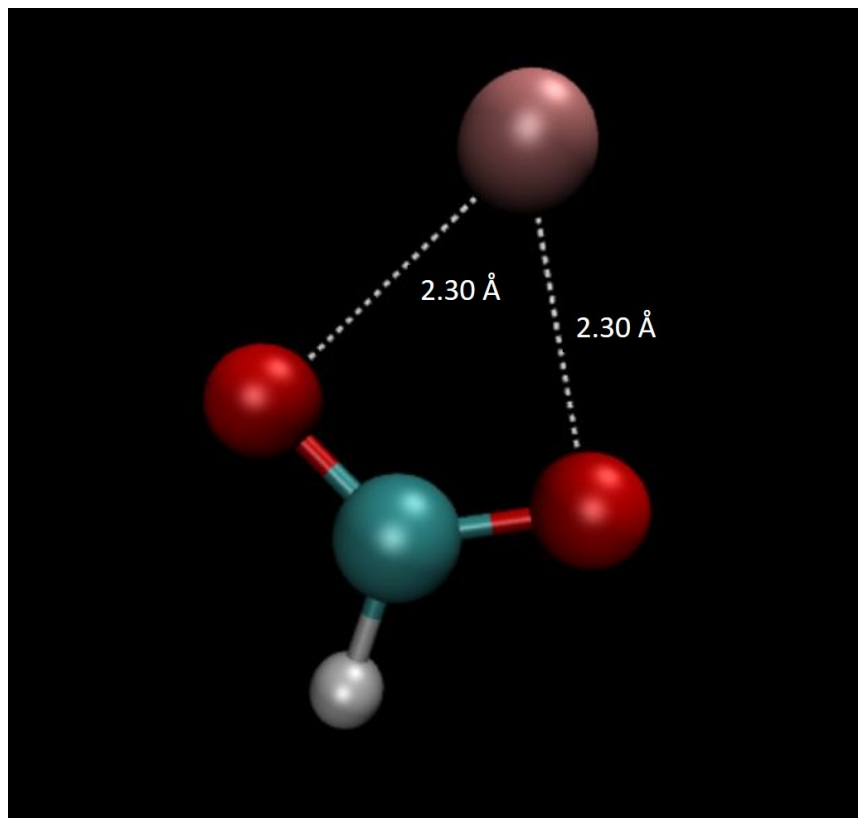


Figure 3.10: Distances of silver cation to either oxygen atoms calculated in VMD on the structure obtained after the geometry optimization in ORCA.

Further analysis can be done in order to better determine what kind of interaction occurs between the silver cation and the deprotonated carboxylic acid. Such analysis are the quantum atoms in molecules (QAIM) table 3.1, the density of states (TDOS, PDOS and OPDOS) [fig. 3.11] and the energy interaction diagram fig. 3.12. Analyzing these three calculations will give more information on how the silver cation and the deprotonated carboxylic acid interact.

A topology analysis named Quantum Atoms in Molecules (QAIM) was performed in each of the final structures obtained by either geometry optimization or by the QM simulations. This technique uses the calculated electron density to obtain some information about the bonding properties in molecular systems. It falls into the scope of topology analysis, since two topological parameters are found (CPs and BCPs). These Critical Points represent localized maxima of electron density. There are four different categories of critical points, but only two of them will be used. Those are the NCPs and the BCPs. The NCPs or Nuclear Critical Points are located at the nuclei of the atoms while the BCPs or Bond Critical Points are located equidistant of two nuclei. The idea behind the QAIM is to, through the electron density, calculate some parameters related to the electron density that will give information about how the electrons are located in the space between two nuclei [table 3.1]. The bond critical point (BCP) already gives an idea of whether the interaction between the two nuclei is attractive or repulsive. If the BCP is described by (3,-1) it will indicate that there is an attractive force between these two nuclei, whereas if the BCP is described by (3,+1) the interaction will be repulsive. The second value given in table 3.1 is the

Simulation Type	BCPs	Atoms	$\rho(r)$	$\nabla^2\rho(r)$	H(r)	$ \frac{G(r)}{V(r)} $
Geometry Optimization	(3,-3)	Ag - O ₁	0.056	0.238	-0.007	0.90
	(3,-3)	Ag - O ₂	0.056	0.238	-0.007	0.90
	(3,+3)	Ag-C	0.038	0.182	0	0.99
No solvent	(3,-3)	Ag - O ₁	0.065	0.290	-0.009	0.89
	(3,-3)	Ag - O ₂	0.058	0.24	-0.007	0.90
	(3,+3)	Ag-C	0.042	0.208	0	0.97
Water as solvent	(3,-3)	Ag - O	0.124	0.686	-0.028	0.87
Acetonitrile as solvent	(3,-3)	Ag - O	0.127	0.743	-0.029	0.87

Table 3.1: Values of the QAIM calculated for each of the simulations and geometry optimization performed to study the interaction between deprotonated carboxylic acid and silver cation. Only those BCPs and its respective values of interest are present. The topology analysis was performed in Multiwfn software and the input file as generated by ORCA with def2-tzvp as basis set and PBE0 as functional. The full analysis can be found in Files link

laplacian of the electron density ($\nabla^2\rho(r)$). A negative value of $\nabla^2\rho(r)$ indicates that there is a delocalization of the electron density along a virtual path connecting both nuclei what indicates the presence of a covalent bond. A positive value, on the other hand, will indicate the absence of electrons along the path, what is common in electrostatic interactions. The next value is the total electron energy density (H(r)). This value is strongly related to the nature of the interaction. It is calculated at the middle point between the two nuclei and it represents the accumulation of charge/electrons. If H(r) is negative, it indicates that there is an accumulation of charge in that middle point, ergo, a covalent bond. If H(r) is positive means that there is a depletion of electrons in that area and so the interaction between both nuclei will be disruptive. And for last, the ratio between the potential energy (V(r)) and the kinetic energy (G(r)). If $|V(r)| > G(r)$ the interaction is of covalent nature and if it is greater than 1 it will indicate an interaction purely non-covalent [14], [61].

The next analysis is the total, partial and overlapped density of states [62]. Analyzing such a graph will help in understanding how the molecular orbitals are created, and how the interaction between the two components is done. Usually the density of states is represented by discrete lines in the energy corresponding to each of the states, but in molecules, when there are more than one atoms interacting, the visualization and the interpretation is easier when these discrete lines are broadened by, in this case, a Gaussian function (this step was done by the software itself). The energy level of the HOMO (highest occupied molecular orbital) is represented in a dashed line. PDOS (Partial Density of States) is the analysis that breaks down the total density of states into the participation of user defined orbital types. In this case the analysis was performed only to see whether there was any overlap of the orbitals from the silver cation and the deprotonated acid that contributed to stabilizing the system. To know whether an overlap will contribute to stabilizing or destabilizing the complex, the OPDOS (Overlap of Partial Density of States) is plotted (green line in fig. 3.11). The values of the OPDOS will only be positive where there is a constructive interaction otherwise they will be negative as can be seen for the LUMO+1 orbital.

Large positive values (a strong overlap of atomic orbitals) are associated to bonding interactions while large negative values to anti-bonding. Whereas values close to zero represent a non-bonding interaction since there is no overlap of the atomic orbitals

The last analysis is to plot the interaction energy diagram from charge decomposition analysis. This analysis gives insight on how the charges of two fragments are moved to one another in order to stabilize a complex formed by these two fragments. In this case it will be used to create an interaction diagram where atomic orbitals from each of the fragments will be connected to the molecular orbitals which is made by their interaction. If there is any overlap of atomic orbitals, these will be connected to the same molecular orbital. Here atomic orbitals from both molecules interacting (in this case silver atom and deprotonated carboxylic acid) are represented in each side (write and left respectively), and the new molecular orbitals are represented in the middle. In order to get such a graph, independent SCF calculation were done for the silver cation and for the deprotonated carboxylic acid. In fig. 3.12, those orbitals that are filled or partially filled (none in the scenario that concern this project) with electrons are presented with a solid line and those empty with a dashed line. When a atomic or molecular orbital has a broken degeneracy (different energies) the lines representing those orbitals are very close to one another (as is the case for the *d* orbitals 14, 15, 16, 17 and 18 in fig. 3.12). When there is only one line but there are more than one orbitals indexes, it means that the orbitals have exactly the same energy (as is the case of the five *d* orbitals of the silver cation 5, 6, 7, 8 and 9).

Red lines connect atomic orbitals with molecular orbitals only if the molecular orbitals are composed by at least a 20% of the corresponding atomic orbital. For a molecular orbital to be formed by two atomic orbitals from different fragments there must be an overlap. The interaction between the silver cation and the carboxylic acid led to basically no overlap based on fig. 3.12 since none of the molecular orbitals is connected to a atomic orbital of both fragments.

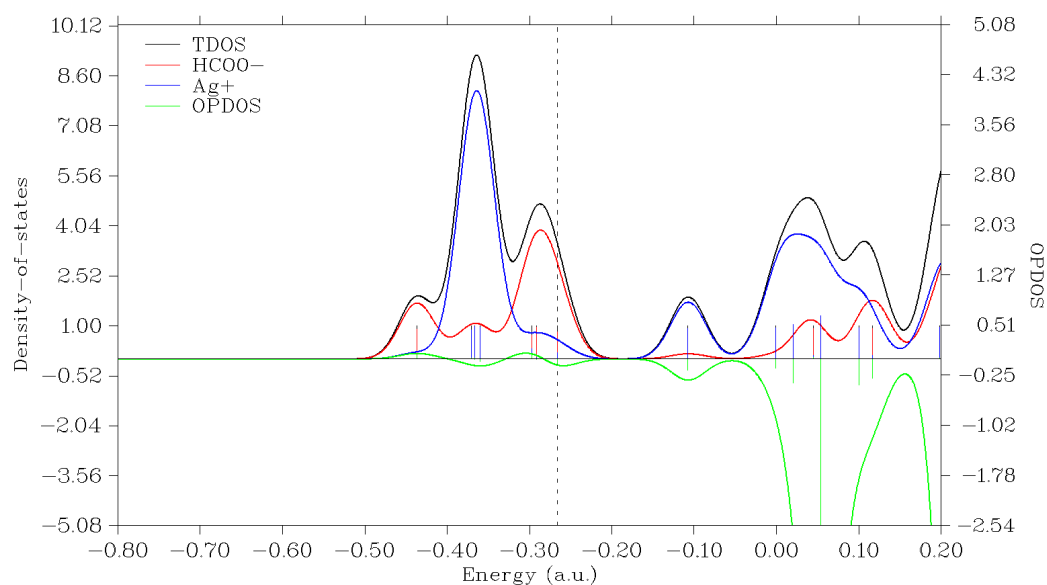


Figure 3.11: TDOS, PDOS and OPDOS. Black curve represents the total density of states (TDOS), blue and red lines describe the participation of atomic orbitals to each molecular orbital (black curve) and in green the overlap of the atomic orbitals. For a bonding interaction, this overlap must be of large positive values whereas for a non-bonding interaction it must have large negative values. Values close to zero indicate no overlapping. Each discrete line corresponds to a molecular orbital which for easy interpretation has been broadened to the black curve. Right axes represent the values for the curves (when interpreting the colored curves, the absolute value is not important but the relative value of them). Left axes correspond to the discrete lines.

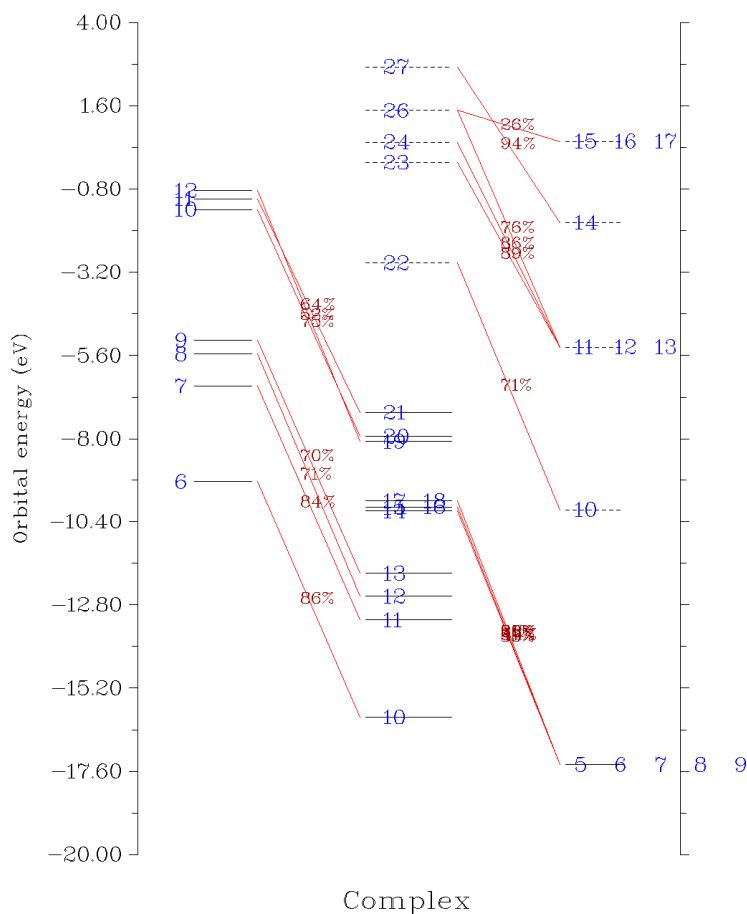


Figure 3.12: Interaction energy diagram of COO^- and Ag^+ . Solid lines represent occupied orbitals while dashed lines represent the unoccupied ones. Each orbitals is labeled by a number in blue. Molecular orbitals are present in the middle while atomic orbitals of both fragments (fragment 1 is the deprotonated carboxylic acid and fragment 2 is the silver cation) are represented in each of the sides. Red lines connect each molecular orbital to the respective atomic orbitals out of which it is formed.

The QM molecular simulations were run in ORCA treating the whole system as a QM region (atoms where quantum chemistry calculation will be applied rather than classical physics). The results are slightly different of those obtained by a simple geometry optimization. The QM molecular simulations were performed in vacuum, with water as solvent and with acetonitrile as solvent. In ORCA, the introduction of solvent is done by introducing a dielectric constant. Whereas the one for water is intrinsic to the software (80.4), the dielectric constant for acetonitrile was obtained from [58] (55.68). Furthermore, these simulations were performed under some constraints. First an energy minimization of the deprotonated carboxylic acid was performed, coordinates of which were used as an input for the simulations and a bond length constraint was applied upon them. This was done to prevent the acid from altering its structure since it would not be realistic. The three simulations led the same tendency in the

results [fig. 3.13], all of them show an attractive force between the silver cation and the deprotonated carboxylic acid. It is worth to mention that how this interaction is done and which atoms participate in it differ from the simulations with solvent and without solvent. Despite all of the starting configurations are the same, when the simulation was performed in vacuum, the silver cation was moved towards a middle point between both oxygen atoms, partially interacting with both atoms while being repulsed by the carbon atom. Notwithstanding, when the simulation was performed in either water or acetonitrile as solvent, the silver cation was attracted to only one of the oxygen atoms, placing itself around 0.4 Å closer than its homologous without solvent (1.9 Å and 2.3 Å respectively).

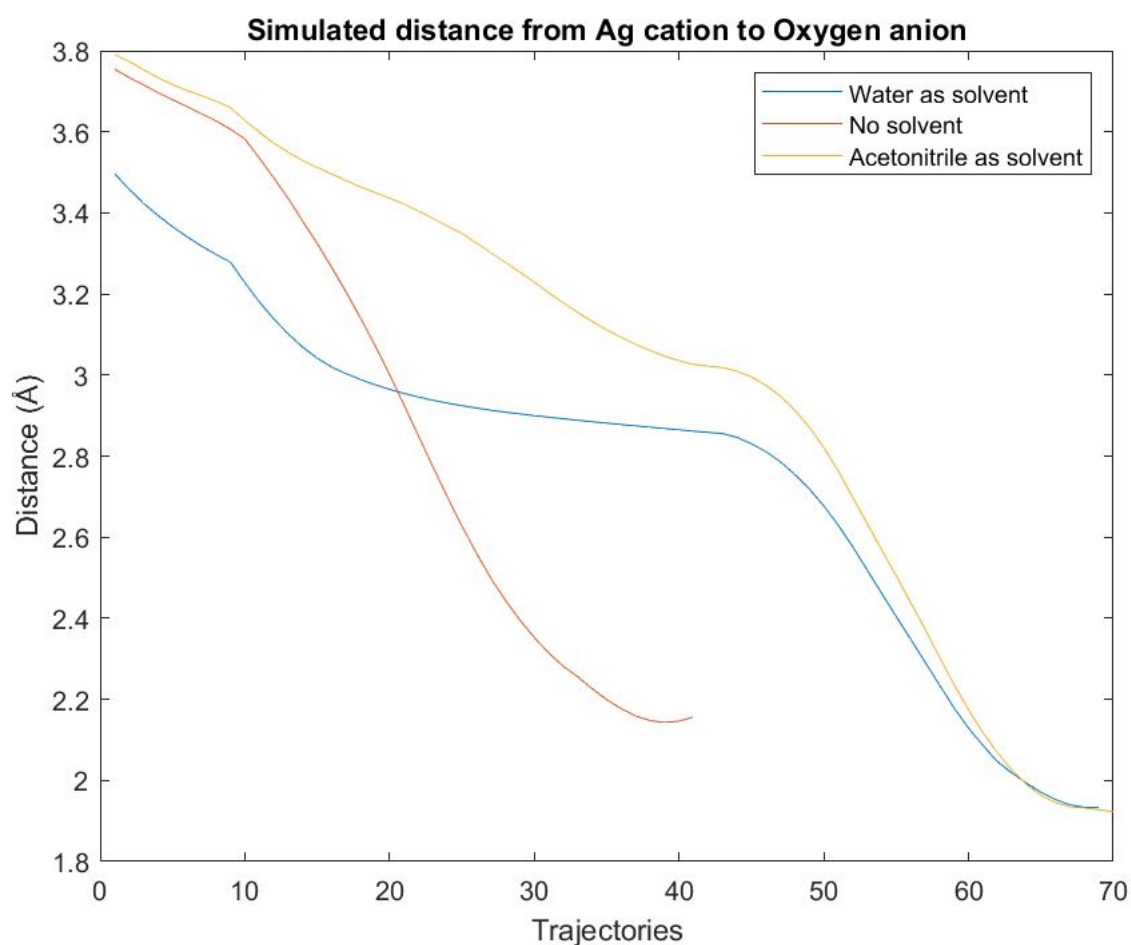
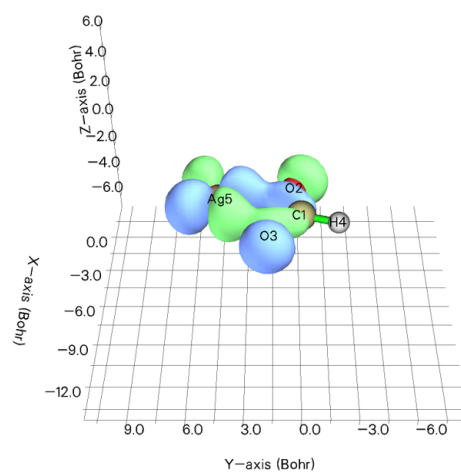
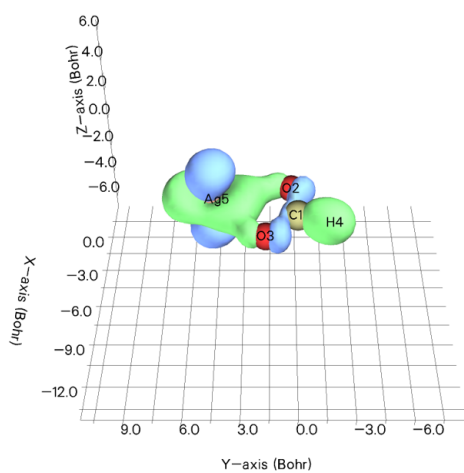


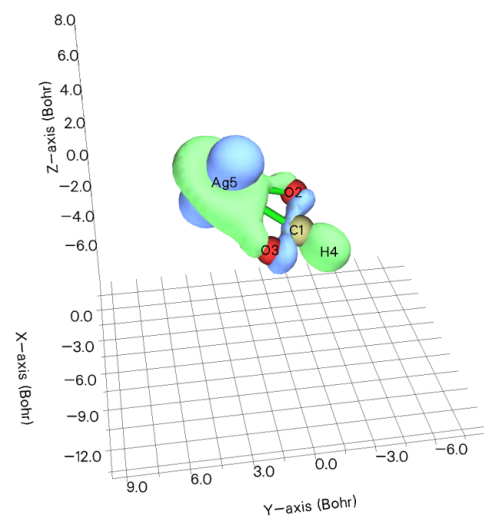
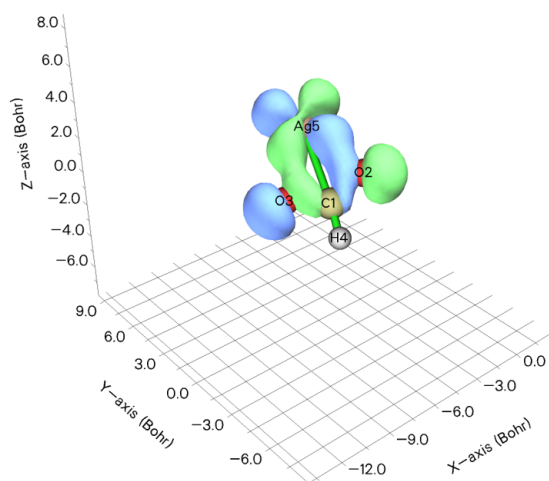
Figure 3.13: Distances obtained from the QMMM simulations. The number of trajectories varies since they depend on when the energy minimum is achieved, that means, the stable structure was found faster when simulated in vacuum than in any other solvent. All simulations were performed in ORCA and its respective input and output files can be found in Files link.

Only the results of the QAIM analysis are shown here [table 3.1], the TDOS, PDOS, OPDOS and the interaction diagram are presented in the appendix A.5, since they are all very similar to that of fig. 3.11 and fig. 3.12. For neither of the simulations a strong overlap of the orbitals exists when the PDOS and the OPDOS is observed. This is confirmed when the interaction diagram is studied. There is no molecular orbital close to the HOMO or LUMO gap that is composed by atomic orbitals from

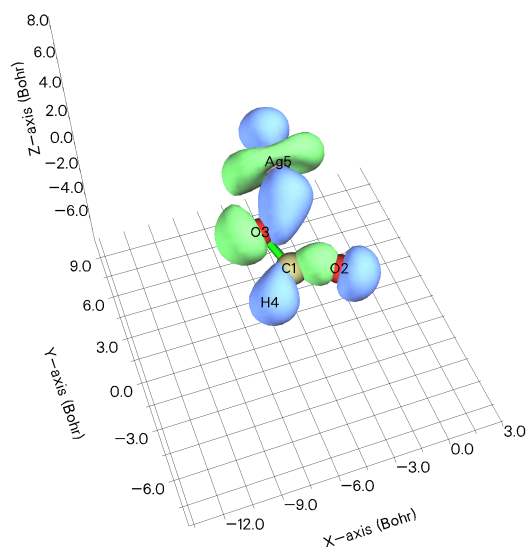
each fragment interacting. An interesting trait that can indeed be observed is the splitting of energies of the d orbitals of the silver cation on the interacting system compared to the calculations performed on the silver cation alone.



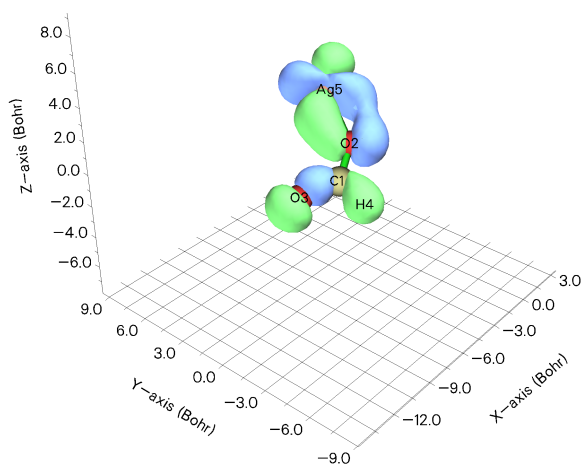
(a)



(b)



(c)



(d)

Figure 3.14: Representation of the molecular orbitals calculated by its simulation and by the geometry optimization. Only those that are formed upon interaction of different atomic orbitals are presented. These interactions will be the reason for the lost of degeneracy of the silver d orbitals in the molecular complex. a) corresponds to the geometry optimization step (orbitals z^2 and xy), b) corresponds to the simulation done in vacuum (orbitals y^2-x^2 and xy) c) to the simulation with water as solvent (orbital y^2-x^2) and d) to the simulations with 30% acetonitrile as solvent (orbital y^2-x^2).

3.3 High Pressure Liquid Chromatography

Analytical HPLC was performed on the synthesized peptide in order to assess the purity of the peptide. In the spectra obtained two major absorption peaks in retention time from 37 to 45 minutes can be seen. Two minor absorption peaks can be observed as well appearing in lower retention times. The first of those belongs to the injection peak belonging to the injection of the sample into the column. The second small peak appearing at a retention time of 28 minutes is rather small compared to the peaks at 38 and 42 minutes. The presence of these two main peaks with a small time shift between them may indicate the presence of two different peptides with one amino acid difference in the synthesis. Based on the high of the two main peaks, both compounds have a presence of roughly 50% in the peptide sample obtained after synthesis [fig. 3.15].

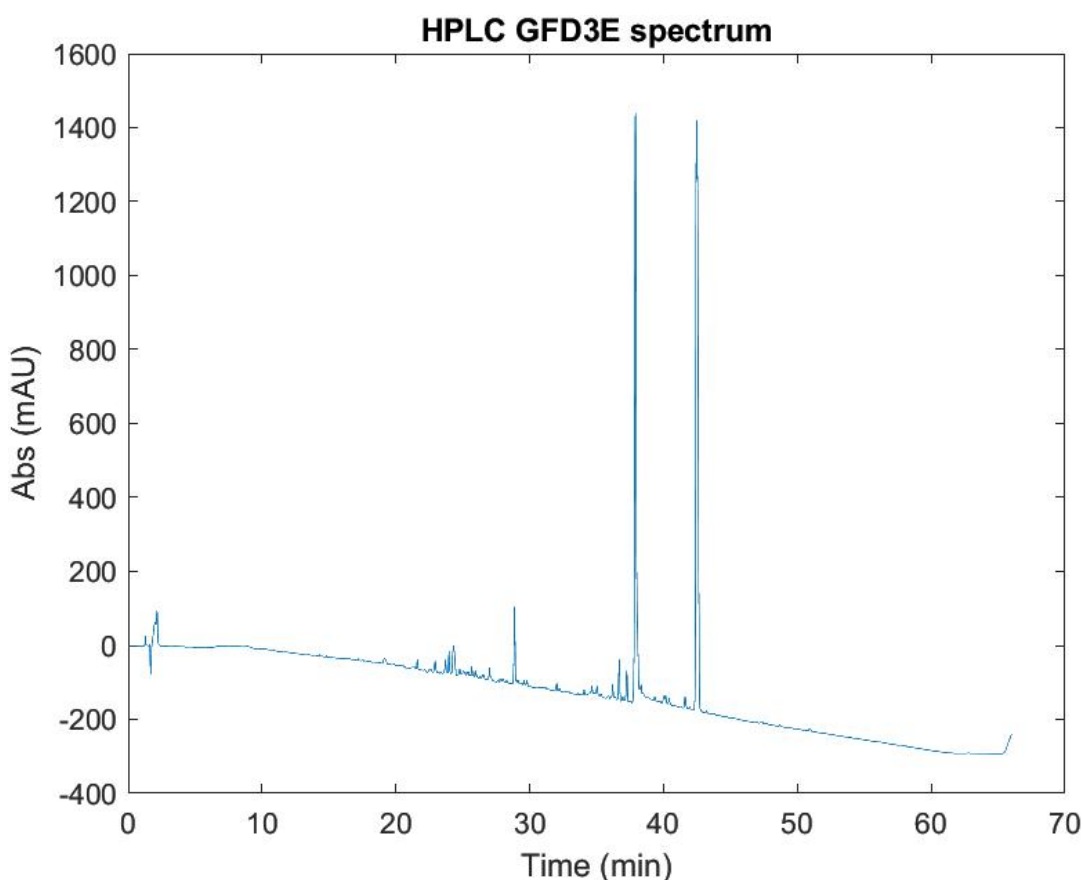


Figure 3.15: HPLC spectra of GFD3E peptide. Gradient of the mobile phase from 5% acetonitrile to 80% Acetonitrile in water quality MiliQ. Two major absorption peaks can be seen between a retention time of 38 and 42 minutes. The width of the peaks is rather narrow (less than 1 minute) indicating a pure component.

3.4 Circular Dichroism

The first analysis performed was a Circular Dichroism spectra. CD spectra calculates the difference between the absorption of right and left circular-polarized light of chiral molecules [63]. Other studies have used CD spectrometry to analyze the structure of the amyloid fibers [34], [37], [64] as a tool where while little sample volume is required,

the results are very informative. In a CD spectra, not only secondary structure can be seen but also functional groups. Aromatic rings have been reported to be identified via CD measurements. The aromatic ring from the phenylalanine amino acid is often reported to appear as a positive peak at around 220 nm wavelength when phenylalanine residues are dissolved in water [63], [65]. In the results obtained no positive peak was observed at around that specific wavelength since a characteristic negative peak for β -sheet structure must appear at such wavelength [8], [64], [66].

CD measurements were taken at different dilutions of the sample to first see the conformation of the fibers formed and second to detect at which concentration fibers begin to form and which concentration have the highest signal, meaning the larger number of fibers in solution. Measurements were taken on dilutions from 1 μ M to 3 mM. A baseline with 30% acetonitrile in MiliQ water was used to account for the effect of the solvent on the measurements. The software itself will subtract the signal of the solvent from the signal of the sample. Dilutions below 0.1 mM did not show any signal (data not shown). Only dilutions from 0.1 mM to 3mM (0.1 mM, 0.25 mM, 0.75 mM, 1 mM, 2 mM and 3mM) proved to form fibers [fig. 3.16].

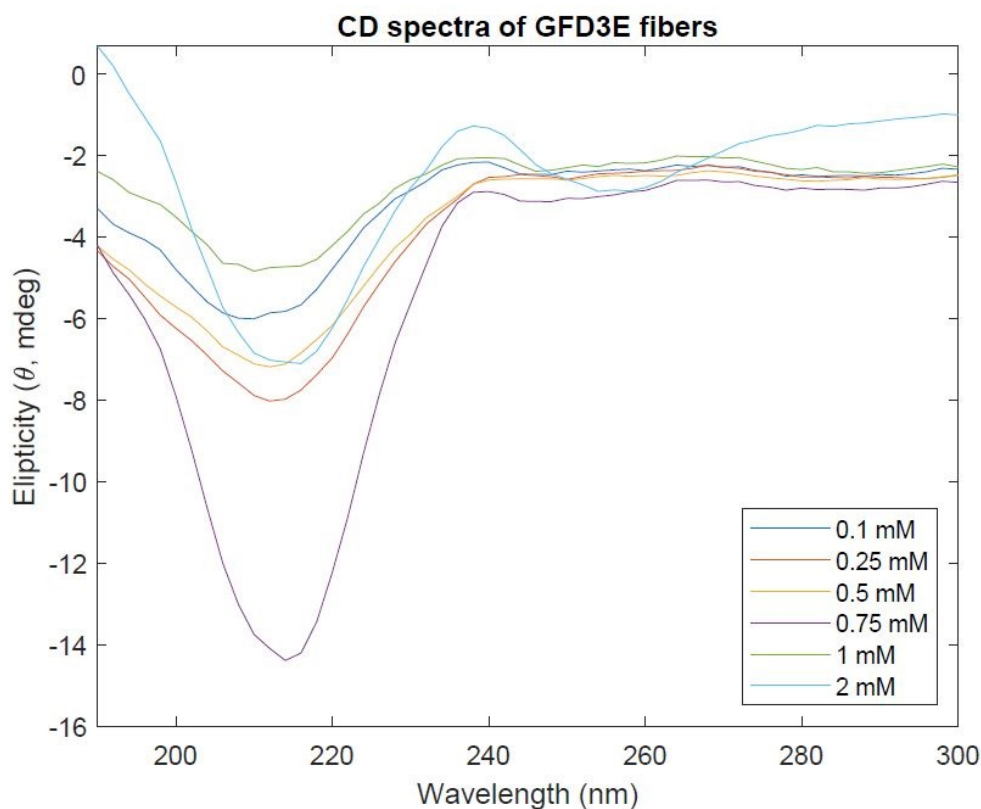


Figure 3.16: CD measurements of solutions 0.1 mM, 0.25 mM, 0.5 mM, 0.75 mM, 1 mM, 2 mM. A global minimum at 218 nm indicates presence of β -sheets. 0.75 mM represents de dilution where a larger number of fibers are present.

Focusing on the global minimum between 200 and 220 nm an increase concentration leads to an increase in the signal until 0.75 mM concentration is reached; then signal is decreased. A local minimum followed by a local maximum can only be appreciated for 0.75 mM and 2 mM samples. A minimum at a wavelength of 260 has been associated to the presence of aromatic rings.

3.5 Fluorescence spectroscopy

In this study, a first attempt to measure emission of the fluorenyl group was performed getting as result an emission peak at 325 nm of wavelength. There is some disagreement when studying the emission wavelength of the free fluorenyl groups. Some studies have associated its emission peak at 313 nm [67], [68] while the interacting fluorenyl group in an antiparallel manner is associated to an emission peak at 325-330 nm. On the other hand, other studies have suggested the emission peak of a free fluorenyl group appears at 320 nm [11], [69], or that antiparallel assembly of the fluorenyl group translates into an emission peak of 360 nm and parallel organization into a peak at 396 nm [8].

Fluorescence emission spectrum was done in order to study the environment surrounding the F-moc groups of the peptides in the GFD3E fibers. The results obtained can be seen in fig. 3.17.

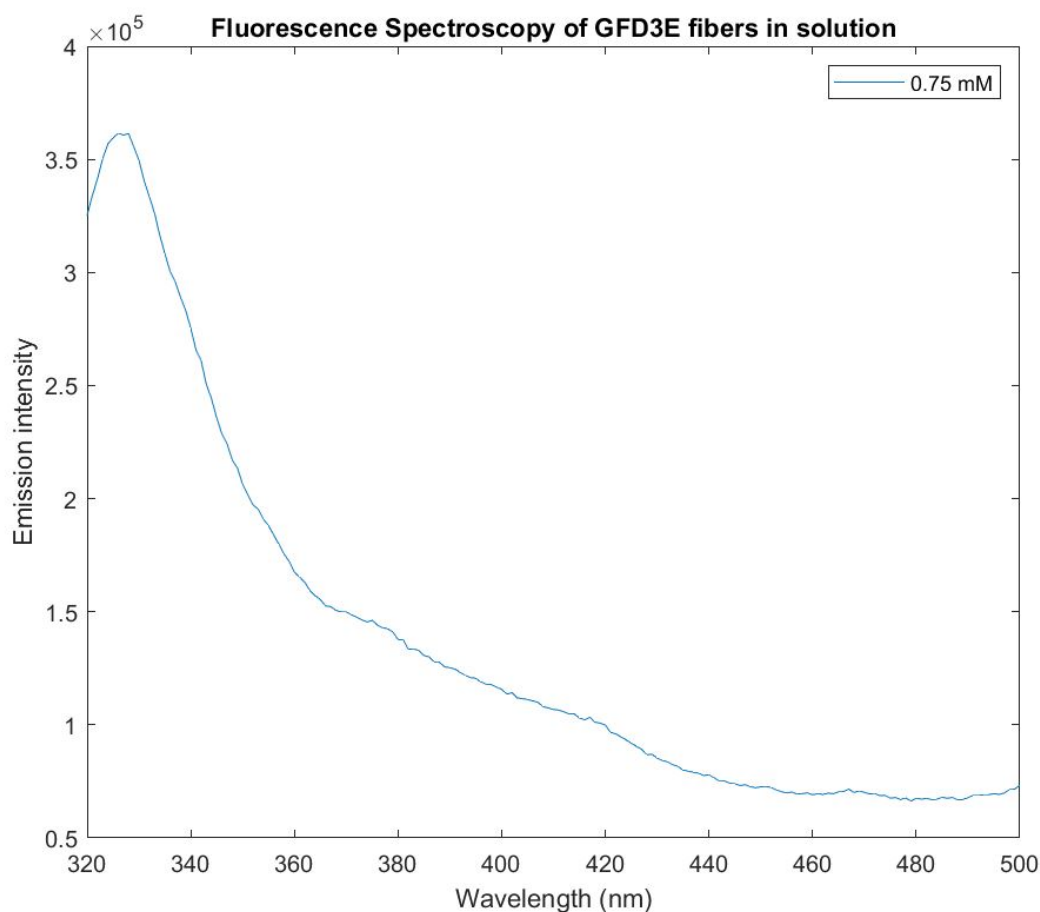


Figure 3.17: Fluorescence emission spectrum of GFD3E peptides at a concentration of 0.75 mM. The spectra shows a peak at 325 nm indicating that the fluorenyl rings groups are free in solution. No peak at 460 nm is seen.

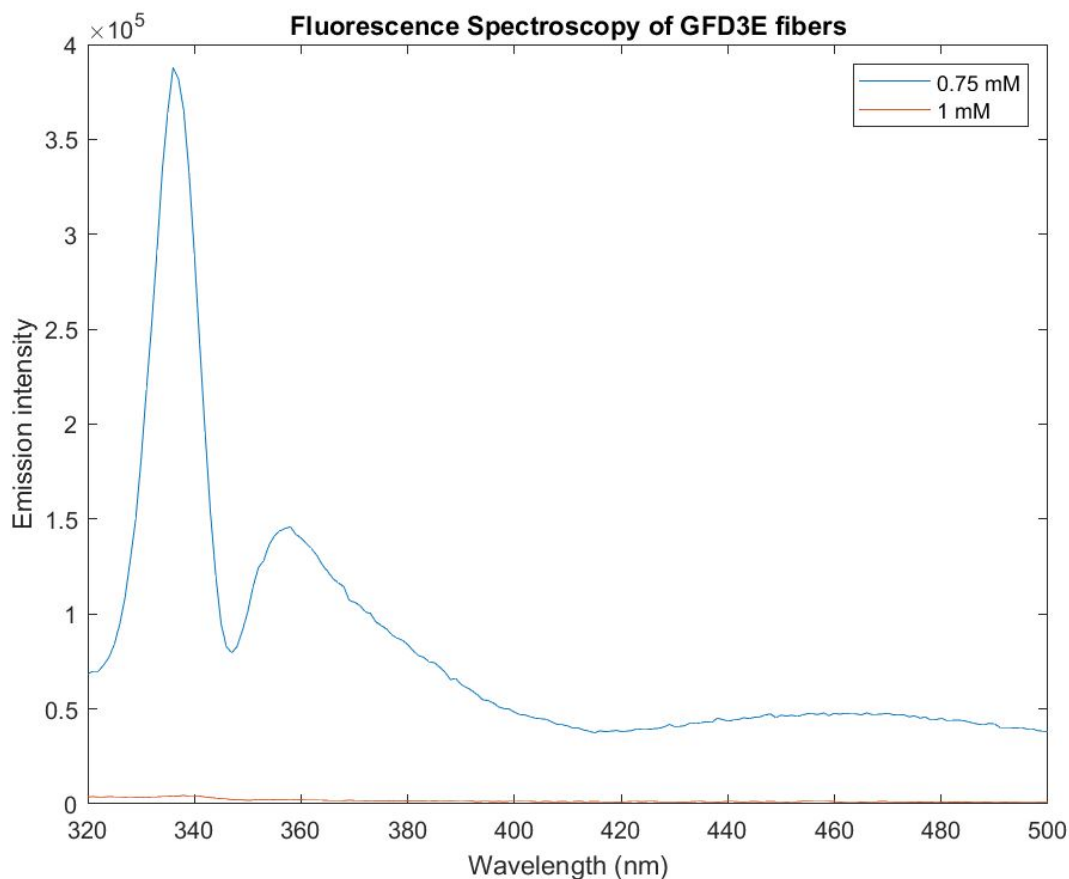


Figure 3.18: Fluorescence emission spectrum of GFD3E fibers at a concentration of 0.75 mM, 1 mM and white sample. Sample at 0.75 mM GFD3E show the higher intensity peak at 336 nm. No peak at 460 nm is seen.

A large difference on intensity between the 1 mM and the 0.75 mM concentrations is seen when the solution is precipitated on quartz wafers [fig. 3.18]. Counter-intuitively, the sample with higher concentration of peptide (1 mM) had the lower emission values. The sample with 0.75 mM of peptide brought the largest values of emission. As can also be seen, a small emission peak at 360 nm of wavelength can be seen but do not modify the main peak [fig. 3.18]. The larger emission value appears at 336 nm wavelength for all the samples analyzed. Again, the emission peak at 460 nm is missing.

The two different methods of preparation of the samples led to different results red-shifting the peak of higher intensity [fig. 3.19]. A smaller emission peak at 360 nm of wavelength is seen clearly only for the precipitated samples even though the samples in solutions show a very broad emission peak and still high intensity on that region.

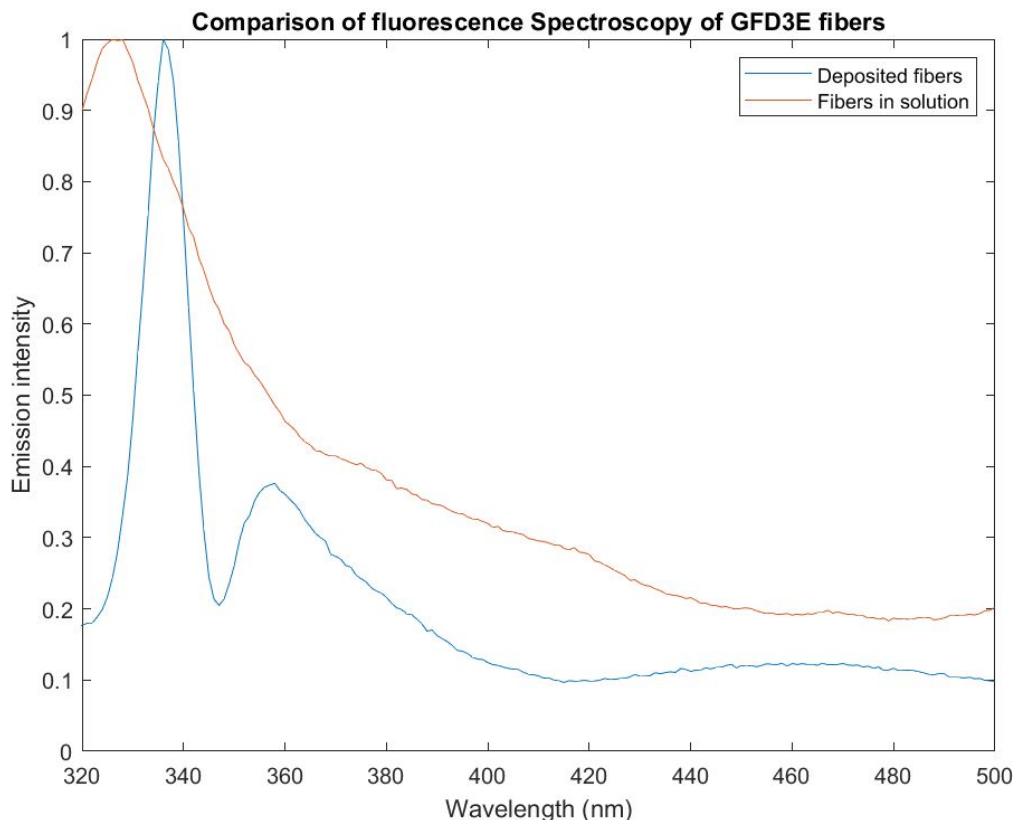


Figure 3.19: Fluorescence emission spectrum of GFD3E fibers at a concentration of 0.75 mM prepared by both methods (in solution and in solid state). The red-shift of the higher intensity peak can be easily observed. Data was normalized in order to have an easy appreciation of the displacement.

Quartz wafers were observed on the AFM to assess the coverage of the substrate and shed some light on the large difference of emission intensity observed between the different concentrations. Coverage was rather low for all samples compared to the ones observed on the AFM with Silica-oxide substrates. An image representative for each sample can be seen in fig. A.9. Sample at concentrations of 0.5 mM and 1 mM of GFD3E led to a very low or null coverage respectively, while sample at 0.75 mM GFD3E, while low coverage compared to the silica oxide wafers, had a larger one compared to the quartz wafers at other concentrations, explaining why the intensity of emission was so high.

3.6 Atomic Force Microscopy

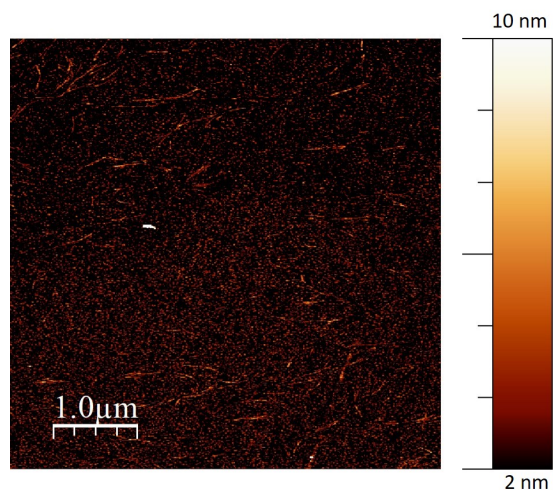
As stated in section 2.5, two methods were used to analyze the samples on the AFM. In the first method, the wafers were incubated with the sample for 24 hours prior to analysis while in the second method the incubation time was only of 20 minutes. These two methods led to very different results regarding coverage. The results obtained are presented below.

Two different concentrations were prepared by method 1 (incubation time of 24 hours), 3 mM and 2 mM of GFD3E peptide solutions. Images obtained on the AFM were not clear showing a background with a large number of impurities. No images were taken

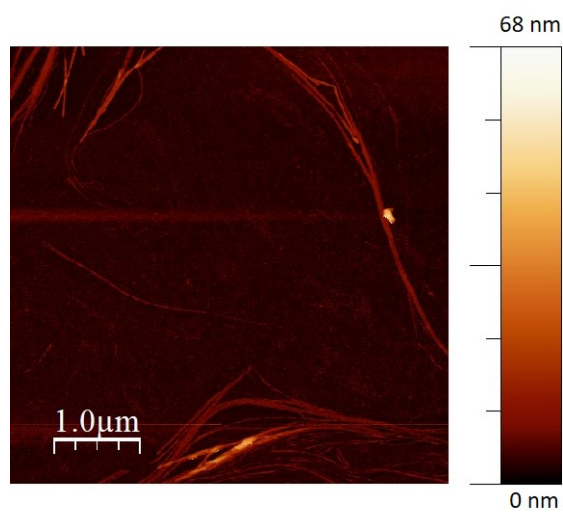
on the 3 mM concentration since the tip of the cantiliver was constantly being adhered to the surface. Hence, only images of the 2mM GFD3E solution were obtained [fig. 3.20].

Samples prepared by method 2 presented a more clear background since the incubation time was shorter and particles from the air had little time to precipitate on the substrate. Yet, this little short incubation time led to a lower coverage of the substrate. CD measurements proved 0.75 mM GFD3E to be the solution with a higher number of fibers (see section 3.4) so this dilution together with 1 mM GFD3E were analyzed[fig. 3.21].

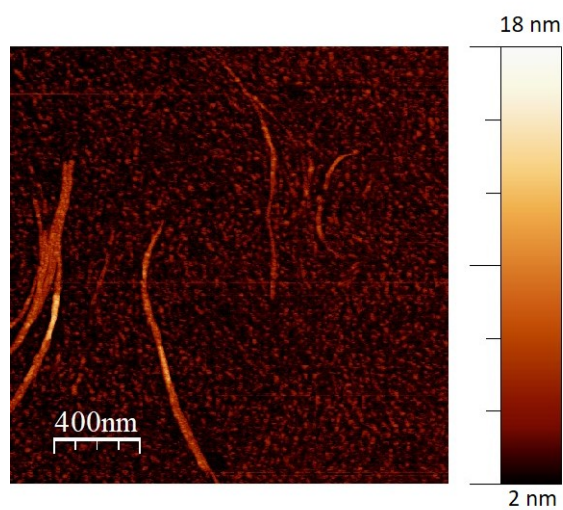
Having now a clearer background the height profile of the samples was analyzed. In order to measure the height, the software WsXM 5.0 Develop 10.0 was used. The selection of the fibers to analyse was done based on their clarity in the image, always trying to study the larger number of fibers possible. Once a fiber/group of fibers was selected, in a zoom-in image a profile was taken. In order to obtain the profile, perpendicular lines to the fiber were used, alongside which the software will measure the different heights. For each fiber, 12 height profiles were obtained along its longitudinal axis to ensure that all the fiber was covered in the analysis. The value obtained was introduced in an Excel file where the average and the standard deviation were calculated for each fiber and for the total of the fibers analyzed in the image. An example of the mechanism as well as the profile obtained can be seen in fig. 3.22.



(a)



(b)



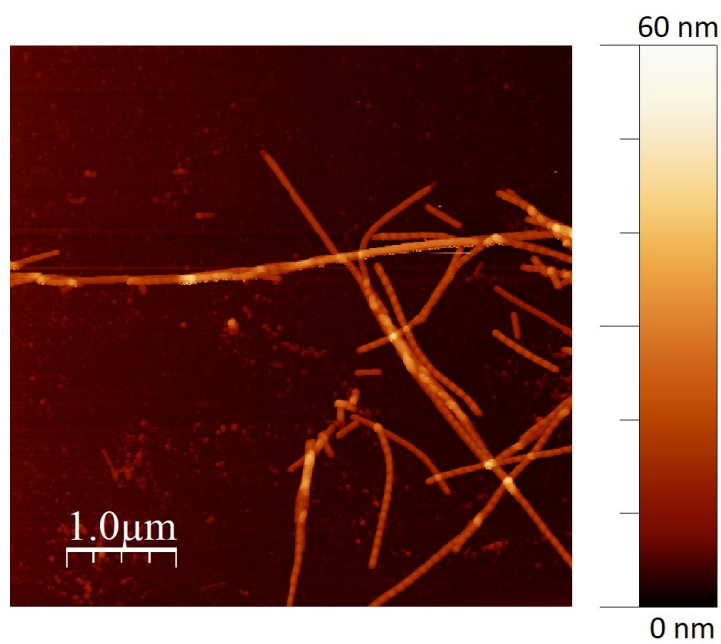
(c)

Figure 3.20: AFM images of samples obtained by method 1 (incubation for 24 hours). All images were taken from the same sample, 2 mM GFD3E concentration. Images have been modified in order to facilitate the interpretation.

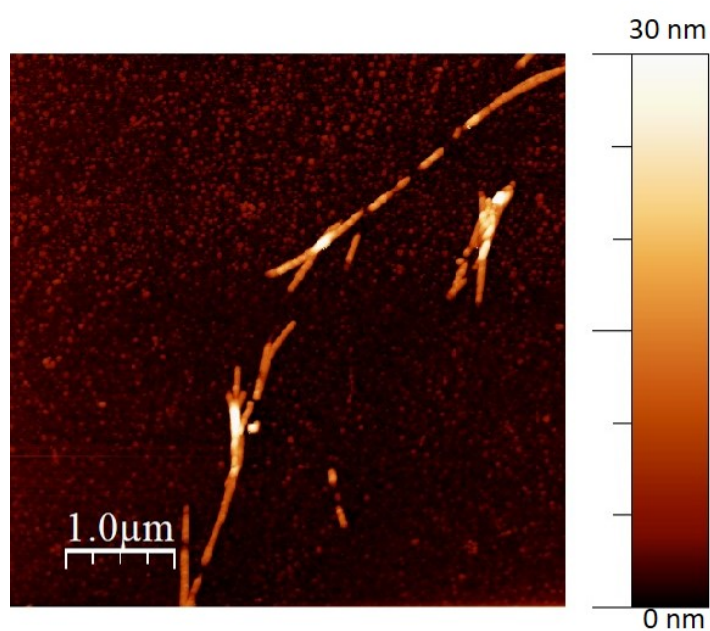
Height profiles were taken for the samples at 0.75 mM and 1 mM. A notable difference in height as well as length of the fibers can be seen between the two concentrations. The fibers at a dilution of 0.75 mM were observed as being longer and with larger values of height, while the fibers at a dilution of 1 mM were notably shorter and smaller in height. Values of the height profile can be seen in table 3.2.

	0.75 mM dilution	1 mM dilution
Fiber 1	14.26 +/- 1.7 nm	9.43 +/- 3.4 nm
Fiber 2	13.78 +/- 1.2 nm	6.53 +/- 0.7 nm
Fiber 3	13.75 +/- 1.4 nm	6.12 +/- 0.78 nm
Fiber 4	11.85 +/- 1.1 nm	6.99 +/- 1.2 nm
Fiber 5	17.65 +/- 2.1 nm	4.53 +/- 0.75 nm
Fiber 6	16.2 +/- 2.1 nm	7.64 +/- 0.7 nm
Fiber 7	17.55 +/- 1.8 nm	8.18 +/- 0.8 nm
Total	15.0 +/- 2.0 nm	7.03 +/- 1.3 nm

Table 3.2: Table with the values obtained of the height analyses for each sample analyzed. Number of fibers obtained for dilution 0.75 mM was 11 but for clarity only 7, the number of fibers analyzed for dilution 1 mM, are shown.



(a)



(b)

Figure 3.21: AFM images of samples obtained by method 2 (incubation time of 20 minutes). Images were modified to ease the interpretation. Images of 0.75 mM GFD3E a) and 1 mM GFD3E b) were the difference on coverage can be easily seen. There is a large difference on the number, the length and the height of fibers between the two samples. A periodicity can be glimpsed on image a) but can't be seen in b).

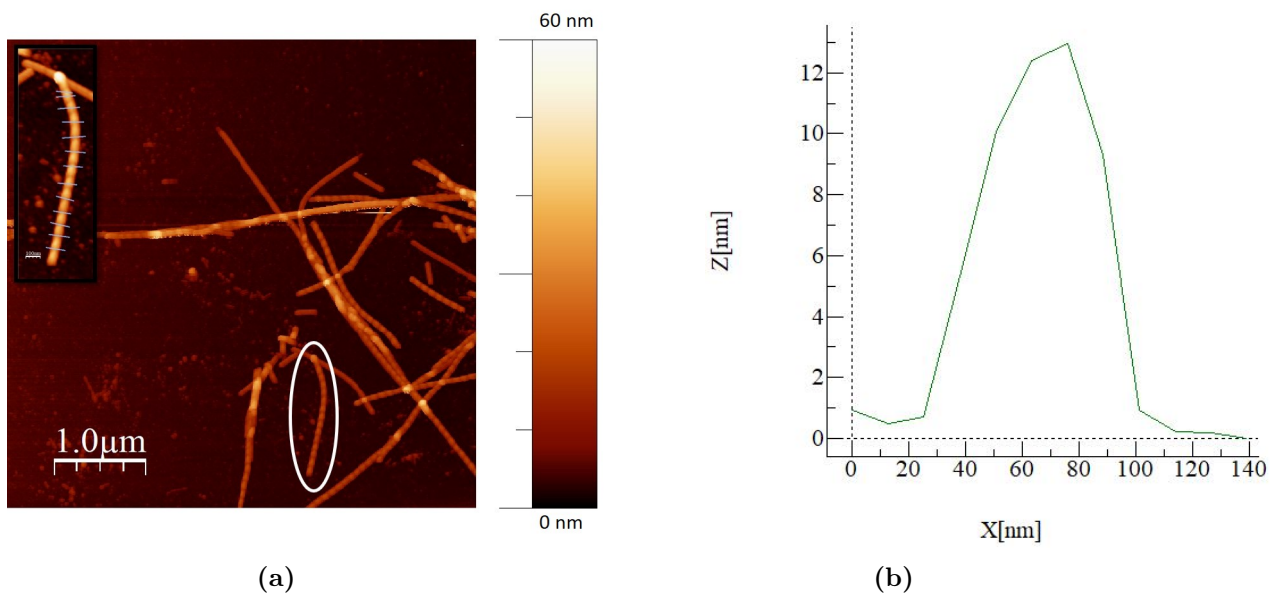


Figure 3.22: AFM images of samples obtained by method 2 (incubation time of 20 minutes). Images were modified to ease the interpretation. a) Image of a sample diluted at 0.75 mM. The fiber enclosed by a white parabola represents the fiber used for the analysis. The inset in image a) represents the process of calculating the average height of the fiber. A homogeneous sampling along the fiber was used in order to ensure validity of the results. A profile line was drawn from a dark spot (low height) near the fiber to another dark spot going through the fiber. In image b) an example of one calculated profile line is represented. The peak of these profiles were used as height value for the fiber and introduced in an Excel file where statistical analysis was done.

Analyzed fibers showed a periodicity along its longitudinal axis where brighter areas are separated by darker areas, representing a change in height. To demonstrate this behaviour a height profile line along the fiber was used. The process followed as explained earlier, only that the purpose of this analysis was not to obtain analytical values but to see this periodicity in a more clear way [fig. 3.23]. Distance between this brighter and darker areas is rather difficult to estimate due to the nature of the cantilever tip.

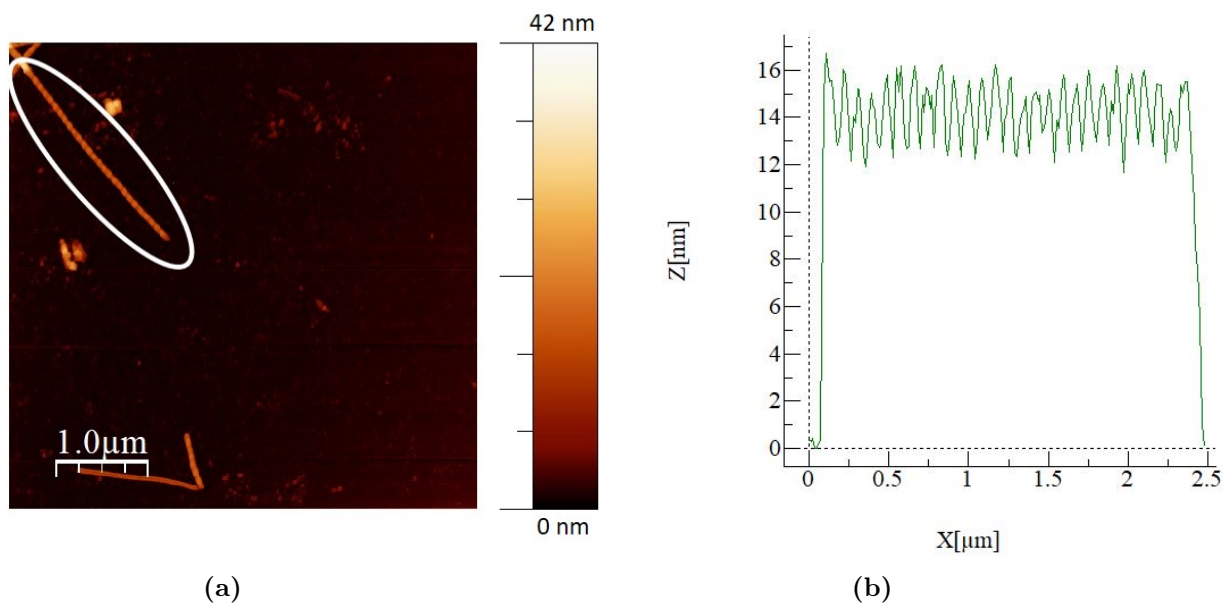


Figure 3.23: AFM images of samples obtained by method 2 (incubation time of 20 minutes). Images were modified to ease the interpretation. a) image of a sample diluted at 0.75 mM with the fiber upon periodicity analysis was performed. The fiber enclosed by a white parabola represents the fiber used for the analysis. b) Profile curve showing the periodicity in height of the fiber enclosed by a white parabola in a). A profile line was used along the axis to see the difference in height along the longitudinal axis of the fiber.

3.7 Silver coating of GFD3E nanofibers

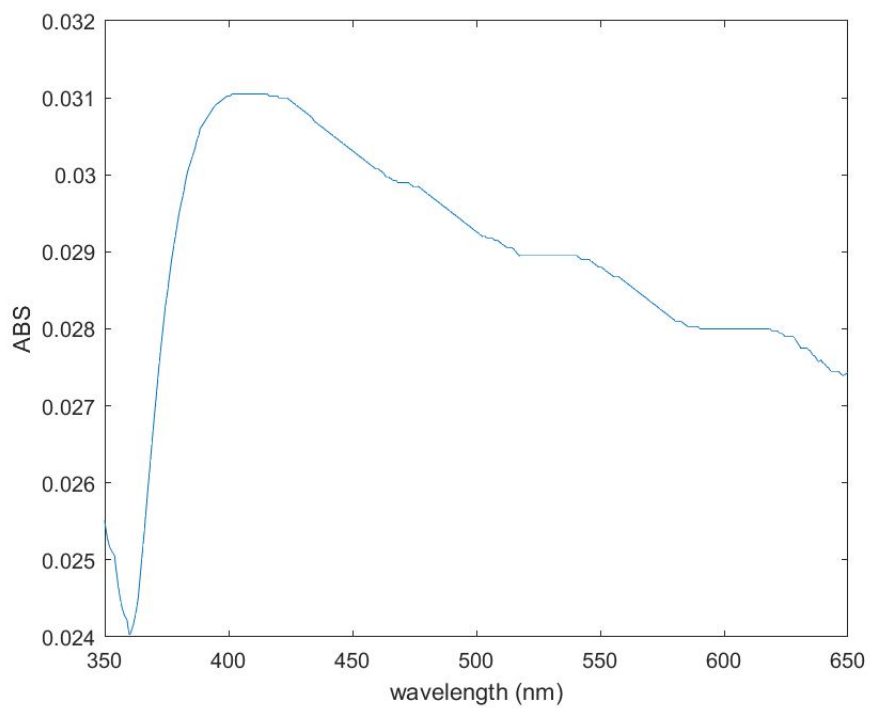
GFD3E fibers were attempted to be coated with silver nanoparticles. In order to study the coating of the fibers, absorbance and visual examination was done. An absorption spectrum ranging from 700 nm to 300 nm wavelength was performed after each experiment. Visualization of the result was done in both AFM and Surface Electron Microscope (SEM). AFM allowed a more detailed visualization of the fibers and the silver nanoparticles (AgNPs) and the samples were later visualized in the SEM to assess whether the fibers had been coated and to what extent. Only conductive material is seen under the SEM in a bright light, otherwise the artifact will appear as a dark shadow.

Different attempts were made to coat the GFD3E fibers with silver nanoparticles but only a some of them will be shown in this section. They represent the variety of results obtained throughout the attempts. It is worth mentioning that right after the coating procedure was finished, an absorption spectra was taken from all samples and only those that lead to a promising curve were selected to be visualized in the AFM and the SEM. This is the reason why for some results only absorbance data will be given. The different attempts with their respective visual characterization (when applied) will be presented on a chronological order.

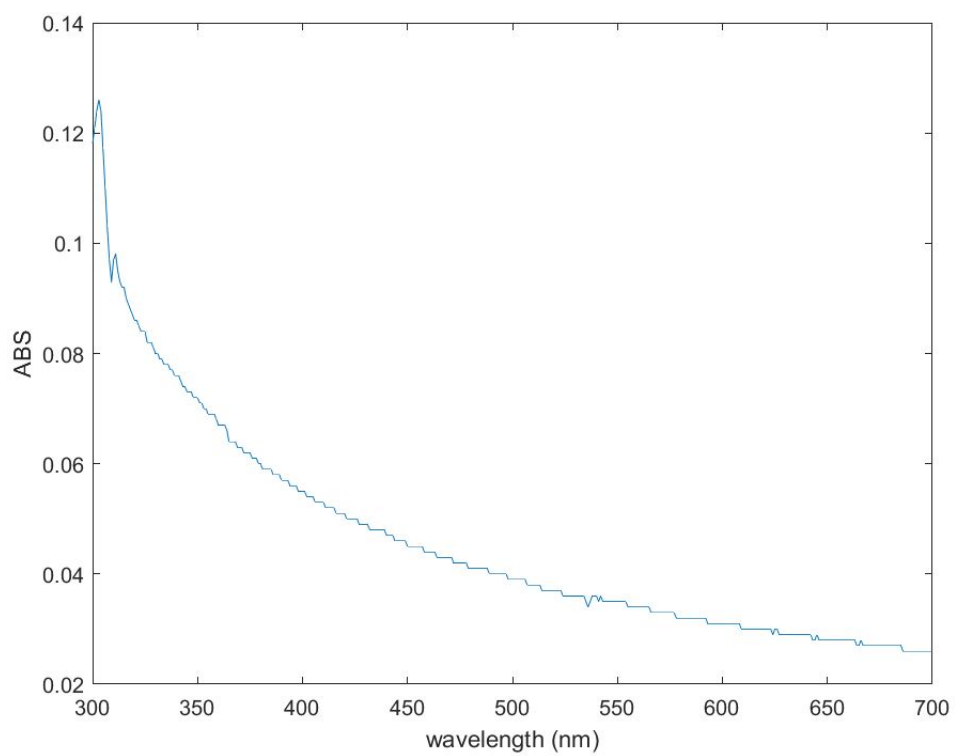
Attempts	Protocol	AFM/SEM
Attempt 1	Protocol 1	-
Attempt 2	Protocol 2 (dark)	fig. 3.31
Attempt 3	Protocol 2 (light)	fig. 3.26
Attempt 4	Protocol 3	fig. 3.27
Attempt 5	Protocol 4	fig. 3.28
Attempt 6	Protocol 5	fig. 3.25
Attempt 7	Protocol 6	fig. 3.31
Attempt 8	Protocol 7	fig. 3.29
Attempt 9	Protocol 8	fig. 3.30

Table 3.3: In this table each attempt is related to their respective protocol and for those that a visual analysis is done, to the respective figure. All attempts except attempt 1 have visual analysis that can be seen either on the results section referenced accordingly.

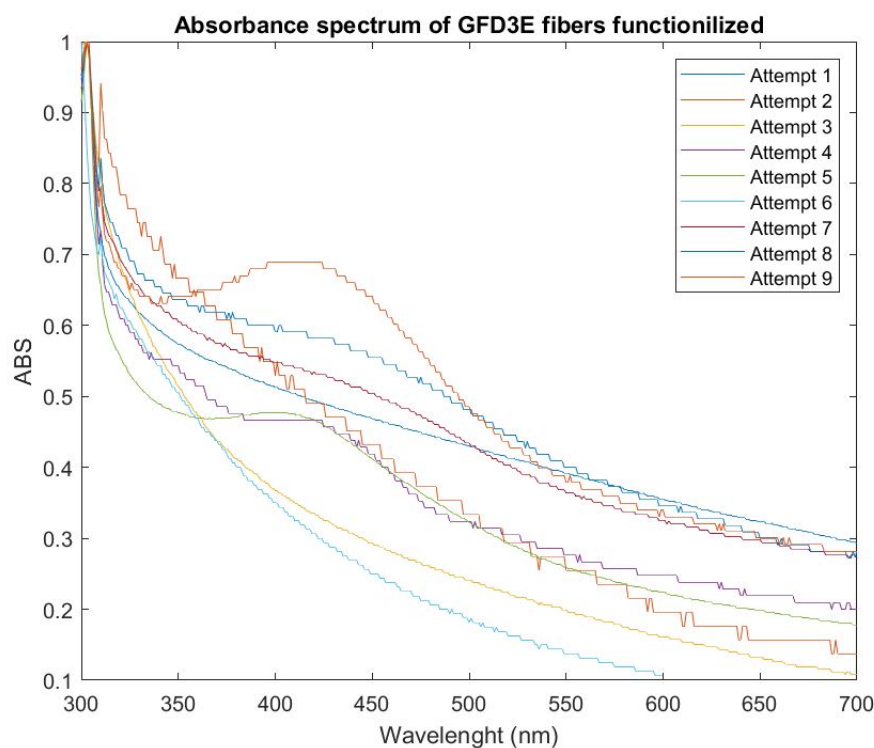
The first results presented will be the absorbance spectra obtained for each one of the attempts and the absorbance spectrum of the GFD3E fibers and AgNPs alone [fig. 3.24]. A clear peak between 400 and 450 nm can be seen for the AgNPs, although a tail on the red side can be appreciated. On the other hand, when GFD3E fibers were analyzed, no peak is observed between 400 and 500 nm (area at which AgNPs often absorb). Regarding the functionalization attempts, only a few of the showed a clear peak at the interval desired, while most of them had a broad peak of a low intensity that expands from 400 to 500 nm.



(a)



(b)



(c)

Figure 3.24: Absorbance spectra of a solution of GFD3E fibers (b) and silver nanoparticles (a) alone and all the different attempts together (c). The GFD3E fibers solutions was prepared just before a coating attempt but no solution of AgNO_3 or NaBH_4 was added to the vial. The AgNPs were prepared as explained in the protocol 5 in section 2.7 but without introducing the solution of GFD3E peptides.

The first attempt led to no absorbance peak what discarded it from further visual characterization, the same tendency on the absorbance was seen for attempt 3 and 6. Because of the same tendency was seen three different times for three different protocols, visual characterization of attempts 3 [fig. 3.26] and 6 [fig. 3.25] was done in both AFM and SEM.

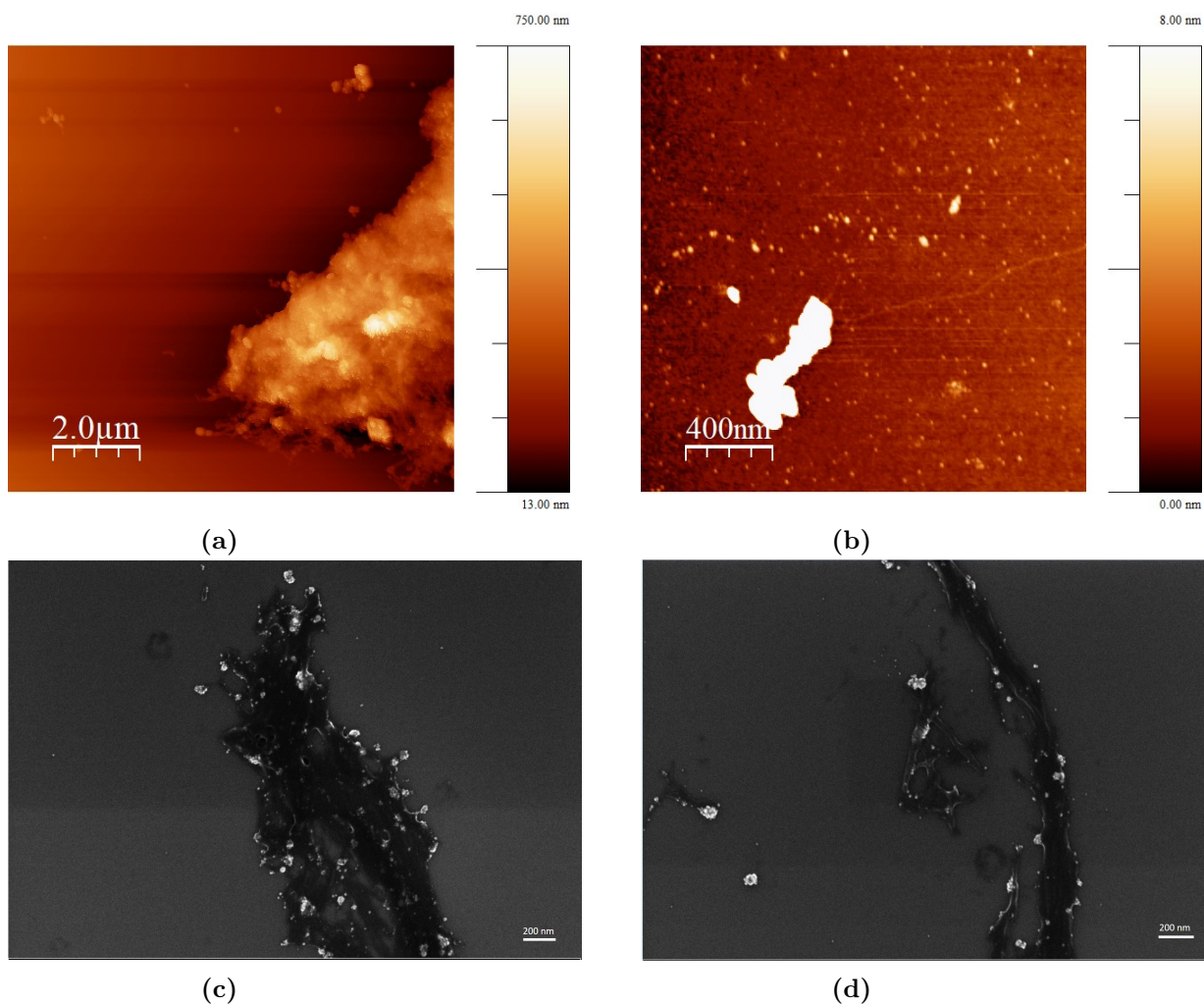


Figure 3.25: AFM (a, b) and SEM (c, d) images of attempt 3. A group of rather big silver aggregates (a) can be seen as well as small silver nanoparticles (b). In the SEM images on the other hand, none or little coverage of GFD3E fibers can be seen.

In attempt 6 both very large clusters and free silver nanoparticles and aggregates could be observed. In the AFM images no free fiber was located contrary to the visualization in the SEM, where a large number of free and aggregated GFD3E fibers were found; most of the uncovered with some of the fibers fictionalised but with a very lo coverage with silver nanoparticles.

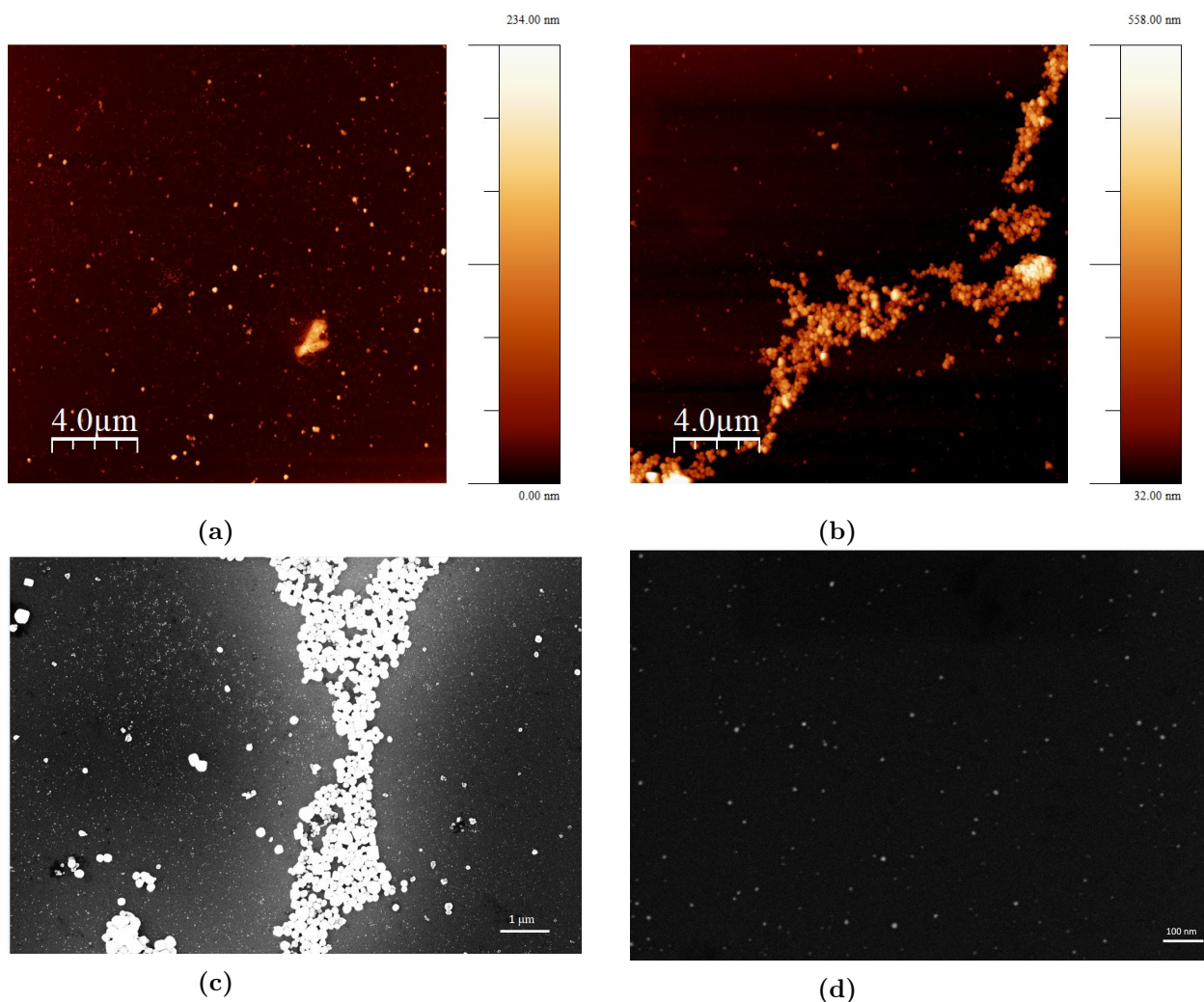
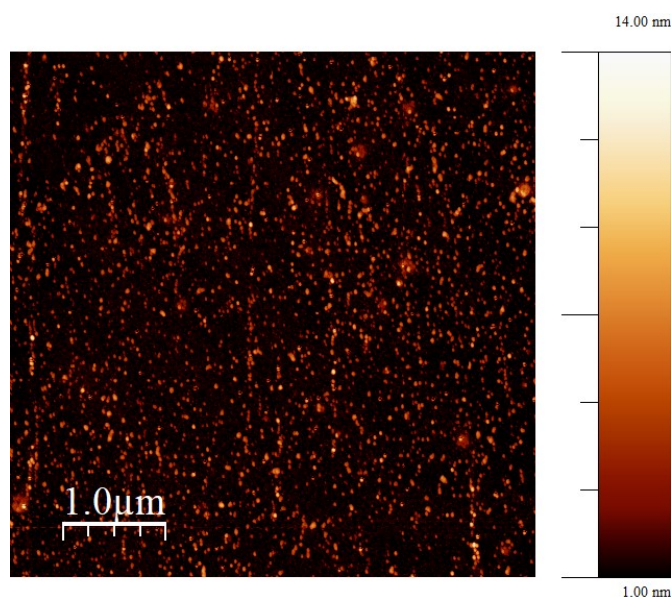


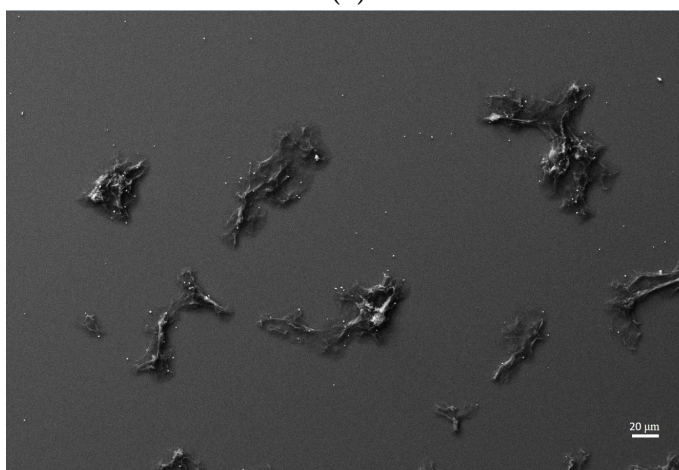
Figure 3.26: AFM (a, b) and SEM (c, d) images of attempt 6. Big silver aggregates can be seen mixed with small silver nanoparticles. Silver aggregates are mainly present in this sample, since the z-scale on the AFM images ranges from 0 nm to 234 nm (a) and 558 nm (b).

Attempt 3 and 6 led to very interesting and contradictory results. On the absorbance spectrum no peak is observed and yet, when the sample is studied in the AFM and in the SEM silver nanoparticles as well as silver aggregates are seen in either instrument. A tendency to aggregation can also be seen for both SEM and AFM images, although a large number of free silver nanoparticles and silver aggregates can be observed. As stated before, the analysis in the AFM allows for an estimation of the height of these silver nanoparticles. The size observed has a large range since sizes from approximately 100 nm to 12 nm can be calculated.

On the contrary, the attempts that led to a most clear peak around 400 nm were attempt 4, 5, 8 and 9, figs. 3.27 to 3.30 respectively.



(a)



(b)

Figure 3.27: AFM (a) and SEM (b) images of attempt 4. Large number of AgNPs can be observed in the AFM image. On the SEM image structures that look like GFD3E fibers can be seen, although these structures are too big for being fibers.

Attempt 4 led to a large number of silver nanoparticles that are seen in an absorbance peak at 414 nm. No fibers were found in the AFM images, unlike for the analysis on the SEM. Large aggregates of GFD3E fibers were spotted but those had none to very little coverage with AgNPs. At the edges of the aggregates, some AgNPs can be seen clustered, but it is not uniform in the aggregate itself or in the sample.

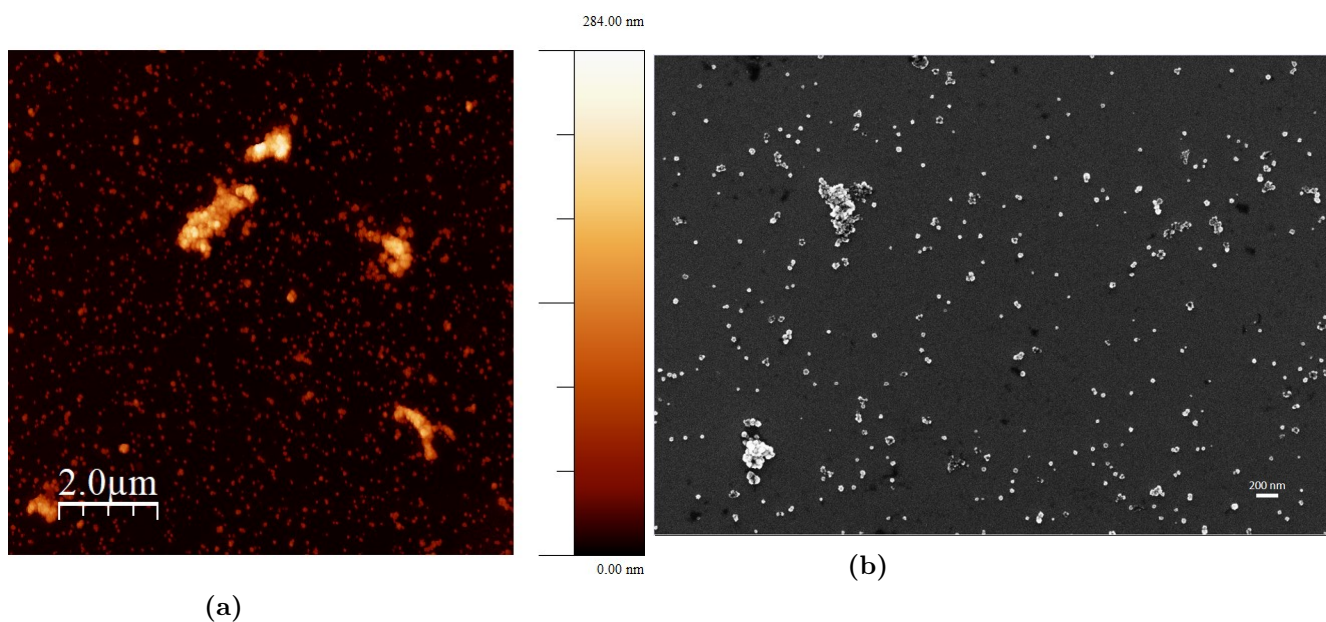


Figure 3.28: AFM (a) and SEM (b) images of attempt 5. Large silver aggregates can be spotted alongside free silver nanoparticles.

In the visualization of attempt 5 relatively large silver aggregates can be seen surrounded by free AgNPs. No GFD3E fibers were found neither in the AFM or in the SEM.

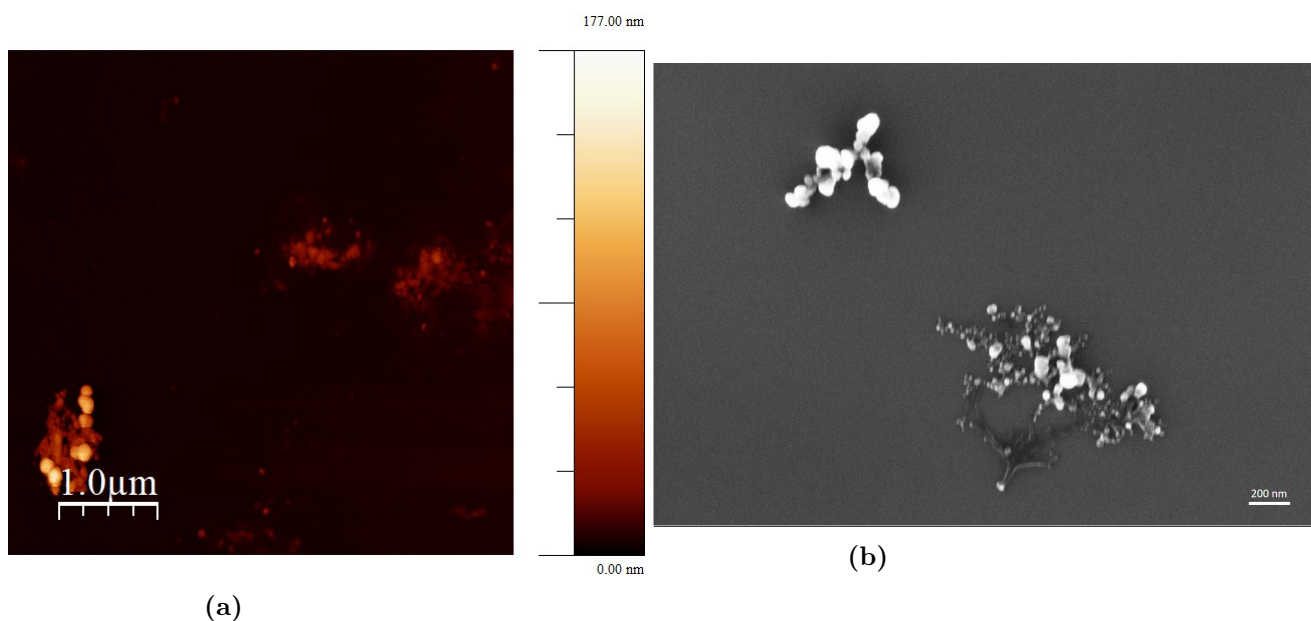


Figure 3.29: AFM (a) and SEM (b) images of attempt 8. Some silver aggregates are spotted in both the AFM and in the SEM. Almost no free AgNPs can be seen.

On the visualization of attempt 6 a large number of aggregates were observed with very little free AgNPs. These aggregates, nonetheless, are not amorphous as the ones seen in other samples, they seem to have a shape very similar to a group of fibers.

Despite no isolated fibers were found, all the aggregates presented AgNPs attached to them in the totality or in some areas along the aggregate.

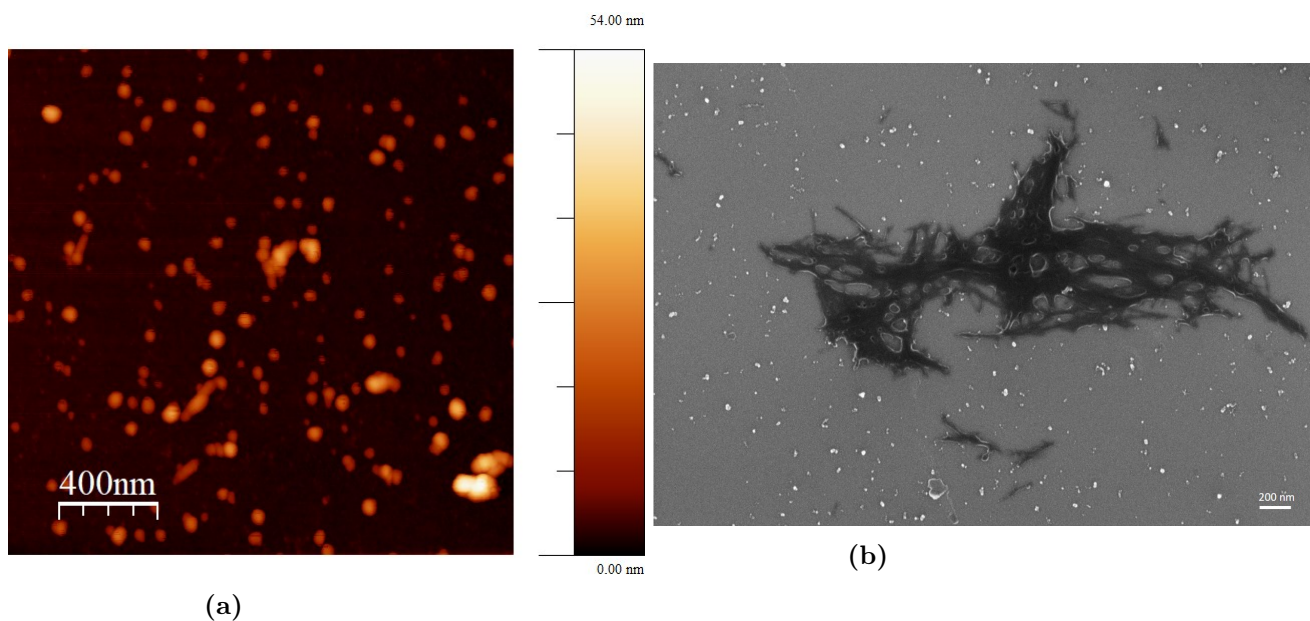


Figure 3.30: AFM (a) and SEM (b) images of attempt 9. A large number of AgNPs can be seen in images taken in either instrument. The fibers found in the SEM image are aggregated and not covered by silver.

The last of the attempts, attempt number 9, led to the synthesis of a large number of AgNPs with a very similar size but no fiber was found to be coated with them. No fiber could be clearly visualized on the AFM, but those found in the SEM showed no indication of AgNPs interacting with them.

Attempt 2 and 7 were only visualized on the AFM. Small aggregates in a fiber-like shape on both sample with very few silver aggregates or free AgNPs surrounding them can be spotted for both samples. These aggregates seemingly of GFD3E fibers are rather big since for both samples those range up to the order of 100 nm.

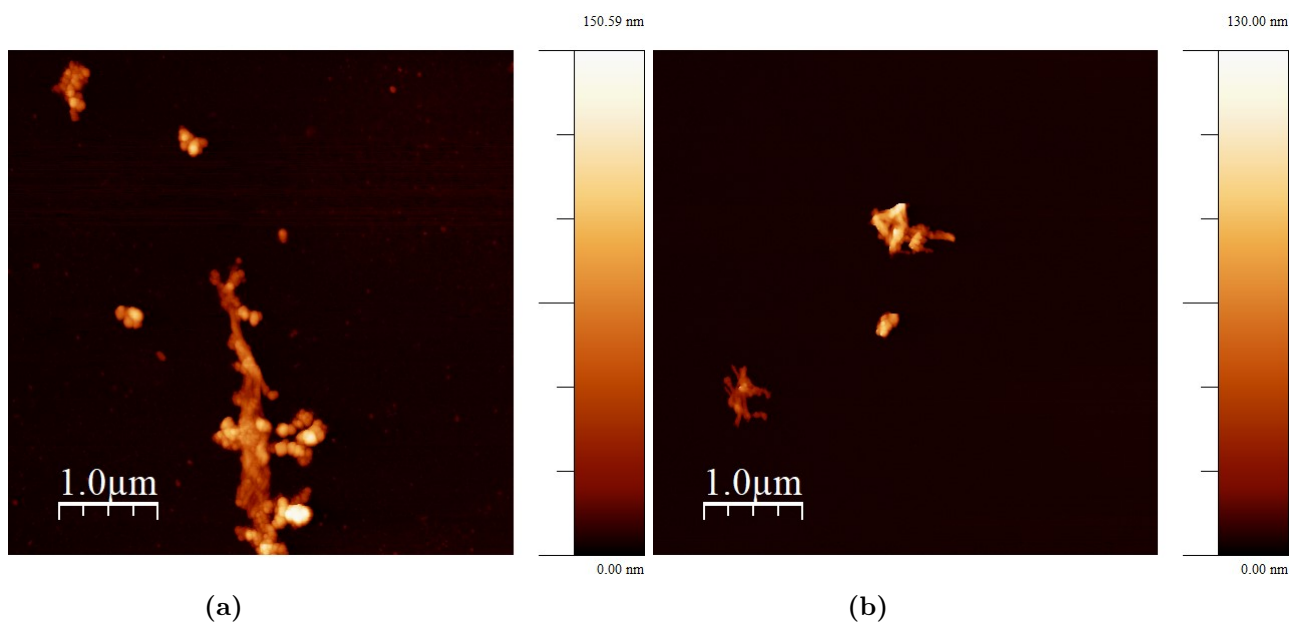


Figure 3.31: AFM images of attempt 2 (a) and 7 (b). Very little number of AgNPs can be seen as well as very few aggregates. For both samples, the height of the aggregates is around 100 nm.

DISCUSSION

4.1 GFD3E as a self-aggregating peptide

GFD3E peptide is comprised of glycine, phenylalanine, aspartic acid and glutamic acid. These four amino acids give the GFD3E peptide the amphiphilic characteristic regarded as crucial for an ordered self-assembling [32], [70], [71].

In the GFD3E peptide case, the hydrophobicity is brought by the phenylalanine residues which contain an aromatic ring (a rather hydrophobic component) which will as well introduce some ordering and constraints [72]–[74] on how these peptides will interact with one another; and by the presence of the F-moc group (which had not been removed for the experimental part but was not present in the MD simulations). The F-moc protecting group was left in the final peptide to increase its hydrophobicity and to be used to identify the orientation of the peptides inside the amyloid fiber [67], [75].

On the other hand, the hydrophilicity of the GFD3E peptide is given by the presence of the glutamic and aspartic acid. These two amino acids are placed strategically so they will always face the same side in a β -fiber (the outside face in contact with the solvent), in such a way that the fibers will not precipitate and will be soluble in water or any hydrophilic solvent (required for the peptide to self-assemble). Aspartic and glutamic acid were selected for their low pKa placed around 4 for both of them. This will grant the peptide three negative charges that can be used for a future functionalization of the fibers. On the other hand, the presence of negative charges will induce repulsion of the peptides in the self-assembling process so their number must be taken into account when studying the self-aggregating properties of GFD3E peptide.

4.1.1 MD simulations

Once the design of the GFD3E peptide was done and tailored to the objectives of the project, Molecular dynamics simulations were performed in order to study the behaviour of the peptide in different conditions. A self-aggregating system is difficult to simulate due to its required big size, hence, an atomistic simulation was prohibitive. Instead, a coarse-grain simulation was performed to study whether the peptide will first aggregate and whether these aggregates will be ordered or not. This step of coarse-graining comes with a penalty on the precision of the results since a peptide with 109 atoms is reduced to 19, hence some physical-chemical properties are lost [76]. The simulations were done in water and in ethanol (as a replacement for acetonitrile, the solvent used in the experimental part).

By simulating the self-assembly of the GFD3E peptide a tendency to aggregate was of course expected since the peptide had been designed for such purpose; but not only was expected to aggregate but was expected to do so in ordered fibers of which morphology could be studied. The aromatic rings of the phenylalanine residues were

expected to be found buried in a hydrophobic core that would extend along the fiber longitudinal axis while the aspartic and glutamic acid were expected to be found interacting with the solvent molecules while being screened by the sodium ions introduced in the system. The results obtained from the simulations are very optimistic in terms of aggregation power, but led to no ordered structures. After the 20 ns MD simulation, several aggregates were found along the simulation box but none of them had an ordered structure [fig. 3.4]. It is worth to mention that while having a fiber-like morphology, a single ordered fiber was not found, rather, the aggregates seemed to pack the hydrophobic residues to reduce their interaction with the solvent molecules in a random fashion. Some simulating environments had not reached an equilibrium before the 20 ns [fig. 3.3], indicating that an increase on the simulation time is required to achieve such equilibrium. With this time increase, a more ordered aggregates may be seen.

The formation of aggregates can be seen not only by a visual assessment of the final configuration after the simulation, but also by calculating the Solvent Accessible Surface Area (SASA) [fig. 3.5]. In general for either solvent, the calculated SASA value drops as the simulation proceeds indicating that the peptides are aggregating. This decrease is more pronounced when the solvent is water than when it is ethanol due to the partial hydrophobicity of the ethanol molecules, possibly indicating that the aggregates are less compact since solvent molecules will still be able to partially interact with the phenylalanine residues. This behaviour is seen in fig. 3.8 as well. The RDF results are dependant on the volume that each solvent molecule occupies, although the P4 CG bead (water) and the P2 CG bead (ethanol) have the same mass (72 amu) but different volume, being the ethanol molecule smaller. This difference in volume can be a reason why the water molecules are found further away from the peptides. In order to be more realistic, a mixed solvation box with ethanol and water could be used. The use of only water as solvent triggered a strong repulsion of the aromatic moieties towards the solvent and thus, the aggregation was rather fast. If ethanol molecules were to be included together with water, they may slow down the aggregation process giving time for the peptides to properly orient and to form the amyloid fibers [77].

Another analysis that was done in order to track the formation of aggregates is measuring the distance between the glycine residues of the different peptides. Glycine residue was selected since there is only one residue per peptide and it has no side-chain, hence, the location of the glycine residue will be a fairly good reference point for the location of the peptide backbone, henceforth the distance will be considered as distances between peptides and not between strictly glycine residues. Peptides were moved closer to one another with either solvent due to the aggregating power of the aromatic rings but a larger decrease in the distances can be seen when water was used as solvent, probably due to the partial hydrophobicity of the ethanol molecule that is translated in a reduced repulsion of the phenylalanine residues.

The driving force for the aggregation of the peptides seemed to be the reduction on the entropy (a characteristic trait when hydrophobic forces are present). This hypothesis can be seen when first, the type of salt used for the screening is taken into consideration and second when the interaction between phenylalanine residues and solvent molecules is studied. Regarding the type of salt used for charge screening, it is easy to see that when using NaCl, the sodium cations will interact with the negative charges of the aspartic and glutamic acid. This could be appreciated already from the start when preparing the system to be simulated. The system was neutralized so no charge will exist, and for all the systems three times the number of GFD3E

molecules were added of sodium cations (Na^+). That gives the idea that for each negative charge coming from the GFD3E peptide, one cation will screen it, leading to a lack of electrostatic attraction due to bivalent cations interacting with two negatives charges. In order to further test this hypothesis, simulations including divalent ions such as Mg^{2+} , Ca^{2+} among others should be performed. The other hint that the results had given comes from the analysis of the calculated number of contacts between the phenylalanine residues. As can be seen in fig. 3.7 there is a big difference between the evolution of such interaction from the simulation with water as solvent and with ethanol as solvent. As a general trend the number of calculated contacts between the phenylalanine residues and the water molecules is drastically reduced and kept at a low number for the rest of the simulation. On the other hand, when ethanol was used as solvent, such a notable reduction could not be seen. This difference can be explained when the chemical nature of the two different solvent molecules is analyzed. Water is a complete hydrophilic molecules and so will cause a stronger repulsion from the aromatic moieties which will explain why there is larger reduction of the interaction. On the other side, ethanol is not a complete hydrophilic molecule what will ease the interaction between the aromatic moieties and the solvent molecules. Molecule size again has to be introduced in the discussion. The presence of a larger molecule inside the aggregates is less likely than the presence of a smaller molecule. This can be translated to water molecules being kept away from the inside area of the aggregates not only by physico-chemical properties but also by its larger size. The fact that the interactions are in either case reduced indicates that the phenylalanine residues are being protected from the solvent, the type of behaviour that was expected.

If all this information is put together, not only the nature of the driving force can be studied but also it brings some knowledge on the nature of the aggregates. Those will have an inner core sealed or partially sealed from solvent molecules, specially for water molecules.

4.1.2 Experimental study of the self-assembly properties of GFD3E

Simultaneously to the MD simulations, the ability of GFD3E to self-assemble into ordered fibers was tested. Before analyzing the results obtained, a brief comment will be given of the peptide synthesis.

The HPLC done after the synthesis showed two different absorbance peaks similar height fig. 3.15. These two absorbance peaks may come from the presence of two different peptides in the final solution. One reason for a truncated peptide can be the formation of D/L-aspartimide [78]–[80] which will eventually react with the N-terminal of the amino acid preventing any other amino acid from being introduced in the sequence. Another reason could be the aggregation of peptides inside the peptide synthesizer due to the presence of highly hydrophobic residues [81]. GFD3E peptide is designed to have a strong aggregation power so the fact that some peptides aggregated during the synthesis and that led to the formation of two different components cannot be ignored. If the exact composition and sequence of the synthesised peptide are to be known, a MS/MS spectrometry will be a fairly easy study to obtain such information [82], [83]. Once the sequence is known, the problem can be sorted. One solution to the aggregation problem proposed in the literature is the use of microwaves irradiation. Microwaves will accelerate the reactions by rotating the molecules what

will increase the temperature of the system helping to overcome kinetic barriers. Another advantage is that peptides were found to orient themselves aligning with the electric field generated by the microwaves, thus, preventing it from aggregating [81].

CD measurements were performed to study whether GFD3E at different concentrations will aggregate into amyloid fibers. Two factors of the peptide can be seen in these experiments. First a positive peak reflecting the presence of phenylalanine was expected at 220 nm [63], [65] but was not reported. The lack of such a peak may come from the presence of β -sheet structure which has been reported to show a negative peak between 215 and 220 nm [34], [37], [64], [84]. Visualization of different dilutions of GFD3E peptides in the AFM, confirmed the presence of amyloid fibers and showed a notable difference between 0.75 mM and 1 mM dilutions regarding the coverage of the wafers [fig. 3.21]. Visualization of 3 mM was attempted but unsuccessful since the sample was in a gel-like state. The larger number of fibers and thinner and longer morphology were the reasons why 0.75 mM was chosen to be the concentration to work for the next analysis.

Visualization of the samples in the AFM allowed for a better understanding of the morphology of such fibers. Moving the focus now to the 0.75 mM dilution, the amyloid fibers had a length of the order of micrometers and a diameter of approximately 15 nm, which falls in the range of diameters found elsewhere [5], [7]. Measuring the height of the fibers prepared at 1mM GFD3E led to a rather interesting information. These fibers were shorter and had a smaller height. A possible explanation for such behaviour can be attributed to the access of the aromatic moieties to water. When a fiber increase in length the aromatic residues placed somewhere far from the edge are less affected by the solvent since they are better protected than those located at the edges of the fiber. This may translate to a more relaxed structure towards the center of the fibers moving the aromatic residues far from each other, while on the extremes or areas where the solvent is in close proximity, the aromatic residues are moved tightly in order to reduce as much as possible the entropy of the system [85]. This will be in agreement with the results from the MD simulations [fig. 3.5 and fig. 3.7] where the presence of water made the aggregates be more compact. Another possibility is that this change in height is simply due to the stacking of one fiber on top of another due to the larger coverage. Another interesting trait is the periodicity found in the fibers. This can be seen for a small periodic difference in height. This is done due to the twisting of the β -fibers in a ribbon-like manner in order to form the amyloid fibers. This type of periodicity has been seen elsewhere[86], [87].

Amyloid fibers can interact in a parallel or anti-parallel fashion, condition that was studied by leaving the F-moc group in the final peptide [11], [67], [75]. The results obtained in this study are controversial in terms of, when the samples were measured in a liquid state, a single emission peak appeared at 325 nm describing either the presence of free fluorenyl groups [11], [69] or the presence of antiparallel amyloid fibers [67], [68]. Yet, when the samples were measured in solid state (dried on a quartz wafer) three emission peaks could be seen. The first and the most intense one located at 336 nm, the second one located at 357 nm and a very broad third one located between 440 nm and 500 nm. It is clear that the low intensity broad emission peak appears due to $\pi - \pi$ stacking of the GFD3E fibers. The two other emission peaks left should correspond to the fluorenyl emission peaks. These two new emission peaks have appeared once the sample was dried on a quartz wafer, hence, reducing the number of monomeric peptides analyzed. Furthermore, the peak obtained when the sample was

analyzed in liquid state is rather broad with a long red-shifted tail contrary to the two narrow emission peaks obtained in the deposited sample. The effect of solvent in the fluorescence spectra is well known. Solvent molecules stabilize the molecular excited state red-shifting the emission peak. This red-shift is increased as the polarity of the solvent increases, although aromatic residues are less affected by such phenomenon [88]. Furthermore, if the wavelengths at which the emission peaks are found in [11], [67]–[69] are compared to the ones obtained in this project, the effects of the presence or absence of the solvent are contradictory, since the solvent they used are either as polar as acetonitrile (DMSO) or highly polarized solvents as HFIP. Hence, it is safe to say that monomeric GFD3E peptide is largely present in the liquid sample what will explain the orange spectra in fig. 3.19 and that, once the samples has been precipitated, the presence of these free GFD3E molecules is reduced to such a point that no longer have a strong effect and the fibers can be analyzed. The presence of these two peaks located at 336 nm and 357 nm may indicate the presence of both aggregation styles (parallel and antiparallel) being the antiparallel the most common since it is represented by the peak of higher intensity.

4.2 Silver functionalization of GFD3E fibers

The interaction between GFD3E and silver cations was studied by quantum chemical simulations and quantum chemical calculations. A posterior attempt to functionalize the GFD3E fibers with silver nanoparticles was done. The principal idea was to attract by electrostatic interaction silver cations for a later reduction of the silver ions to form a thin filament of silver metal on top of the fibers. That strategy had been done somewhere else with a complete different peptide [8] and with a different purpose. For the objective of the project to be accomplished, the fibers had to have a rather high coverage in order to have continuous silver filaments. To ensure a good coverage the first contact between the peptide and the silver cation is key, if the silver cation is able to be trapped at the surface of the peptide, the reduction step will be easier. QM simulations and quantum chemical calculations were performed in order to study that interaction.

The silver cation showed an attractive interaction towards the deprotonated carboxylic acid in all simulated and calculated geometries due to the attraction between the positive charge from the silver cation and the negative charge from the deprotonated carboxylic acid. An approximated distance can be guessed taking into consideration the ionic radii of both the silver ion and the oxygen ion. This guessed distance is of 2.1 Å, so the expected location of the silver cation was to be around these 2.1 Å. Although all results fell in the expected location, for those simulation performed in either solvent the silver cation was attracted towards only one of the two oxygen atoms and was placed in a closer location [fig. 3.13]. In a vacuum system, both components rely only on the interaction between the two charges, on the other hand the introduction of polarizable solvent can amplify such interaction by inducing small dipoles of the solvent molecules around the silver cation and the deprotonated carboxylic acid that may contribute to increasing this attractive force.

The geometry optimization led to a structure where the silver cation was placed in a equidistant point between the two oxygen atoms. This location is in agreement with

the idea of that the negative charge is in resonance between the two oxygen atoms. That can be seen in the output file [Files link] under the Mayer Population analysis. A general increase of the energy of the orbitals is expected but those orbitals corresponding to the silver off-axis d orbitals are expected to break the degeneracy of the d orbitals, since are expected to be responsible of the interaction between the silver cation and the deprotonated carboxylic acid [fig. 3.9]. Indeed, all orbitals increased in energy after the geometry optimization step but those that break the degeneracy are not the off-axis d orbitals, but the molecular orbitals corresponding to the in-axis x^2-y^2 and the off-axis yz orbitals. The loss of degeneracy of the silver d orbitals can be explained by visualizing the isosurface of these two molecular orbitals. It can be seen that while most of the probability to find the electron is placed on the silver atom, some small probability is found on both oxygen atoms. For the orbitals that show the larger increase of energy (orbitals yz and x^2y^2) the interaction is done between orbitals of opposite symmetry. Molecular Orbital Theory (part of the Ligand Field Theory) states that when two orbitals of opposite symmetry interact, a new highly energetic orbital is created, often harming the stability of the complex (anti-bonding MO). This may explain why the x^2y^2 orbital showed a much larger increase in energy than those off-axis as was expected. The same scenario is found for the results obtained from the QM simulation in vacuum. The silver cation is placed at a very similar location and while the energies are different, the energetic order of the orbitals is the same. In fig. 3.14 can be seen that the orbitals where there is some overlapping are essentially the same in a) and in b) (geometry optimization and QM simulation in vacuum respectively) as the energy diagram in fig. 3.9 show the same lost of degeneracy.

In the QM simulations where solvent was used, a difference in the final location of the silver cation can be appreciated. Both systems placed the silver cation closer to one of the oxygen atoms leading to a more linear interaction. Of the five d orbitals from the silver cation, only two of them have the correct orientation to have any kind of interaction with the molecular orbitals of the deprotonated acid, these are the xy and the x^2-y^2 d orbitals. These two orbitals are in either scenario the ones with higher energy. Constructive interaction in the case of the use of water as solvent is done by the orbital x^2-y^2 which is regarded as the orbital with less energy of them both [fig. 3.9] (although the difference is minimum) while the orbital xy is regarded as the more energetic. For the scenario with 30% acetonitrile completely different scenario is seen, orbital xy is the responsible for the constructive interaction while the x^2-y^2 is the only one breaking the degeneracy. This can be explain again if the symmetry of the orbitals is taken into consideration, since for both cases, the xy and the x^2-y^2 orbitals respectively will interact with opposed-symmetry orbitals from the deprotonated carboxylic acid, leading to the formation of a high energy MO.

Disagreeing with the visualization of the isosurface of the molecular orbitals of the different complexes, no orbital overlap was found in any of the successive analysis. In fig. 3.11, no constructive interaction between the different atomic orbitals can be seen in either of the molecular orbitals of the complex formed by neither the geometry optimization nor the QM simulations, due to the large energy gap between the valance orbitals of silver cation and the ones from the deprotonated carboxylic acid [fig. 3.12 and ??]. This large energy gap and the anti-symmetric orientation of the orbitals makes this interaction non-covalent. The lack of constructive overlap can be seen in the lack of electron density in the BCPs, although the results from the QAIM do not completely discard the presence of a weak electron density along the interaction axis.

This can be understood as the attraction the lone pair of electrons from the oxygen atom feel towards the silver cation.

The values obtained in the QAIM analysis are on the same trend (small differences can be seen due to the use of a different functional or from the size of the system) of those obtained in [14], indicating that the simulations and the later analysis of those is correct. In [14], the interaction between the aspartic and glutamic amino acids is classified as partially covalent, although they again see no overlap of atomic orbitals when the silver is interacting with the deprotonated carboxylic acid from the amino acid side-chain.

Putting altogether the different analysis performed in all four systems, it is difficult to attribute a partial covalent interaction since for such interaction to occur, a small overlap between atomic orbitals must occur, and given the CDA (charge decomposition) and DOS (Density of states) analysis, no constructive overlapping exist. It is true that in a coordination complex it is often found that the ligand cedes a pair of electrons to fill the empty orbitals of the metal. In this case a more complex interpretation of the CDA must be done, since the tendency of either giving or accepting electrons can be evaluated.

4.2.1 Silver functionalization of GFD3E fibers

After the description of the interaction found between the silver cation and the deprotonated carboxylic acid, functionalization of the GFD3E fibers was attempted. Functionalization of peptide fibers has been achieved before [89], [90]. In this project similar strategies were tried in order to cover the GFD3E fibers with silver nanoparticles. GFD3E fibers had to be formed before introduction of silver nitrate, since no fibers were found when the silver nitrate solution was used as diluting solvent of the GFD3E peptide (Attempt 4 and 5). The expected behaviour was for the silver cation to interact with the carboxylic acid, screening the negatives charges and hence, helping in the fiber formation, but the silver nitrate solution contained only water as solvent, reducing the amphiphilicity of the solvent what may have become a problem for the correct self-assembly of the fibers. This lack of fibers may indicate that the peptides are being trapped at the nanoparticle surface (since it is positively charge) and work as a capping agent, although further assessment must be done [??]. When the fibers were first formed and then attempted to be coated almost no coverage was seen and most of the fibers were visualized to be uncovered or covered just at the edges. A possible explanation is that the fibers do interact with the silver cation or the silver nanoparticle but upon addition of the reducing agent they are reduced one on top of another. This will explain the large and big aggregates of GFD3E fibers and of silver nanoparticles that can be seen in some SEM images. Another possibility is that the silver nanoparticles that are being reduced on top of the fibers acquire such a large size that tears apart the GFD3E fiber and this small fragments of peptide and silver nanoparticle aggregate. A weaker reducing agent (ascorbic acid) than sodium borohydrate was used to see if this aggregation could be eliminated, but no big differences were observed. Weak reducing agents lead to the formation of smaller particle size, what may lead to the synthesis of smaller particles suitable to interact with the peptide fiber. The introduction of a weaker reducing agent also led to a slower growth process and so, more time may have been given for the fibers to aggregate. Another factor of using ascorbic acid is that the growth of the nanoparticle is done over a seed

(preexisting nanoparticle). This was thought to be an advantage, since only nanoparticles on the fibers were expected to grow. On the contrary, results indicate that nanoparticles may have been growing by bringing GFD3E fibers together, what will explain this clusters of nanoparticles seen in the SEM images [fig. 3.25. The phenomena just explained should not be misunderstood by the aggregation of nanoparticles in a specific location when small bubbles are dried on the wafers. This will lead to a collapse of either fibers and/or silver nanoparticles in a given location corresponding to the edges of the evaporated bubbles. This can be seen in figs. 3.25 and 3.26 and is easily distinguished by their tendency to have a circular shape (following the shape of the bubbles).

The lack of coated GFD3E fibers can also be explained for a small concentration of silver nitrate. To ensure a good coverage, a large concentration of silver nitrate is required to ensure that the silver cation interact with the aspartic and glutamic acid. Different concentration were tried, increasing up to ten times the concentration of the peptide. Little difference was observed.

Another possibility for this lack of surface-coated fibers is that the silver cations may have a tendency to move insight the fiber and interact with the aromatic rings of the phenylalanine, being reduced inside the fibers and organizing in filaments in the hydrophobic core. Although this phenomenon was not expected, Reches and coworkers [91] achieved such filaments, although by using a complete different methodology (the biphenylalanine fibers were added into a boiling silver nitrate solution and reduced with citric acid). In order to test this hypothesis a simple peptide degradation by a simple proteolytic lysis can be done with a later visualization analysis.

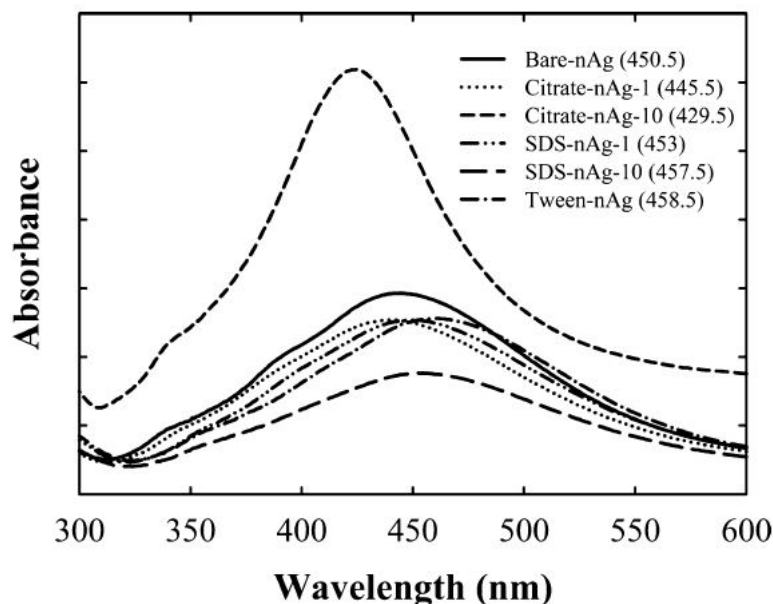


Figure 4.1: Effect of the introduction of a capping agent on the particle size.

Figure reproduced from [92] with permission from ACS Publications.

Functionalization of GFD3E fibers was studied, first by performing quantum chemical calculations on the interaction between the silver cations and the deprotonated carboxylic acid, expected anchoring point of the fibers, and a experimental attempt where silver nitrate concentrations and reducing agent components were changed in

order to find which protocol led to the higher functionalization rate. The results obtained from the calculation indicate a mainly electrostatic interaction between these two centers, although further calculations are required to see whether the presence of the full amino acid structure affects the interaction (and the anchoring point) [93], [94]. Further analysis as the CDA or LOL can also be performed in order to shine more light into the nature of the silver cation - GFD3E peptide interaction. Regarding the experimental approach, the protocol still must be tailored for GFD3E fibers, but a good starting point may be the introduction of capping agents to prevent the fibers to reduce one on top of the other and to control the nanoparticles size fig. 4.1.

CONCLUSION

The capability of F-moc GFD3E peptide (Glycine-Phenylalanine-Aspartic acid-Phenylalanine-Aspartic acid-Phenylalanine-Glutamic acid) to self-assemble into ordered amyloid fibers was tested together with the possible functionalization of the fibers due to the negative outer shell brought by the deprotonation of the aspartic and glutamic acids.

Molecular dynamics simulations of the coarse-grain model of the GFD3E peptide confirm a self-assembling propensity in a water and in ethanol, although difference in the morphology of such aggregates were found. When water was used as solvent a rapid and notable reduction of the solvent accessible surface area as well as of the interaction between the aromatic moieties and the solvent molecules was seen. Nonetheless, all results indicate that, despite GFD3E aggregating in these two different solvents and at different concentrations, no ordered fibers were seen, denoting that simulations have to be yet optimized to favour the formation of such fibers. This optimization comes from letting the system simulate for longer time, use a mixed solvent of water and ethanol and performing not only coarse-grain simulations but also atomistic simulations to mimic in a better extend what would happen in reality. Optimization of the simulations must be done since experimentally GFD3E peptide was found to not only aggregate but to do it in stable amyloid fibers in a ribbon-like manner. Different concentrations were tested and 0.75 mM led to the better results agreeing with CD spectroscopy and AFM visualization. GFD3E peptide was synthesized and analyzed by HPLC, where two very similar compounds were found of more or less same concentration in the sample after the synthesis. These two compounds most likely only differ from one amino acid due to its proximity, but a characterization of either is advised in order to confirm this hypothesis. The presence of two different compounds seemed to not affect the self-assembly of the GFD3E. The fibers observed varied in length in the range of micrometers and had a height profile of 15 nm. It was seen that when the concentration was augmented to 1 mM fibers were not only shorter but smaller, indicating a possible tighter packing. Thanks to the presence of the F-moc group, the arrangement of these amyloid fibers was found to be mainly antiparallel with some parallel interactions. Of course this must be further assessed since there are some discrepancies with the literature, although these can be due to solvent interactions. Functionalization of the GFD3E fibers was studied as well by two different strategies. First, the interaction between the silver cation and the carboxylic group of the aspartic and glutamic acid was studied by quantum chemical simulations and physico-chemical calculations. These calculations led to confirm that the most likely interaction between these two centers is electrostatic. Small values of electron density were calculated to be placed along the interaction axis between the silver cation and the deprotonated carboxylic acid. Further analysis may bring some more information on how this interaction is done, for example whether the existence of dative bonds can be shown or whether the interaction with not only a silver cation but the interaction with a silver nanoparticle would be of different nature.

Functionalization with silver nanoparticles was also studied experimentally. Different

protocols in terms of silver concentration, hierarchy of processes and reducing agents were tested. None of the attempts led to completely satisfying results, although some fibers were seen to be covered by silver nanoparticles, specially for the samples prepared with high concentration of salt (11.25 mM of silver nitrate) and reduced with 0.5 mM of sodium borohydrate. The results showed that the strategy that seems to work better is to first form the amyloid fibers and let them stabilize for at least one hour at room temperature, then slowly introduce the silver nitrate at a concentration higher than three times the GFD3E concentration and reduce with sodium borohydrate at low concentration adding it dropwise until a change in color can be seen. Further analysis to tailor the protocol to functionalize GFD3E fibers is required since no visualization of single complete covered fibers was achieved. The incorporation of coating agents may improve the yield of functionalization preventing the formation of silver aggregates and preventing the fibers to clump one on top of another.

The search and characterization of new short peptides that can assemble into ordered structures has increased in the recent years due to its large possibilities in microelectronics and in antibacterial treatment. GFD3E peptide seem to be a good contender for such applications since the incorporation of the phenylalanine rings can be used to form a delocalized electron cloud that may allow the fiber to be conductive through its longitudinal axes and the negative charges brought by the deprotonation of the aspartic and glutamic acid may allow for a tailored functionalization of the fiber based on its usage. Yet, characterization of the GFD3E fibers must continue in order to understand its promising applicability as an antimicrobial therapeutic or in the field of nanoelectronics. This project is intended to be a first step towards the discovery of the GFD3E potential and a small contribution to expand the knowledge on peptide self-assembly and peptide functionalization.

BIBLIOGRAPHY

- [1] A. H. Flood, J. F. Stoddart, D. W. Steuerman, and J. R. Heath, “Whence molecular electronics?” eng, *Science (American Association for the Advancement of Science)*, vol. 306, no. 5704, pp. 2055–2056, 2004, ISSN: 0036-8075.
- [2] J. M. Tour, “Molecular electronics. synthesis and testing of components,” eng, *Accounts of chemical research*, vol. 33, no. 11, pp. 791–804, 2000, ISSN: 0001-4842.
- [3] A. Coskun, J. M. Spruell, G. Barin, W. R. Dichtel, A. H. Flood, Y. Y. Botros, and J. F. Stoddart, “High hopes: Can molecular electronics realise its potential?” eng, *Chemical Society reviews*, vol. 41, no. 14, pp. 4827–4859, 2012, ISSN: 0306-0012.
- [4] C. Pigliacelli, R. Sánchez-Fernández, M. D. García, C. Peinador, and E. Pazos, “Self-assembled peptide-inorganic nanoparticle superstructures: From component design to applications,” eng, *Chemical communications (Cambridge, England)*, vol. 56, no. 58, pp. 8–814, 2020, ISSN: 1359-7345.
- [5] T. Scheibel, R. Parthasarathy, G. Sawicki, X.-M. Lin, H. Jaeger, and S. L. Lindquist, “Conducting nanowires built by controlled self-assembly of amyloid fibers and selective metal deposition,” eng, *Proceedings of the National Academy of Sciences - PNAS*, vol. 100, no. 8, pp. 4527–4532, 2003, ISSN: 1091-6490.
- [6] D. Gottlieb, S. A. Morin, S. Jin, and R. T. Raines, “Self-assembled collagen-like peptide fibers as templates for metallic nanowires,” eng, *Journal of materials chemistry*, vol. 18, no. 32, pp. 3865–3865, 2008, ISSN: 1364-5501.
- [7] T. Guterman, N. L. Ing, S. Fleischer, P. Rehak, V. Basavalingappa, Y. Hunash al, R. Dongre, S. Raghobhama, P. Král, T. Dvir, A. I. Hochbaum, and E. Gazit, “Electrical conductivity, selective adhesion, and biocompatibility in bacteria-inspired peptide-metal self-supporting nanocomposites,” eng, *Advanced materials (Weinheim)*, vol. 31, no. 10, 1 807 285–n/a, 2019, ISSN: 0935-9648.
- [8] Y. Wang, L. Cao, S. Guan, G. Shi, Q. Luo, L. Miao, I. Thistlethwaite, Z. Huang, J. Xu, and J. Liu, “Silver mineralization on self-assembled peptide nanofibers for long term antimicrobial effect,” eng, *Journal of materials chemistry*, vol. 22, no. 6, pp. 2575–2581, 2012, ISSN: 1364-5501.
- [9] H. Acar, R. Genc, M. Urel, T. S. Erkal, A. Dana, and M. O. Guler, “Self-assembled peptide nanofiber templated one-dimensional gold nanostructures exhibiting resistive switching,” eng, *Langmuir*, vol. 28, no. 47, pp. 16 347–16 354, 2012, ISSN: 0743-7463.
- [10] E. Pazos, E. Sleep, C. M. Rubert Perez, S. S. Lee, F. Tantakitti, and S. I. Stupp, “Nucleation and growth of ordered arrays of silver nanoparticles on peptide nanofibers: Hybrid nanostructures with antimicrobial properties,” eng, *Journal of the American Chemical Society*, vol. 138, no. 17, pp. 5507–5510, 2016, ISSN: 0002-7863.

- [11] Y. Hu, W. Xu, G. Li, L. Xu, A. Song, and J. Hao, "Self-assembled peptide nanofibers encapsulated with superfine silver nanoparticles via ag^+ coordination," eng, *Langmuir*, vol. 31, no. 31, pp. 8599–8605, 1900, ISSN: 0743-7463.
- [12] J. Wang, X. Zhao, J. Li, X. Kuang, Y. Fan, G. Wei, and Z. Su, "Electrostatic assembly of peptide nanofiber–biomimetic silver nanowires onto graphene for electrochemical sensors," eng, *ACS macro letters*, vol. 3, no. 6, pp. 529–533, 2014, ISSN: 2161-1653.
- [13] R. Srivastava, "Interaction of cysteine with au_n ($n=8, 10, 12$) even neutral clusters: A theoretical study," eng, *ChemistrySelect (Weinheim)*, vol. 2, no. 9, pp. 2789–2796, 2017, ISSN: 2365-6549.
- [14] A. A. Buglak, R. R. Ramazanov, and A. I. Kononov, "Silver cluster–amino acid interactions: A quantum-chemical study," eng, *Amino acids*, vol. 51, no. 5, pp. 855–864, 2019, ISSN: 1438-2199.
- [15] H. J. Xie, H. J. Xie, Q. F. Lei, Q. F. Lei, W. J. Fang, and W. J. Fang, "Intermolecular interactions between gold clusters and selected amino acids cysteine and glycine: A dft study," eng, *Journal of molecular modeling*, vol. 18, no. 2, pp. 645–652, 2012, ISSN: 1610-2940.
- [16] J. A. Palesko, eng, 1st ed. Broken Sound Parkway NW, Suite: chapman and Hall/CRC, 2007, ISBN: 1584886870.
- [17] *Physics and chemistry of interfaces*, eng, 3., rev. and enl. ed. Weinheim: Wiley-VCH Verlag, 2013, ISBN: 9783527412167.
- [18] J. J. McManus, P. Charbonneau, E. Zaccarelli, and N. Asherie, "The physics of protein self-assembly," eng, *Current opinion in colloid and interface science*, vol. 22, pp. 73–79, 2016, ISSN: 1359-0294.
- [19] G. A. Mihai, "Control, design, and understanding of molecular self-assembly," eng, in *Fabrication and Self-Assembly of Nanobiomaterials - Applications of Nanobiomaterials*, Elsevier, 2016, pp. 1–1, ISBN: 9780323415330.
- [20] M. Chintamaneni and M. Bhaskar, "Biomarkers in alzheimer's disease: A review," eng, *ISRN pharmacology*, vol. 2012, pp. 984 786–6, 2012, ISSN: 2090-5173.
- [21] E. Gazit, "Mechanisms of amyloid fibril self-assembly and inhibition. model short peptides as a key research tool," eng, *The FEBS journal*, vol. 272, no. 23, pp. 5971–5978, 2005, ISSN: 1742-464X.
- [22] F. Chiti and C. M. Dobson, "Protein misfolding, functional amyloid, and human disease," eng, *Annual review of biochemistry*, vol. 75, no. 1, pp. 333–366, 2006, ISSN: 0066-4154.
- [23] C. H. Norn and I. André, "Computational design of protein self-assembly," eng, *Current opinion in structural biology*, vol. 39, pp. 39–45, 2016, ISSN: 0959-440X.
- [24] K. C. Chou, M. Pottle, G. Némethy, H. A. Scheraga, *et al.*, "Structure of β -sheets: Origin of the right-handed twist and of the increased stability of antiparallel over parallel sheets," *Journal of Molecular Biology*, vol. 162, no. 1, pp. 89–112, 1982.
- [25] *Biological and Bio-inspired Nanomaterials Properties and Assembly Mechanisms*, eng, 1st ed. 2019., ser. Advances in Experimental Medicine and Biology, 1174. Singapore: Springer Singapore, 2019, ISBN: 981-13-9791-0.

- [26] C. J. Bowerman and B. L. Nilsson, "Review self-assembly of amphipathic β -sheet peptides: Insights and applications," eng, *Peptide Science*, vol. 98, no. 3, pp. 169–184, 2012, ISSN: 0006-3525.
- [27] K. Morris and L. Serpell, "From natural to designer self-assembling biopolymers, the structural characterisation of fibrous proteins and peptides using fibre diffractionpart of the peptide- and protein-based materials themed issue," eng, vol. 39, no. 9, pp. 3445–3453, 2010, ISSN: 0306-0012.
- [28] C. Wurth, N. K. Guimard, and M. H. Hecht, "Mutations that reduce aggregation of the alzheimer's $\alpha\beta$ 42 peptide: An unbiased search for the sequence determinants of $\alpha\beta$ amyloidogenesis," eng, *Journal of molecular biology*, vol. 319, no. 5, pp. 1279–1290, 2002, ISSN: 0022-2836.
- [29] S. Toksoz, H. Acar, and M. O. Guler, "Self-assembled one-dimensional soft nanostructures," eng, *Soft matter*, vol. 6, no. 23, pp. 5839–5849, 2010, ISSN: 1744-683X.
- [30] J. Wang, K. Liu, R. Xing, and X. Yan, "Peptide self-assembly: Thermodynamics and kinetics," eng, *Chemical Society reviews*, vol. 45, no. 2, pp. 5589–564, 2016, ISSN: 0306-0012.
- [31] I. M. Stanković, S. Niu, M. B. Hall, and S. D. Zarić, "Role of aromatic amino acids in amyloid self-assembly," eng, *International journal of biological macromolecules*, vol. 156, pp. 949–959, 2020, ISSN: 0141-8130.
- [32] C. J. Bowerman, D. M. Ryan, D. A. Nissan, and B. L. Nilsson, "The effect of increasing hydrophobicity on the self-assembly of amphipathic beta-sheet peptides," eng, *Molecular bioSystems*, vol. 5, no. 9, pp. 1058–1069, 2009, ISSN: 1742-206X.
- [33] C. J. Bowerman, W. Liyanage, A. J. Federation, and B. L. Nilsson, "Tuning β -sheet peptide self-assembly and hydrogelation behavior by modification of sequence hydrophobicity and aromaticity," eng, *Biomacromolecules*, vol. 12, no. 7, pp. 2735–2745, 2011, ISSN: 1525-7797.
- [34] A. Lakshmanan, D. W. Cheong, A. Accardo, E. D. Fabrizio, C. Riekkel, and C. A. E. Hauser, "Aliphatic peptides show similar self-assembly to amyloid core sequences, challenging the importance of aromatic interactions in amyloidosis," eng, *Proceedings of the National Academy of Sciences - PNAS*, vol. 110, no. 2, pp. 519–524, 2013, ISSN: 0027-8424.
- [35] N. R. Lee, C. J. Bowerman, and B. L. Nilsson, "Effects of varied sequence pattern on the self-assembly of amphipathic peptides," eng, *Biomacromolecules*, vol. 14, no. 9, pp. 3267–3277, 2013, ISSN: 1525-7797.
- [36] Y. Zhao, W. Yang, C. Chen, J. Wang, L. Zhang, and H. Xu, "Rational design and self-assembly of short amphiphilic peptides and applications," eng, *Current opinion in colloid and interface science*, vol. 35, pp. 112–123, 2018, ISSN: 1359-0294.
- [37] J. K. Sahoo, C. Nazareth, M. A. VandenBerg, and M. J. Webber, "Self-assembly of amphiphilic tripeptides with sequence-dependent nanostructure," eng, *Biomaterials science*, vol. 5, no. 8, pp. 1526–1530, 2017, ISSN: 2047-4830.
- [38] Y. Jean, *Molecular orbitals of transition metal complexes*, eng. Oxford ; Oxford University Press, 2005, ISBN: 1-280-84624-0.
- [39] D. A. McQuarrie, eng, 2nd ed. University of California, Davis: University Science Books, 2008, ISBN: 978-1-891389-50-4.

- [40] F. Bickelhaupt, "A chemist's guide to density functional theory," eng, *Chemical physics*, vol. 2, pp. 257–258, 2001, ISSN: 0301-0104.
- [41] A. L. Parrill and K. B. Lipkowitz, *Reviews in computational chemistry, volume 30*, eng, 1st ed., ser. Reviews in Computational Chemistry. Somerset: Wiley-Interscience, 2017, ISBN: 9781119355434.
- [42] D. Frenkel, *Understanding molecular simulation : from algorithms to applications*, eng, 2. ed., ser. Computational science ; vol. 1. San Diego, Calif: Academic, 2002, ISBN: 0122673514.
- [43] D. C. Rapaport, *The art of molecular dynamics simulation*, eng, 2nd ed. Cambridge, UK ; Cambridge University Press, 2004, ISBN: 1-107-14671-2.
- [44] S. Y. Joshi and S. A. Deshmukh, "A review of advancements in coarse-grained molecular dynamics simulations," eng, *Molecular simulation*, vol. ahead-of-print, no. ahead-of-print, pp. 1–18, ISSN: 0892-7022.
- [45] A. Kukol, Ed., *Molecular Modeling of Proteins*, eng, 2nd ed. 2015., ser. Methods in Molecular Biology, 1215. New York, NY: Springer New York, 2015, ISBN: 1-4939-1465-0.
- [46] D. H. de Jong, G. Singh, W. F. D. Bennett, C. Arnarez, T. A. Wassenaar, L. V. Schafer, X. Periole, D. P. Tieleman, and S. J. Marrink, "Improved parameters for the martini coarse-grained protein force field," eng, *Journal of chemical theory and computation*, vol. 9, no. 1, pp. 687–697, 2013, ISSN: 1549-9618.
- [47] W. Humphrey, A. Dalke, and K. Schulten, "Vmd: Visual molecular dynamics," eng, *Journal of molecular graphics*, vol. 14, no. 1, pp. 33–38, 1996, ISSN: 0263-7855.
- [48] M. J. Abraham, T. Murtola, R. Schulz, S. Páll, J. C. Smith, B. Hess, and E. Lindahl, "Gromacs: High performance molecular simulations through multi-level parallelism from laptops to supercomputers," eng, *SoftwareX*, vol. 1-2, no. C, pp. 19–25, 2015, ISSN: 2352-7110.
- [49] S. Páll, M. J. Abraham, C. Kutzner, B. Hess, and E. Lindahl, "Tackling exascale software challenges in molecular dynamics simulations with gromacs," eng, in *Solving Software Challenges for Exascale*, ser. Lecture Notes in Computer Science, Cham: Springer International Publishing, 2015, pp. 3–27, ISBN: 9783319159751.
- [50] B. Hess, "P-lincs: A parallel linear constraint solver for molecular simulation," eng, *Journal of chemical theory and computation*, vol. 4, no. 1, pp. 116–122, 2008, ISSN: 1549-9618.
- [51] G. Bussi, D. Donadio, and M. Parrinello, "Canonical sampling through velocity rescaling," eng, *The Journal of chemical physics*, vol. 126, no. 1, pp. 014 101–014101–7, 2007, ISSN: 0021-9606.
- [52] S. Pronk, S. Páll, R. Schulz, P. Larsson, P. Bjelkmar, R. Apostolov, M. R. Shirts, J. C. Smith, P. M. Kasson, D. van der Spoel, B. Hess, and E. Lindahl, "Gromacs 4.5: A high-throughput and highly parallel open source molecular simulation toolkit," eng, *Bioinformatics (Oxford, England)*, vol. 29, no. 7, pp. 845–854, 2013, ISSN: 1367-4803.
- [53] B. Hess, C. Kutzner, D. van der Spoel, and E. Lindahl, "Gromacs 4: Algorithms for highly efficient, load-balanced, and scalable molecular simulation," eng, *Journal of chemical theory and computation*, vol. 4, no. 3, pp. 435–447, 2008, ISSN: 1549-9618.

- [54] D. Van Der Spoel, E. Lindahl, B. Hess, G. Groenhof, A. E. Mark, and H. J. C. Berendsen, "Gromacs: Fast, flexible, and free," eng, *Journal of computational chemistry*, vol. 26, no. 16, pp. 1701–1718, 2005, ISSN: 0192-8651.
- [55] E. Lindahl, B. Hess, and D. van der Spoel, "Gromacs 3.0: A package for molecular simulation and trajectory analysis," eng, *Journal of Molecular Modeling*, vol. 7, no. 8, pp. 306–317, 2001, ISSN: 0949-183X.
- [56] S. J. Marrink, H. J. Risselada, S. Yefimov, D. P. Tieleman, and A. H. de Vries, "The martini force field: Coarse grained model for biomolecular simulations," eng, *The journal of physical chemistry. B*, vol. 111, no. 27, pp. 7812–7824, 2007, ISSN: 1520-6106.
- [57] M. D. Hanwell, D. E. Curtis, D. C. Lonie, T. Vandermeersch, E. Zurek, and G. R. Hutchison, "Avogadro: An advanced semantic chemical editor, visualization, and analysis platform," eng, *Journal of cheminformatics*, vol. 4, no. 1, pp. 17–17, 2012, ISSN: 1758-2946.
- [58] S. N. Helambe, M. P. Lokhande, A. C. Kumbharkhane, S. C. Mehrotra, and S Doraiswamy, "Dielectric study of aqueous solution of acetonitrile," eng, *Pramana*, vol. 44, no. 5, pp. 405–410, 1995, ISSN: 0304-4289.
- [59] T. Lu and F. Chen, "Multiwfn: A multifunctional wavefunction analyzer," eng, *Journal of computational chemistry*, vol. 33, no. 5, pp. 580–592, 2012, ISSN: 0192-8651.
- [60] L. Mulfinger, S. D. Solomon, M. Bahadory, A. V. Jeyarajasingam, S. A. Rutkowsky, and C. Boritz, "Synthesis and study of silver nanoparticles," eng, *Journal of chemical education*, vol. 84, no. 2, pp. 322–, 2007, ISSN: 0021-9584.
- [61] P. S. V. Kumar, V Raghavendra, and V Subramanian, "Bader's theory of atoms in molecules (aim) and its applications to chemical bonding," eng, *Journal of chemical sciences (Bangalore, India)*, vol. 128, no. 10, pp. 1527–1536, 2016, ISSN: 0973-7103.
- [62] Z. Liu, T. Lu, and Q. Chen, "An sp-hybridized all-carboatomic ring, cyclo[18]carbon: Electronic structure, electronic spectrum, and optical nonlinearity," eng, *Carbon (New York)*, vol. 165, pp. 461–467, 2020, ISSN: 0008-6223.
- [63] *Circular dichroism and the conformational analysis of biomolecules*, eng. New York, N.Y: Plenum Press, 1996, ISBN: 0306451425.
- [64] D. M. Fowler, A. V. Koulov, C. Alory Jost, M. S. Marks, W. E. Balch, and J. W. Kelly, "Functional amyloid formation within mammalian tissue," eng, *PLoS biology*, vol. 4, no. 1, pp. 0100–0107, 2006, ISSN: 1545-7885.
- [65] N. Amdursky and M. M. Stevens, "Circular dichroism of amino acids: Following the structural formation of phenylalanine," eng, *Chemphyschem*, vol. 16, no. 13, pp. 2768–2774, 2015, ISSN: 1439-4235.
- [66] B. R. Sahoo, T. Genjo, M. Bekier, S. J. Cox, A. K. Stoddard, M. Ivanova, K. Yasuhara, C. A. Fierke, Y. Wang, and A. Ramamoorthy, "Alzheimer's amyloid-beta intermediates generated using polymer-nanodiscs," eng, *Chemical communications (Cambridge, England)*, vol. 54, no. 91, pp. 12 883–12 886, 2018, ISSN: 1359-7345.
- [67] C. Tang, R. V. Ulijn, and A. Saiani, "Effect of glycine substitution on fmoc–diphenylalanine self-assembly and gelation properties," eng, *Langmuir*, vol. 27, no. 23, pp. 14 438–14 449, 2011, ISSN: 0743-7463.

- [68] K. Tao, E. Yoskovitz, L. Adler Abramovich, and E. Gazit, "Optical property modulation of fmoc group by ph-dependent self-assembly," eng, *RSC advances*, vol. 5, no. 90, pp. 73 914–73 918, 2015, ISSN: 2046-2069.
- [69] S. Roy, N. Javid, P. W. J. M. Frederix, D. A. Lamprou, A. J. Urquhart, N. T. Hunt, P. J. Halling, and R. V. Ulijn, "Dramatic specific-ion effect in supramolecular hydrogels," eng, *Chemistry : a European journal*, vol. 18, no. 37, pp. 11 723–11 731, 2012, ISSN: 0947-6539.
- [70] D. W. P. M. Löwik, J. Garcia-Hartjes, J. T. Meijer, and J. C. M. van Hest, "Tuning secondary structure and self-assembly of amphiphilic peptides," eng, *Langmuir*, vol. 21, no. 2, pp. 524–526, 2005, ISSN: 0743-7463.
- [71] A. Dehsorkhi, V. Castelletto, and I. W. Hamley, "Self-assembling amphiphilic peptides: Self-assembling peptides," eng, *Journal of peptide science*, vol. 20, no. 7, pp. 453–467, 2014, ISSN: 1075-2617.
- [72] A. Reymer, K. K. Frederick, S. Rocha, T. Beke-Somfai, C. C. Kitts, S. Lindquist, and B. Nordén, "Orientation of aromatic residues in amyloid cores: Structural insights into prion fiber diversity," eng, *Proceedings of the National Academy of Sciences - PNAS*, vol. 111, no. 48, pp. 17 158–17 163, 2014, ISSN: 0027-8424.
- [73] E. Jack, M. Newsome, P. G. Stockley, S. E. Radford, and D. A. Middleton, "The organization of aromatic side groups in an amyloid fibril probed by solid-state 2h and 19f nmr spectroscopy," eng, *Journal of the American Chemical Society*, vol. 128, no. 25, pp. 8098–8099, 2006, ISSN: 0002-7863.
- [74] E. Gazit, "A possible role for π -stacking in the self-assembly of amyloid fibrils," eng, *The FASEB journal*, vol. 16, no. 1, pp. 77–83, 2002, ISSN: 0892-6638.
- [75] A. Smith, R. Williams, C Tang, P Coppo, R. Collins, M. Turner, A Saiani, and R. Ulijn, "Fmoc-diphenylalanine self assembles to a hydrogel via a novel architecture based on π - π interlocked β -sheets," eng, *Advanced materials (Weinheim)*, vol. 20, no. 1, pp. 37–41, 2008, ISSN: 0935-9648.
- [76] S. Takada, "Coarse-grained molecular simulations of large biomolecules," *Current opinion in structural biology*, vol. 22, no. 2, pp. 130–137, 2012.
- [77] A. T. Kuo, S. Urata, K. Nakabayashi, H. Watabe, and S. Honmura, "Coarse-grained molecular dynamics simulation of perfluorosulfonic acid polymer in water-ethanol mixtures," eng, *Macromolecules*, vol. 54, no. 2, pp. 609–620, 2021, ISSN: 0024-9297.
- [78] R. Behrendt, P. White, and J. Offer, "Advances in fmoc solid-phase peptide synthesis," *Journal of Peptide Science*, vol. 22, no. 1, pp. 4–27, 2016.
- [79] M. Stawikowski and G. B. Fields, "Introduction to peptide synthesis," *Current protocols in protein science*, vol. 69, no. 1, pp. 18–1, 2012.
- [80] D. Samson, D. Rentsch, M. Minuth, T. Meier, and G. Loidl, "The aspartimide problem persists: Fluorenylmethoxycarbonyl-solid-phase peptide synthesis (fmoc-spps) chain termination due to formation of n-terminal piperazine-2, 5-diones," *Journal of Peptide Science*, vol. 25, no. 7, p. 3193, 2019.
- [81] A. K. Tickler and J. D. Wade, "Overview of solid phase synthesis of "difficult peptide" sequences," *Current protocols in protein science*, vol. 50, no. 1, pp. 18–8, 2007.
- [82] L. M. Mikesch, B. Ueberheide, A. Chi, J. J. Coon, J. E. Syka, J. Shabanowitz, and D. F. Hunt, "The utility of etd mass spectrometry in proteomic analysis,"

- eng, *Biochimica et biophysica acta. Proteins and proteomics*, vol. 1764, no. 12, pp. 1811–1822, 2006, ISSN: 1570-9639.
- [83] A. Frank, S. Tanner, V. Bafna, and P. Pevzner, “Peptide sequence tags for fast database search in mass-spectrometry,” eng, *Journal of proteome research*, vol. 4, no. 4, pp. 1287–1295, 2005, ISSN: 1535-3893.
- [84] M. Migliore, A. Bonvicini, V. Tognetti, L. Guilhaudis, M. Baaden, H. Oulyadi, L. Joubert, and I. Ségalas Milazzo, “Characterization of β -turns by electronic circular dichroism spectroscopy: A coupled molecular dynamics and time-dependent density functional theory computational study,” *Physical Chemistry Chemical Physics*, vol. 22, no. 3, pp. 1611–1623, 2020.
- [85] D. Chandler, “Interfaces and the driving force of hydrophobic assembly,” eng, *Nature (London)*, vol. 437, no. 7059, pp. 640–647, 2005, ISSN: 0028-0836.
- [86] C. C. vandenAkker, M. F. Engel, K. P. Velikov, M. Bonn, and G. H. Koenderink, “Morphology and persistence length of amyloid fibrils are correlated to peptide molecular structure,” *Journal of the American Chemical Society*, vol. 133, no. 45, pp. 18 030–18 033, 2011.
- [87] J. Adamcik, C. Lara, I. Usov, J. S. Jeong, F. S. Ruggeri, G. Dietler, H. A. Lashuel, I. W. Hamley, and R. Mezzenga, “Measurement of intrinsic properties of amyloid fibrils by the peak force qnm method,” *Nanoscale*, vol. 4, no. 15, pp. 4426–4429, 2012.
- [88] J. R. Lakowicz, *Principles of Fluorescence Spectroscopy*, 3rd. Springer, 2006, ISBN: 0387312781,9780387312781.
- [89] W. C. Fu, M. A. Opazo, S. M. Acuña, and P. G. Toledo, “New route for self-assembly of α -lactalbumin nanotubes and their use as templates to grow silver nanotubes,” eng, *PloS one*, vol. 12, no. 4, e0175680–e0175680, 2017, ISSN: 1932-6203.
- [90] E. Gazit, “Use of biomolecular templates for the fabrication of metal nanowires,” eng, *The FEBS journal*, vol. 274, no. 2, pp. 317–322, 2007, ISSN: 1742-464X.
- [91] M. Reches and E. Gazit, “Casting metal nanowires within discrete self-assembled peptide nanotubes,” *Science*, vol. 300, no. 5619, pp. 625–627, 2003.
- [92] X. Li, J. J. Lenhart, and H. W. Walker, “Aggregation kinetics and dissolution of coated silver nanoparticles,” *Langmuir*, vol. 28, no. 2, pp. 1095–1104, 2012.
- [93] S. Eckhardt, P. S. Brunetto, J. Gagnon, M. Priebe, B. Giese, and K. M. Fromm, “Nanobio silver: Its interactions with peptides and bacteria, and its uses in medicine,” eng, *Chemical reviews*, vol. 113, no. 7, pp. 4708–4754, 2013, ISSN: 0009-2665.
- [94] S. A. A. Sajadi, “Metal ion-binding properties of l-glutamic acid and l-aspartic acid, a comparative investigation,” eng, *Natural science (Irvine, Calif.)*, vol. 2, no. 2, pp. 85–90, 2010, ISSN: 2150-4091.
- [95] *Storage and handling of photoresists and ancillaries*.
- [96] D. L. Flamm and O. Auciello, *Plasma deposition, treatment, and etching of polymers: the treatment and etching of polymers*. Elsevier, 2012.
- [97] J. R. Vig, “Uv/ozone cleaning of surfaces,” *Journal of Vacuum Science & Technology A: Vacuum, Surfaces, and Films*, vol. 3, no. 3, pp. 1027–1034, 1985.

APPENDIX

A.1 LCAO of a two electron system described by two basis functions

This section is based on [39].

Here an example of LCAO used in a system of a diatomic molecule with one electron (for example H^+ interaction). This simple interaction will allow for some simplifications and assumptions that will ease the lector to have an idea of how the LCAO method works.

The MO wave function is described as

$$\psi_K = c_1\phi_1 + c_2\phi_2 \quad (\text{A.1})$$

From the time-independent Schrödinger equation, to measure the energy of a system the following equation must be applied,

$$H\psi_K = E\psi_K \quad (\text{A.2})$$

which once it is integrated over all space leads to:

$$\left| H - E \right| \psi_K \rangle = 0 \quad (\text{A.3})$$

Introducing eq. (A.1) into eq. (A.3) the next expression is obtained:

$$\left| H - E \left| \sum^K C_1\phi_a + C_2\phi_b \right. \right| = 0 \quad (\text{A.4})$$

If now, eq. (A.4) is multiplied at the left by each of the basis function describing the atomic orbitals the next set of equations is obtained:

$$0 = \begin{pmatrix} c_1 \langle \phi_a | H - E | \phi_a \rangle & c_2 \langle \phi_a | H - E | \phi_b \rangle \\ c_1 \langle \phi_b | H - E | \phi_a \rangle & c_2 \langle \phi_b | H - E | \phi_b \rangle \end{pmatrix} \quad (\text{A.5})$$

Separating the terms in eq. (A.5), the following equation is obtained. This will be the one over which the eigenvalues will be calculated, each of which will be the solution of the Slater determinant and will represent a new molecular orbital.

Simplification	Value	Reason
$H_{aa}=H_{bb}$	ε	The energy for the electron to be placed in either atom is the same, since they are the same element
$H_{ab}=H_{ba}$	V_{ab}	Potential energy is the same for either interactions, since the hamiltonian is a hermitian operator
$S_{aa}=S_{bb}$	1	Atomic orbitals are normalized. The probability of finding an electron somewhere in the atomic orbital is 1
$S_{ab}=S_{ba}$	S_{ab}	Because the 1_s orbitals (the ones studied in this example) are real.

Table A.1: Assumptions made to simply the calculation of the matrix of eq. (A.7)

$$\begin{pmatrix} c_1 \\ c_2 \end{pmatrix} \begin{pmatrix} \langle \phi_a | H | \phi_a \rangle & \langle \phi_a | H | \phi_b \rangle \\ \langle \phi_b | H | \phi_a \rangle & \langle \phi_b | H | \phi_b \rangle \end{pmatrix} = E \begin{pmatrix} c_1 \\ c_2 \end{pmatrix} \begin{pmatrix} \langle \phi_a | \phi_a \rangle & \langle \phi_a | \phi_b \rangle \\ \langle \phi_b | \phi_a \rangle & \langle \phi_b | \phi_b \rangle \end{pmatrix} \quad (\text{A.6})$$

Since the interacting system being described is a homonuclear diatomic molecule with only one electron (H^+), the following assumptions [appendix A.1] can be done that will simplify system in eq. (A.7) to:

$$\begin{pmatrix} c_1 \\ c_2 \end{pmatrix} \begin{pmatrix} \varepsilon & V_{ab} \\ V_{ab} & \varepsilon \end{pmatrix} = E \begin{pmatrix} c_1 \\ c_2 \end{pmatrix} \begin{pmatrix} S_{aa} & S_{ab} \\ S_{ba} & S_{bb} \end{pmatrix} \quad (\text{A.7})$$

From eq. (A.7), the same determinant as in eq. (1.12):

$$0 = \begin{vmatrix} \varepsilon - E & V_{12} - ES_{ab} \\ V_{12} - ES_{ab} & \varepsilon - E \end{vmatrix}$$

Solving the secular determinant in appendix A.1, the next expression is obtained

$$(\varepsilon - E)^2 - (V_{12} - ES_{ab})^2 = 0 \quad (\text{A.8})$$

Two solutions are of interest to solve this problem:

$$E = \frac{\varepsilon + V_{12}}{1 + S_{12}} \quad (\text{A.9})$$

$$E = \frac{\varepsilon - V_{12}}{1 - S_{12}} \quad (\text{A.10})$$

The two solutions above represents the two molecular orbitals created upon interaction of each of the s orbitals from both hydrogen atoms, the bonding molecular orbital [eq. (A.9)] and the anti-bonding [eq. (A.10)]. Those are represented in fig. A.1

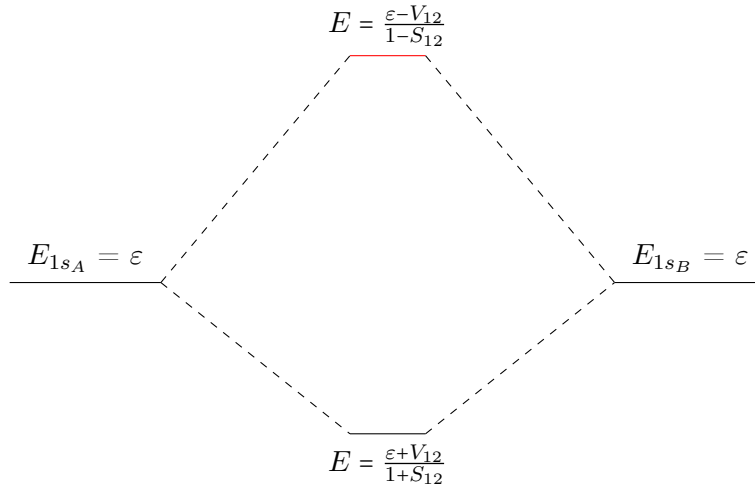


Figure A.1: Representation of both atomic orbitals from both hydrogen atoms interacting and the new molecular orbitals created upon interaction. In red, the anti-bonding orbital is represented. Their respective energy values are expressed. Although it is a representation, the anti-bonding orbital is more destabilizing than stabilizing the bonding orbital is.

A.2 Role of electron density in DFT

The electron density ($\rho(\mathbf{r})$) is the principal component in DFT approximation on solving the Schrodinger equation to calculate the wavefunctions of the molecular orbitals. It is defined as the probability of finding an electron with arbitrary spin within an arbitrary space while the rest of the electrons have arbitrary position and spin.

$$\rho(\mathbf{r}) = N \int \int \left[\psi(\mathbf{x}_1, \mathbf{x}_2, \mathbf{x}_3, \dots, \mathbf{x}_N) \right]^2 d_{s_1} d_{\mathbf{x}_N} \quad (\text{A.11})$$

where N represents the number of electrons. Likewise, the same concept can be applied when studying the probability of finding two electrons with spin σ_1 and σ_2 at two different points in space. This is called the pair density and is defined as

$$\rho_2(\mathbf{x}_1, \mathbf{x}_2) = N(N-1) \int \int \left[\psi(\mathbf{x}_1, \mathbf{x}_2, \mathbf{x}_3, \dots, \mathbf{x}_N) \right]^2 d_{\mathbf{x}_N} \quad (\text{A.12})$$

The pair density is key to DFT approximation since it has to introduce the effect of electron-electron interaction. This interaction can be reduced to the fact that electrons are fermions and so they have an antisymmetric wavefunction and that electrons are charged particles so there will be coulomb repulsion between them. In order to introduce the concept of symmetry in the electron wavefunction, first the pair density expression will be changed to the reduced density matrix, where the complex conjugate of the electron wavefunction is used.

$$\gamma_2(\mathbf{x}_1, \mathbf{x}_2, \mathbf{x}_1', \mathbf{x}_2') = N(N-1) \int \int \psi(\mathbf{x}_1, \mathbf{x}_2, \mathbf{x}_3, \dots, \mathbf{x}_N) \psi^*(\mathbf{x}_1', \mathbf{x}_2', \dots, \mathbf{x}_N) d_{\mathbf{x}_N} \quad (\text{A.13})$$

If in eq. (A.13) the variables are interchanged, say x_1 for x_2 or x_1' for x_2' , the value of γ_2 will change sign

$$\gamma_2(\mathbf{x}_1, \mathbf{x}_2, \mathbf{x}_1', \mathbf{x}_2') = -\gamma_2(\mathbf{x}_2, \mathbf{x}_1, \mathbf{x}_1', \mathbf{x}_2') \quad (\text{A.14})$$

Following this expression, when the probability to find two electrons with the same spin at the same spot ($x_1 = x_2$) is studied, the expression obtained will only be correct if $\gamma_2(\mathbf{x}_1, \mathbf{x}_2)$ is null. Hence, electrons with the same spin do not move independently from one another. This effect is known as Fermi or exchange correlation.

The second property that will affect how the pair density is computed is the charge of the electrons. Since they are negatively charged, the coulomb repulsion will prevent them from being close to one another. This effect is known as Coulomb correlation. These two effects are incorporated in the pair density expression as

$$\rho_2(\mathbf{x}_1, \mathbf{x}_2) = \rho(\mathbf{x}_1)\rho(\mathbf{x}_2)[1 + f(\mathbf{x}_1; \mathbf{x}_2)] \quad (\text{A.15})$$

where $f(\mathbf{x}_1; \mathbf{x}_2)$ is the correlation factor, that is zero when there is no correlation at all between electrons (self-interacting system).

Bearing this scheme in mind, a new concept will be introduced. This is the Conditional probability [eq. (A.16)]. $\Omega(\mathbf{x}_2, \mathbf{x}_1)$ describes the probability of finding an electron with a given spin at \mathbf{x}_2 when there is an already known electron at \mathbf{x}_1 .

$$\Omega(\mathbf{x}_2, \mathbf{x}_1) = \frac{\rho_2(\mathbf{x}_1, \mathbf{x}_2)}{\rho_1(\mathbf{x}_1)} \quad (\text{A.16})$$

The difference between the probability of finding an electron in \mathbf{x}_2 and the conditional probability is the exchange-correlation effect discussed above (Fermi and Coulomb correlation), h_{xc} , also known as exchange-correlation hole. This term will always be negative since it must lead to a reduction on the probability of finding an electron in \mathbf{x}_2 .

$$h_{xc}(\mathbf{x}_1; \mathbf{x}_2) = \rho_2(\mathbf{x}_2)f(\mathbf{x}_1; \mathbf{x}_2) \quad (\text{A.17})$$

Keeping these two concepts in mind, the energy of the electron-electron interaction can be described as

$$E_{e-e} = \frac{1}{2} \int \int \frac{\rho_2(\mathbf{x}_1, \mathbf{x}_2)}{x_{12}} d\mathbf{x}_1 d\mathbf{x}_2 \quad (\text{A.18})$$

eq. (A.18) when combined with eq. (A.15) and eq. (A.16) will lead to

$$E_{ee} = \frac{1}{2} \int \int \frac{\rho(\mathbf{x}_1)\rho(\mathbf{x}_2)}{x_{12}} d\mathbf{x}_1 d\mathbf{x}_2 + \frac{1}{2} \int \int \frac{\rho(\mathbf{x}_1)h_{xc}(\mathbf{x}_1; \mathbf{x}_2)}{x_{12}} d\mathbf{x}_1 d\mathbf{x}_2 \quad (\text{A.19})$$

where the term x_{12} refers to the distance between electrons. It is clear that the first term of eq. (A.19) is very similar to the Coulomb interaction between two charged particles and it is often represented as $J[\rho]$ [eq. (1.16)]. The second term will take into consideration the exchange-correlation effect together with the electron density.

A.3 Hartree-Fock: Slater determinant

When studying a many-body electric system as molecules are, the mathematical expressions describing the system increase its complexity to the point where they are almost impossible to compute. A very relevant example for this project is the hamiltonian operator (\hat{H}), that goes from a simple expression [eq. (A.20)] to a very complex one when the system is upgraded to two nuclei with one electron each [eq. (A.21)].

$$\hat{H} = -\frac{\hbar^2}{2m}\nabla^2 - \frac{e^2}{\epsilon_0 r} \quad (\text{A.20})$$

$$\hat{H} = -\sum_{i=1}^N \frac{\hbar^2}{2M_i} \nabla_{R_i}^2 + \frac{1}{2} \sum_{i=1}^N \sum_{j \neq 1}^N \frac{Z_i Z_j e^2}{|R_i - R_j|} - \frac{\hbar^2}{2m} \sum_{i=1}^n \nabla_{r_i}^2 - \sum_{i=1}^N \sum_{j \neq 1}^n \frac{Z_i e^2}{|R_i - r_j|} + \frac{1}{2} \sum_{i=1}^n \sum_{j \neq 1}^n \frac{e^2}{|r_i - r_j|} \quad (\text{A.21})$$

Such a complex hamiltonian of the many-body system displays one of the most complicated treats of big systems, and is that the hamiltonian now is a function of many dimensions (each electron and each nuclei is understood as a dimension on their own) [eq. (A.22)].

$$\hat{H}(R_1 \dots R_n, r_1 \dots r_n) \psi(R_1 \dots R_n, r_1 \dots r_n) = E \psi(R_1 \dots R_n, r_1 \dots r_n) \quad (\text{A.22})$$

A first approximation that simplifies the mathematical expression is the Born-Oppenheimer approximation, where motion of nuclei is neglected due to its much larger mass than the one of the electrons. Hence, all the terms describing the interaction between nuclei in eq. (A.21) are neglected [eq. (A.23)].

$$\hat{H} = -\frac{\hbar^2}{2m} \sum_{i=1}^n \nabla_{r_i}^2 - \sum_{i=1}^N \sum_{j \neq 1}^n \frac{Z_i e^2}{|R_i - r_j|} + \frac{1}{2} \sum_{i=1}^n \sum_{j \neq 1}^n \frac{e^2}{|r_i - r_j|} \quad (\text{A.23})$$

Even the the Born-Oppenheimer approximation, it is computationally prohibitive to check for all possible wave-functions to minimize the energy of the system, hence, more approximations are needed. One of these, is the Hartree-Fock approximation. This is based on the idea that a system wave-function can be described by the product of single electron wave-functions [eq. (A.24)].

$$\psi(r_1, r_2, \dots, r_n) = \phi(r_1) \phi(r_2) \dots \phi(r_n) \quad (\text{A.24})$$

This expression must fulfill the property of antisymmetry of the electron wave-function otherwise electrons will not be indistinguishable so they will not be understood as fermions ¹.

The expression in eq. (A.24) can be written as a determinant, which will be called Slater determinant [eq. (A.25)].

¹In quantum physics an operator that permute a given number of electrons exist \hat{P}_{ix} . This operator what it does it to change one electron for another. $\hat{P}_{1,2}^2 \psi(1, 2, \dots, n) = \pm \psi(1, 2, \dots, n)$. Only the negative solutions will apply for fermions.

$$\psi(r_1, \dots, r_N) = (N!)^{-\frac{1}{2}} \begin{vmatrix} \phi_1(r_1) & \dots & \phi_N(r_1) \\ \vdots & \ddots & \vdots \\ \phi_1(r_N) & \dots & \phi_N(r_N) \end{vmatrix} \quad (\text{A.25})$$

A.4 Adiabatic Connection and Hybrid functionals

Adiabatic connection lies on the basis on the strategy that hybrid functionals use in order to approximate the exchange-correlation energy (E_{xc}). This strategy consists on modifying the hamiltonian based on a parameter λ to go from the "non-interacting system" to a fully interacting system ².

$$\hat{H}_\lambda = \hat{T} + \hat{V}_{ext}^\lambda + \lambda \hat{V}_{eff} \quad (\text{A.26})$$

In the equation above, the parameter λ appears in two terms. The first one, \hat{V}_{ext}^λ is the external potential and it will be adjusted for every different value of λ used in order to match the electron density to the one is being calculated for the system. The second time λ appears it does so as a coupling strength parameter. The term it proceeds is describing the potential of the electron-electron interaction. So as described in section 1.3.1, when $\lambda=0$ the whole term vanishes and the system is named the "non-interacting" system. On the other hand, when $\lambda>0$ the electron-electron interaction will have to be calculated, and eq. (A.26) will be written as

$$\hat{H}_\lambda = \hat{T} + \hat{V}_{ext}^\lambda + \lambda \hat{V}_{eff} \quad (\text{A.27})$$

$$\hat{V}_{ext}^\lambda + \hat{V}_{eff} = \int \frac{\rho(\vec{r}_2)}{r_{12}} d\vec{r}_2 + V_{xc}(\vec{r}_1) - \sum_A^M \frac{Z_A}{r_{1A}} \quad (\text{A.28})$$

Hence, using \hat{H}_λ , the energy of the interacting system ($E_{\lambda=1}$) can be calculated as the expectational value of \hat{H}_λ , and will have the following form

$$E_{\lambda=1} = E_{\lambda=0} + \int_0^1 dE_\lambda \quad (\text{A.29})$$

From eq. (A.29) $E_{\lambda=0}$ is known from the "non-interacting" expression of the Kohn-Sham equations, and an expression that introduces the exchange-correlation effect can be obtained for E_λ . This comes from eq. (A.19). eq. (A.29) will then be expressed as

$$E_{\lambda=1} = E_{\lambda=0} + \int_0^1 dE_\lambda \quad (\text{A.30})$$

where

²In a "non-interacting" system, electrons are considered just particles with no interaction between them, so they only feel the attraction to the nuclei. On the other hand, in a fully interacting system, electrons are considered charged fermions, that means, not only they feel a repulsive force between them due to the charge but also a repulsive force due to the Pauli exclusion principle. In a "non-interacting system no exchange-correlation factor is involved.

$$E_{\lambda=0} = -\frac{1}{2}\nabla^2(\vec{r}) + V_{eN}(\vec{r}) \quad (\text{A.31})$$

$$-\frac{1}{2}\nabla^2(\vec{r}) = T_s \quad (\text{A.32})$$

$$V_{eN}(\vec{r}) = \int \rho(\vec{r}') V_s d(\vec{r}') \quad (\text{A.33})$$

$$V_s = \frac{Z_A}{R_A - \vec{r}} \quad (\text{A.34})$$

and

$$E_\lambda = \int \rho(\vec{r}) \hat{V}_{eff}^\lambda d\vec{r} + \frac{1}{2} \int \int \frac{\rho(\vec{r}_1)\rho(\vec{r}_2)}{r_{12}} d\vec{r}_1 d\vec{r}_2 + \frac{1}{2} \int \int \frac{\rho(\vec{r}_1) h_{xc}^\lambda(\vec{r}_1, \vec{r}_2)}{r_{12}} d\vec{r}_1 d\vec{r}_2 d\lambda \quad (\text{A.35})$$

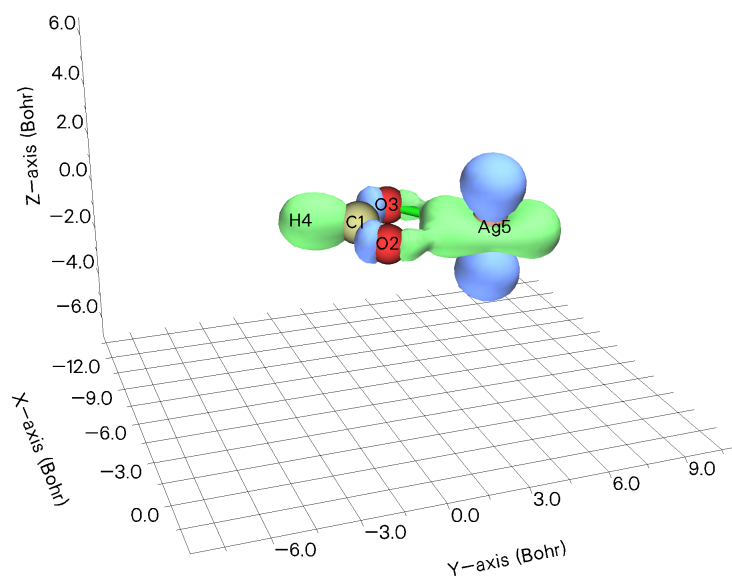
Combining all expressions in eq. (A.30), eq. (A.31) and eq. (A.35) $E_\lambda = 1$ is expressed as

$$E_\lambda = T_s + \int \rho(\vec{r}) \hat{V}_{eff}^\lambda d\vec{r} + \frac{1}{2} \int \int \frac{\rho(\vec{r}_1)\rho(\vec{r}_2)}{r_{12}} d\vec{r}_1 d\vec{r}_2 + \frac{1}{2} \int \int \frac{\rho(\vec{r}_1) h_{xc}^\lambda(\vec{r}_1, \vec{r}_2)}{r_{12}} d\vec{r}_1 d\vec{r}_2 d\lambda \quad (\text{A.36})$$

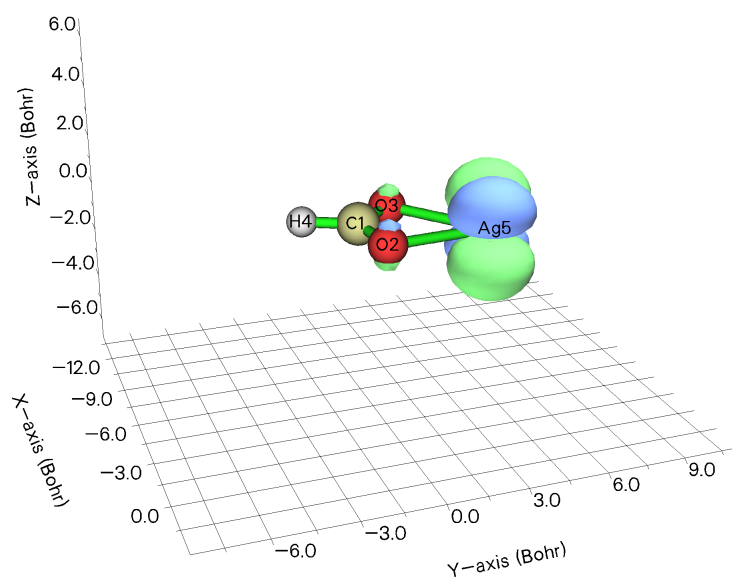
The description of the electron kinetic energy (T) by the "non-interacting" system expression T_s , brings a lot of simplicity to the calculations, but of course, there is a price to pay and this is the introduction of the exchange-correlation hole as a function of λ . Notwithstanding, this approach is extensively used and hybrid functionals are present and preferred for a lot of quantum chemistry calculations.

A.5 QMMM orbital interaction analysis

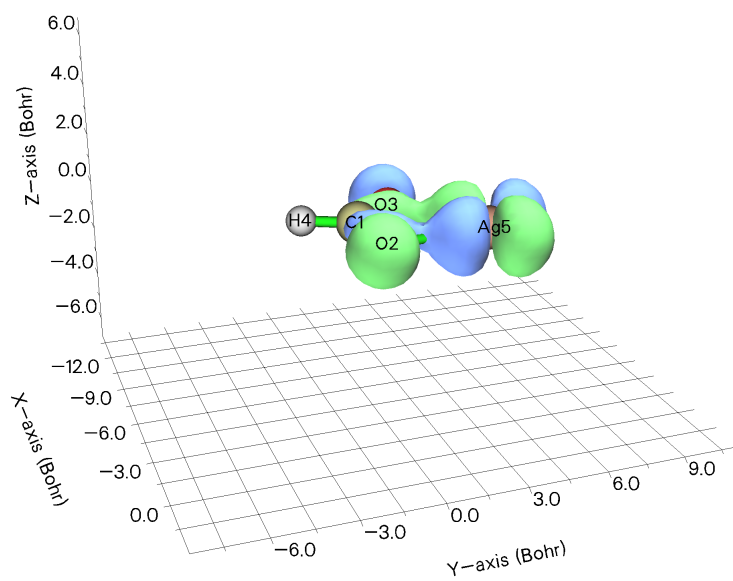
The final configuration of the geometry optimization and of the QM simulations are shown with the calculated isosurface of the valance molecular orbitals.



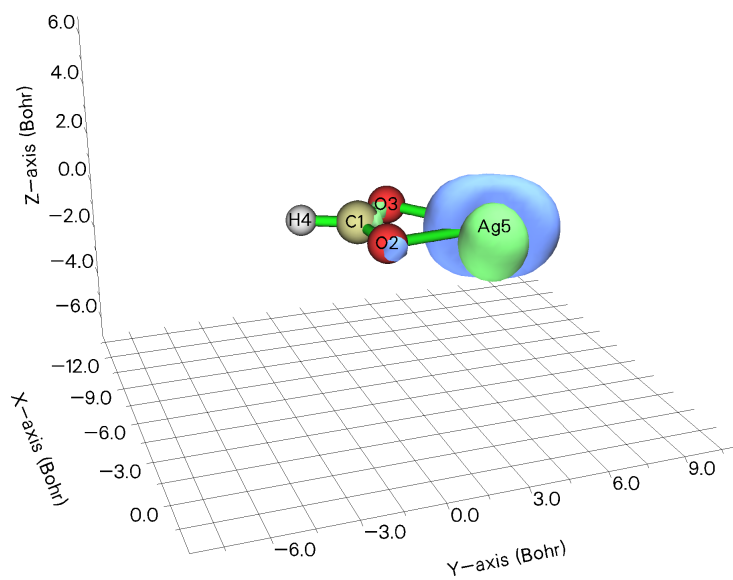
(a)



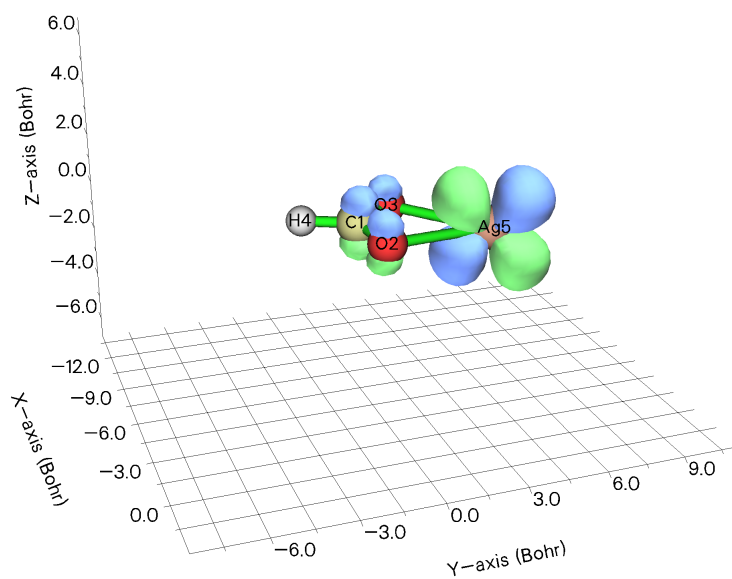
(b)



(c)

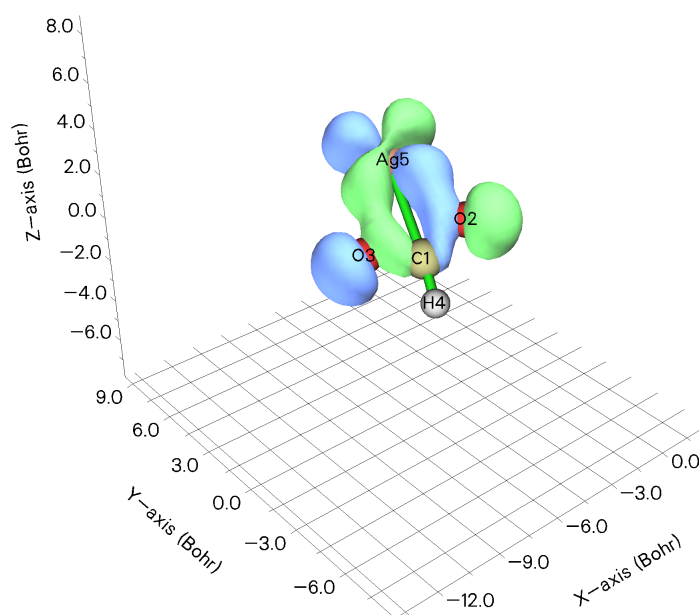


(d)

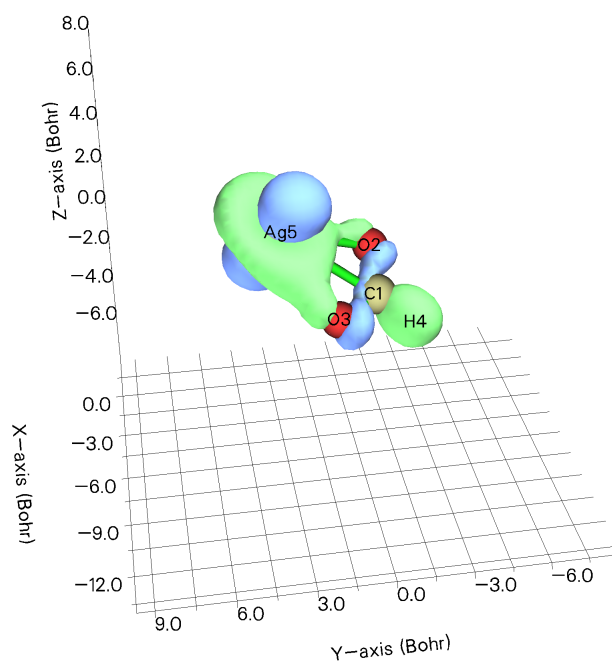


(e)

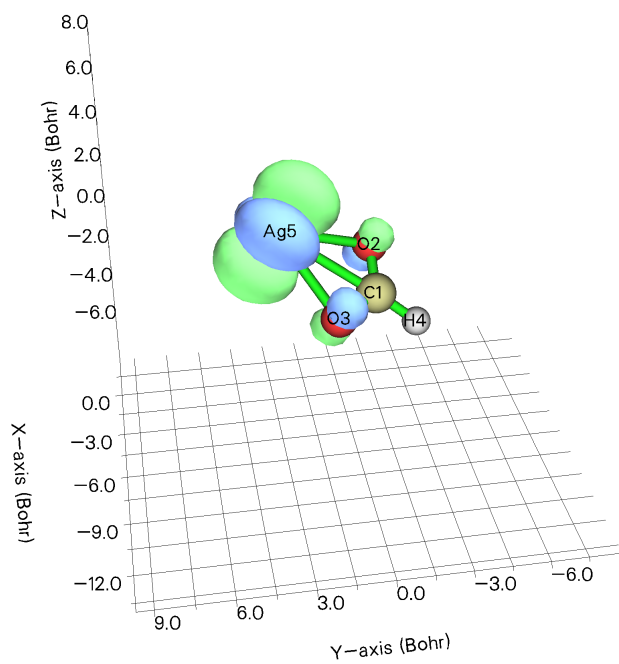
Figure A.2: Representation of the molecular orbitals corresponding to the five d orbitals from the silver cation. The calculations are done in the geometry optimized structure. In order, the respective d orbitals are: a) z^2 , b) xz , c) xy , d) $x^2 - y^2$ and e) yz



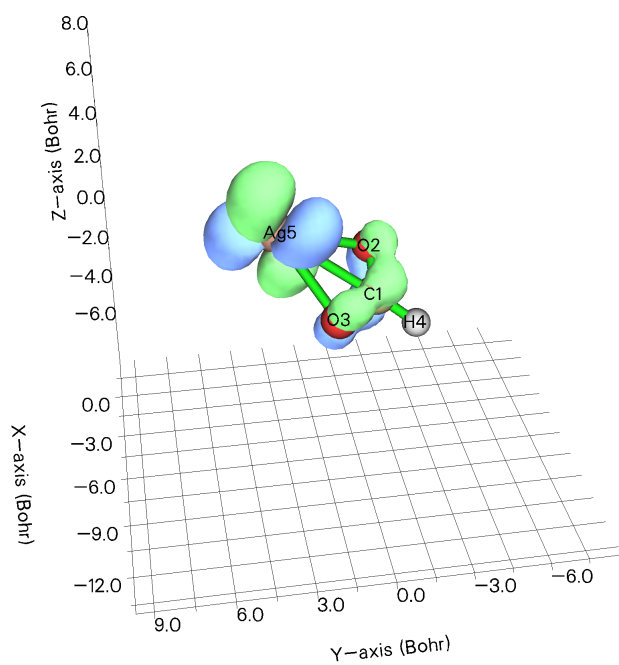
(a)



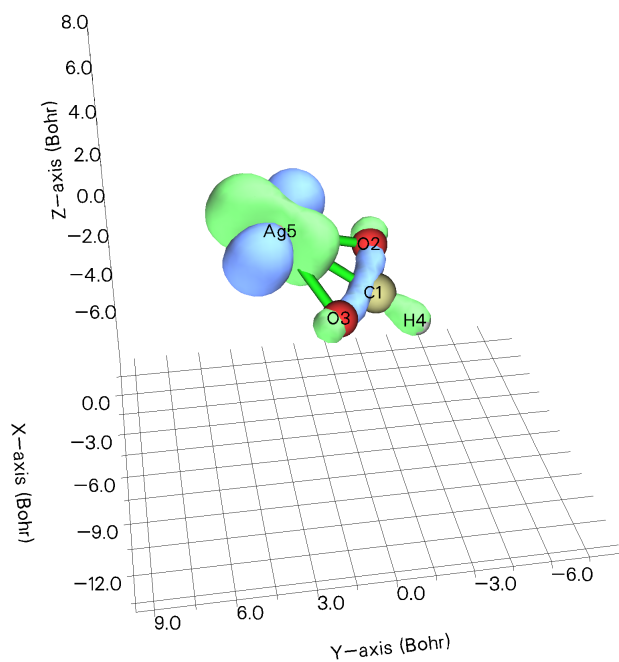
(b)



(c)

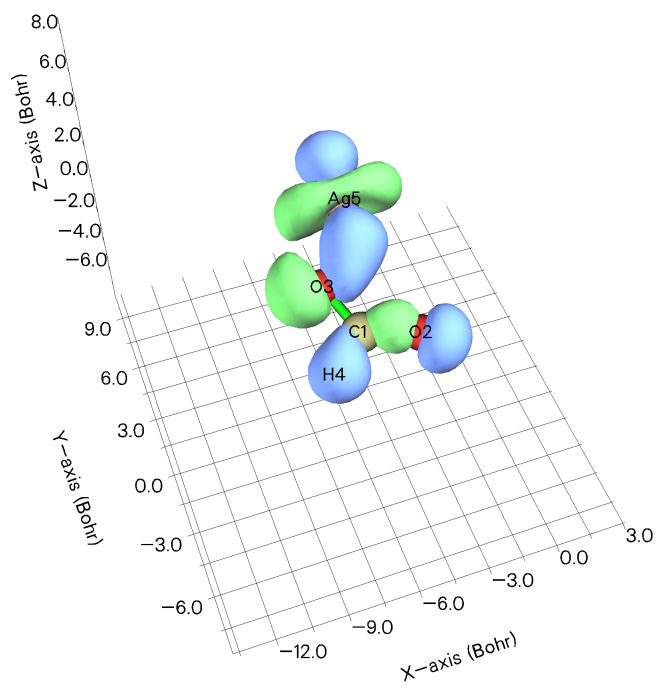


(d)

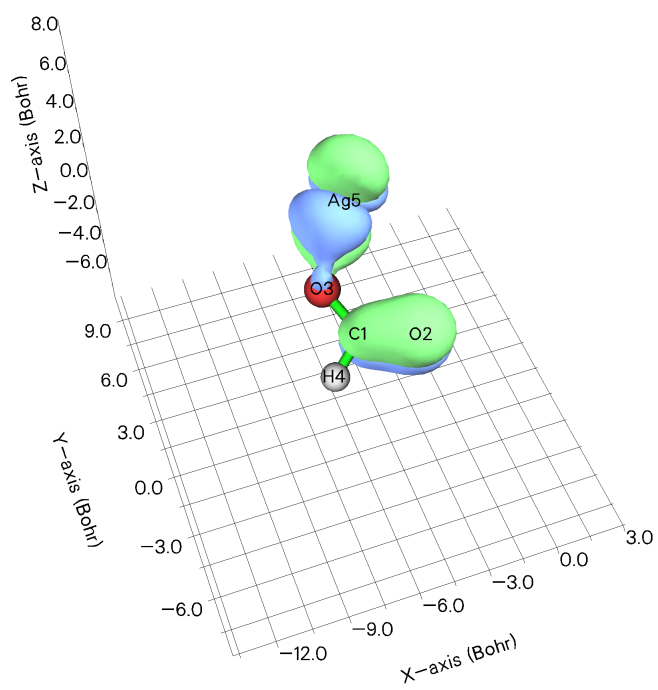


(e)

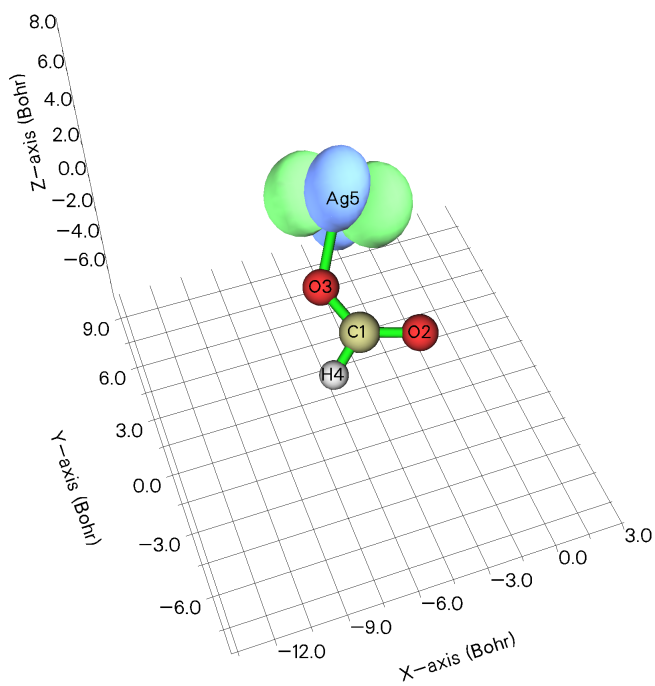
Figure A.3: Representation of the molecular orbitals corresponding to the five d orbitals from the silver cation. The calculations are done in the final structure obtained after the QM simulation in vacuum. In order, the respective d orbitals are: a) $x^2 - y^2$, b) z^2 , c) xz , d) yz and e) xy



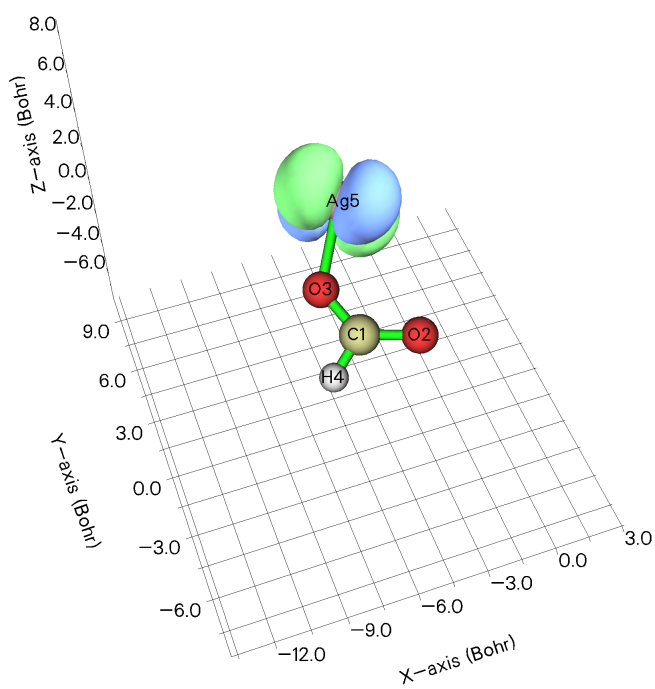
(a)



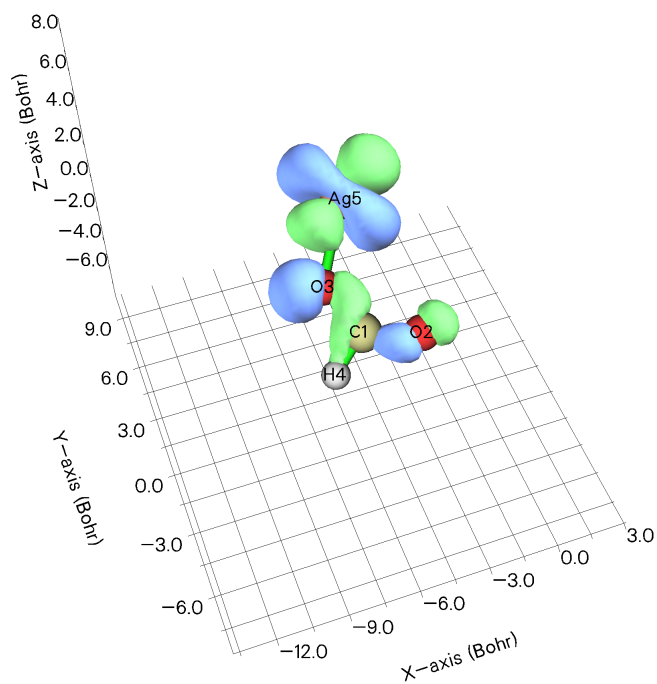
(b)



(c)

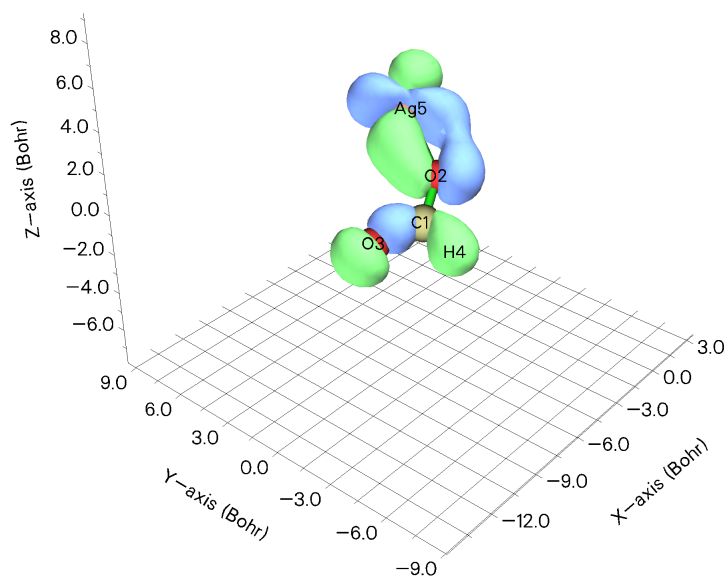


(d)

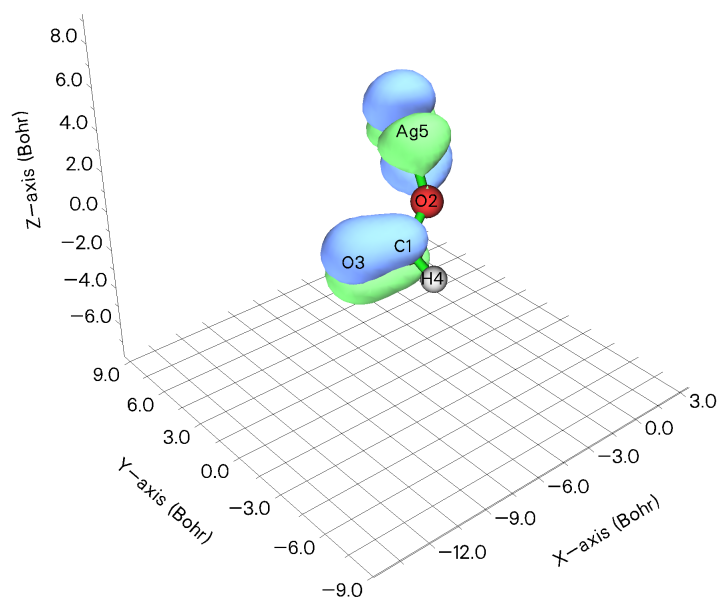


(e)

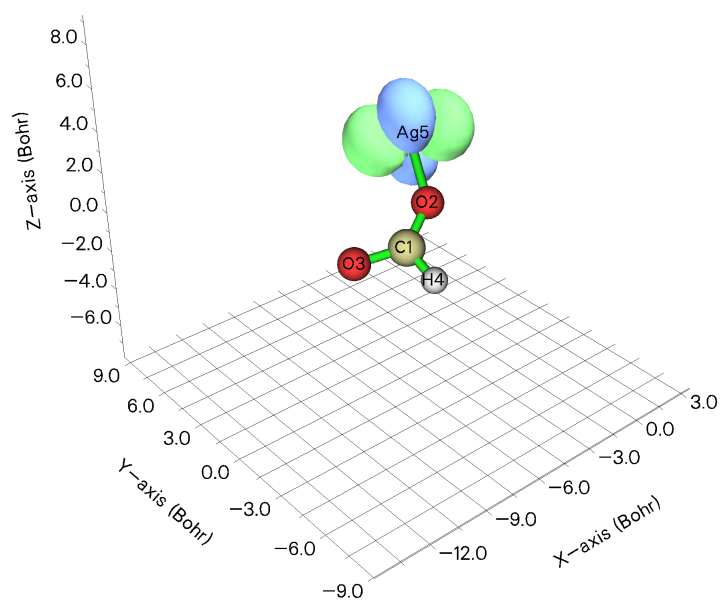
Figure A.4: Representation of the molecular orbitals corresponding to the five d orbitals from the silver cation. The calculations are done in the structure obtained after the QM simulations done in water as solvent. In order, the respective d orbitals are: a) $x^2 - y^2$, b) z^2 , c) xz , d) yz and e) xy



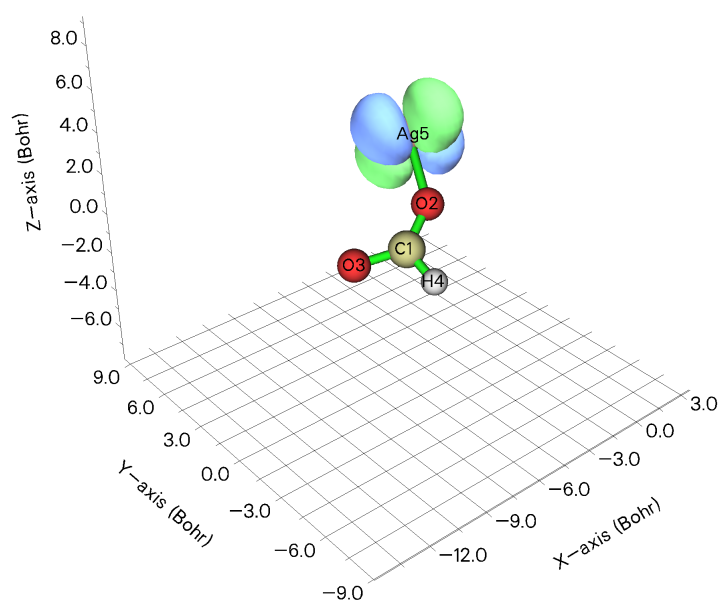
(a)



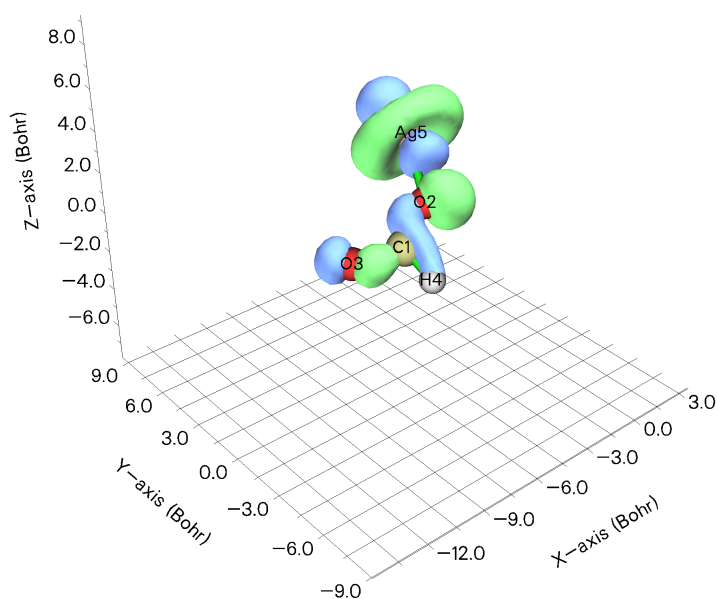
(b)



(c)



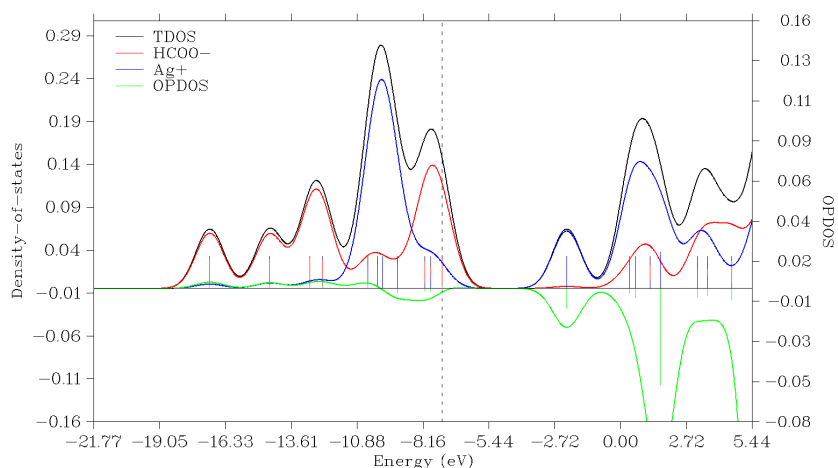
(d)



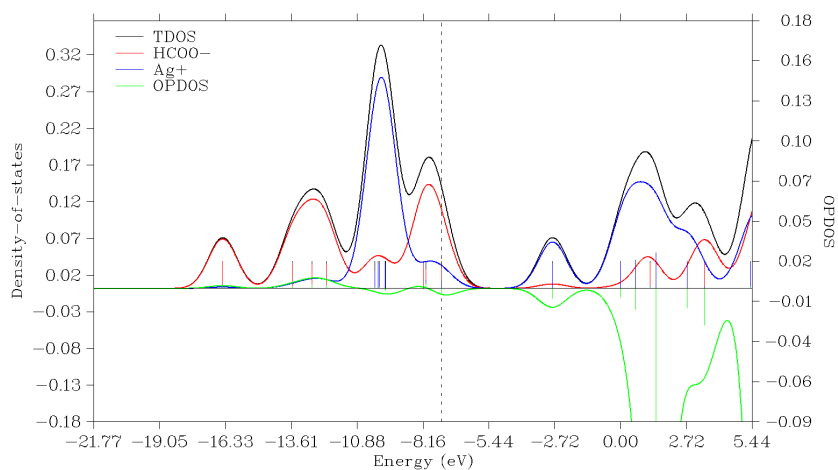
(e)

Figure A.5: Representation of the molecular orbitals corresponding to the five d orbitals from the silver cation. The calculations are done in the structure obtained after the QM simulations done in 30% acetonitrile as solvent. In order, the respective d orbitals are: a) $x^2 - y^2$, b) z^2 , c) xz , d) yz and e) xy

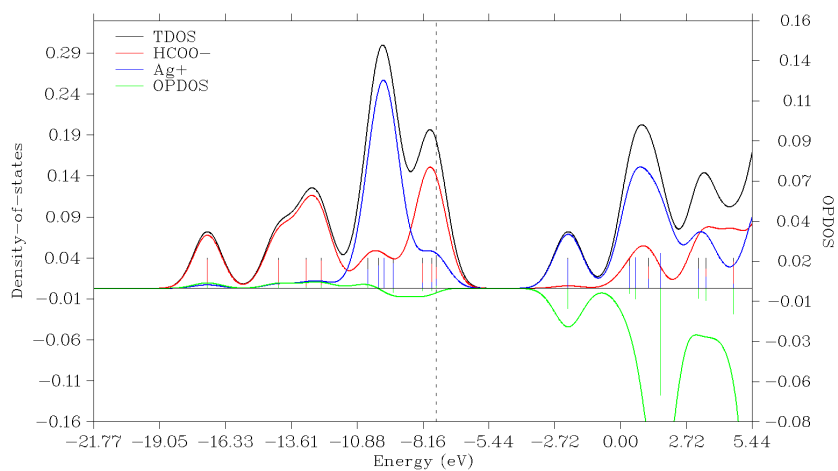
TDOS, PDOS and OPDOS were plotted for each one of the simulations. The results were rather similar in any of the scenarios not showing any kind of overlapping either bonding or anti-bonding. The results can be seen in



(a)



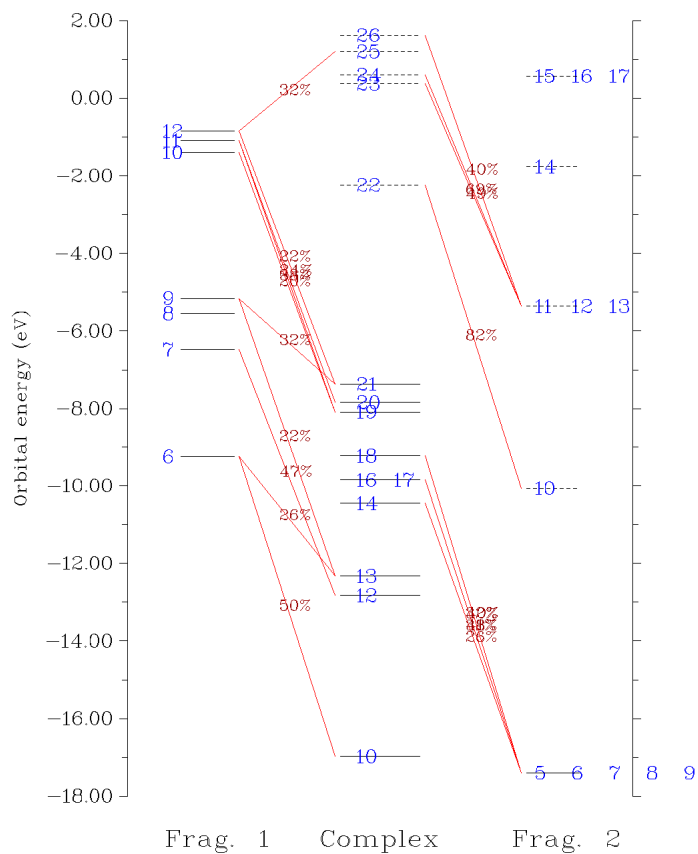
(b)



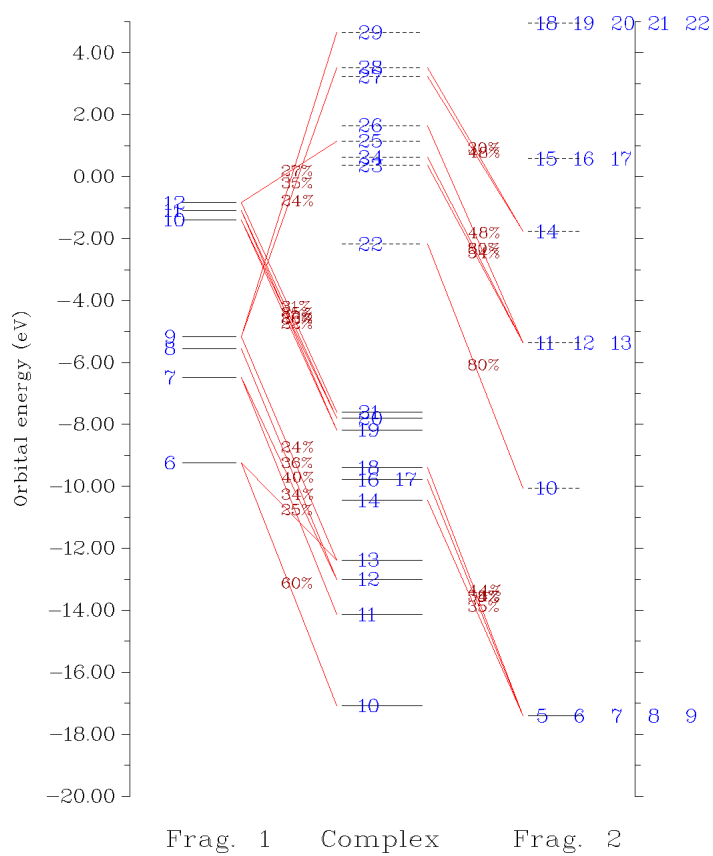
(c)

Figure A.6: TPDOS, PDOS and OPDOS of the final configuration obtained through QMMM simulations. a) correspond to the simulation with acetonitrile as solvent, b) to the simulation in vacuum and c) to the simulation with water as solvent.

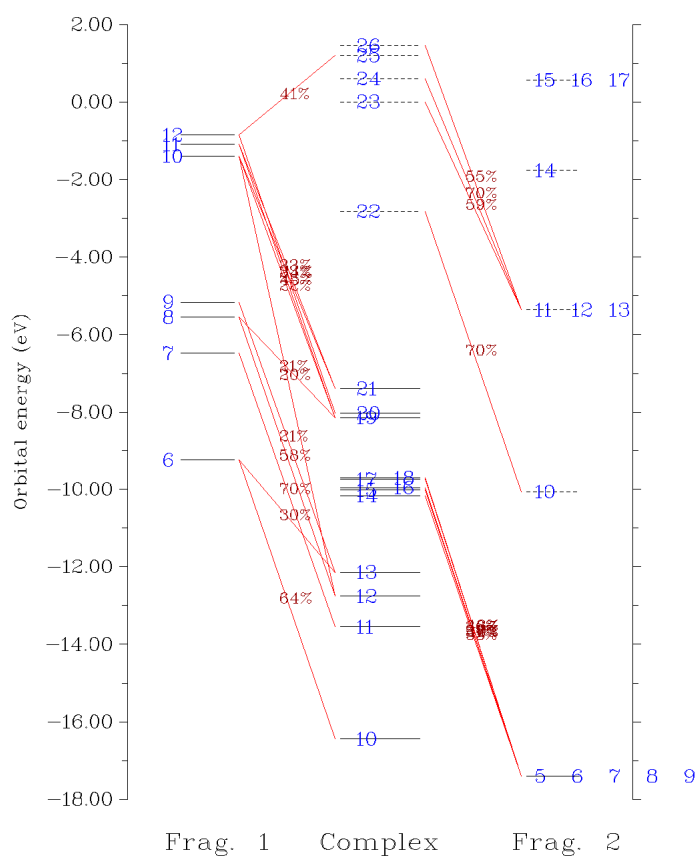
The interaction diagram was also calculated for each of the simulations. The same parameters as the results analyzed in section 3.2 (only consider overlap if the molecular orbital is composed by at least a 20% of the respective atomic orbital).



(a)



(b)



(c)

Figure A.7: Interaction diagram of each of the simulations. As can be seen there is no molecular orbital composed by more than a 20% of its respective atomic orbitals. Fragment 1 describes the carboxylic acid and Fragment 2 describes the silver cation. a) corresponds to the simulations performed with acetonitrile and water respectively as solvent and b) to the simulations performed in vacuum.

A.6 GFD3E synthesis worklist

Worklist for Synthesis C:\Documents and Settings\User\My Documents\gfdfd\gfdfdfe.syn

Thursday, September 24, 2020 13:06:44 Version 1.4.4.31

Sequence: Gly Phe Asp Phe Asp Phe Glu

N-terminal Fmoc protected, C-terminal acid

Monoisotopic molecular weight: 1097.402

Theoretical yield: 0.150 millimole

Time for synthesis: 16 Hours 1 Minute

Maximum reactor contents: 4.0 ml, use 10 ml reactor

PV not used

Maximum amino acid vial contents: 3.0 ml, use 15 ml vials

Multitask mode: Just in time

Simple wizard used: Single coupling, Swell, Final DCM wash

UV monitoring used

Resin data:

Substitution: 0.570 mmoles/gram, Quantity: 0.263 grams, Preloaded with Glu, Deprotect before first coupling

Fluid Allocation

Bottle	Fluid	Molarity	millilitres
External 1	DMF	na	1722.0
External 2		na	0.0
External 3		na	0.0
Internal 4		na	0.0
Internal 5		na	0.0
Internal 6	DCM	na	15.0
Internal 7	DIEA 1.0 M	1.00	21.0
Internal 8	HBTU 0.48 M	0.48	21.0
Internal 9	Piperidine 25%	na	90.0

(Add allowance for fluid to cover inlet filters in bottles)

When UV monitoring is used fluid usage is calculated for maximum deprotections

Fit vial 0 with new cap for initial probe wash

Sequence Data

Sequence Data

Carousel	Vial	Seq	Protected amino acid		Quantity	Protocol
		0	C terminal			initial
1	1	1	Glu attached to resin	No vial	0 mg	-
1	2	2	Fmoc-Phe-OH	powder	291 mg	standard cycle
1	3	3	Fmoc-Asp(OtBu)-OH	powder	309 mg	standard cycle
1	4	4	Fmoc-Phe-OH	powder	291 mg	standard cycle
1	5	5	Fmoc-Asp(OtBu)-OH	powder	309 mg	standard cycle
1	6	6	Fmoc-Phe-OH	powder	291 mg	standard cycle
1	7	7	Fmoc-Gly-OH	powder	223 mg	standard cycle
		8	N terminal			final

Consolidated amino acid vial data

Protected amino acid		Quantity	No. of vials	Carousel 1	Carousel 2
Glu attached to resin	powder	0 mg	1	1	
Fmoc-Phe-OH	powder	291 mg	3	2,4,6	
Fmoc-Asp(OtBu)-OH	powder	309 mg	2	3,5	
Fmoc-Gly-OH	powder	223 mg	1	7	

Figure A.8: Worklist for the synthesis of GFD3E.

A.7 AFM images of quartz wafers used for solid state fluorescence spectroscopy

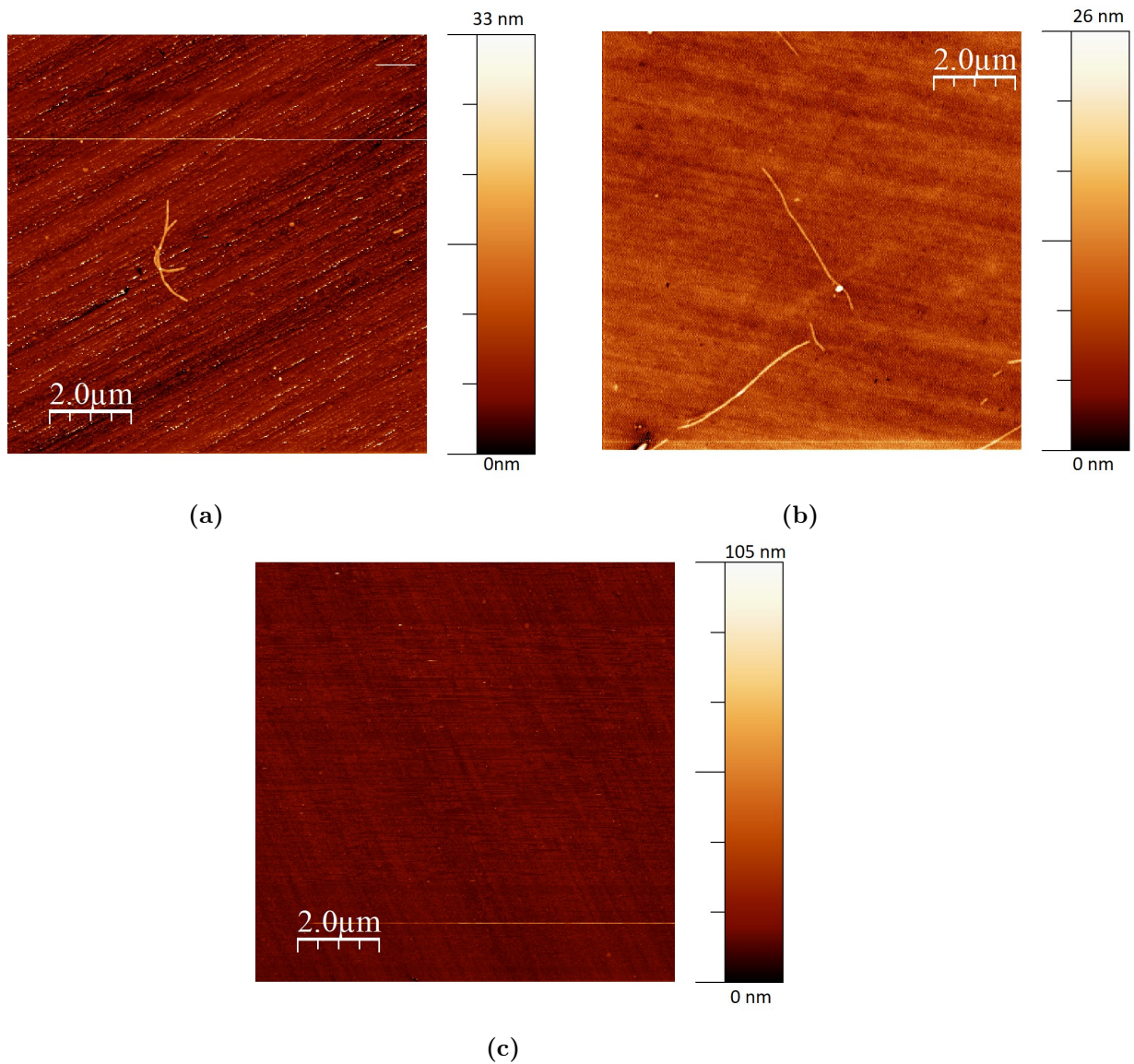


Figure A.9: AFM images of samples analyzed by solid substrate on the fluorescence spectroscopy. These images are representative of the coverage of the substrate. Images at random position of the substrate were taken, until no fibers were found in three straight pictures. Images have been modified in order to facilitate the interpretation. Samples dilutions are a) 0.5 mM, b) 0.75 mM and c) 1mM.

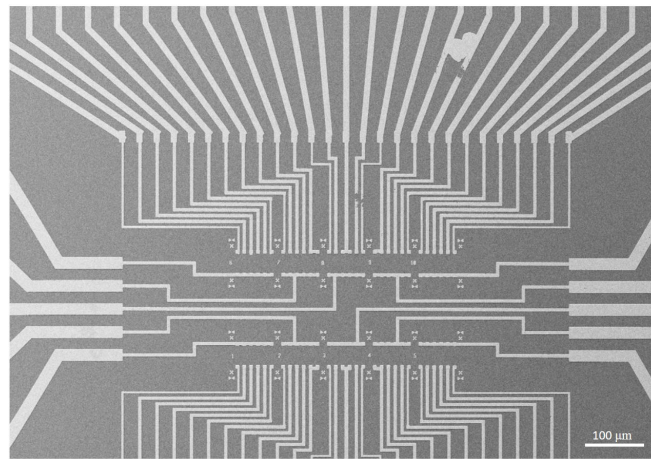
A.8 Device preparation

The wafers upon which the nanoelectrodes will be printed were prepared in two different methods to assess the performance of either. The methods were quite similar, although some reagents differed from one to another as well as some treatments performed on them. This small changes will be noted along the procedure.

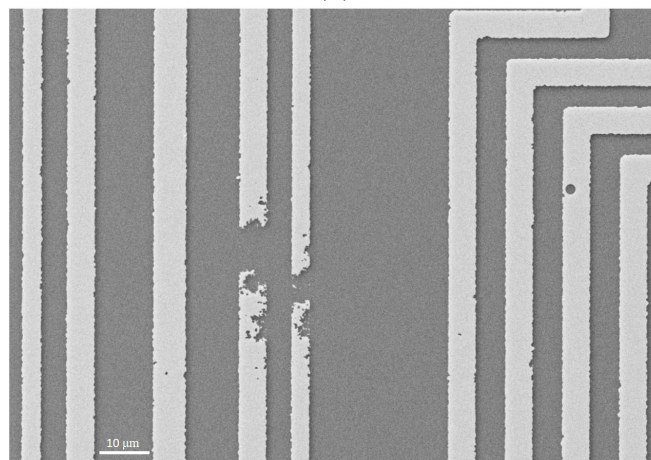
Circular silica wafers were washed in a heated solution of hydrogen peroxyde and sulfuric acid in a ration of 1:3 (v/v) fig. A.10 (for method 1) or in pure nitric fuming acid fig. A.11 (for method 2) and put in a sonication bath for three minutes. Subsequently, the wafers were rinsed in water MiliQ quality in a sonication bath for another minute and dried with nitrogen gas. Prior to photoresist precipitation, the wafers were baked in a heated plate for one minute at 115°C to ensure that no water molecules were left on the surface. A thin layer of hexamethyldisilazane (HMDS) was deposited on the surface of the wafers in a POLOS SPIN105i spin coater. This solution of HMDS is used to create a more hydrophobic surface for a better adhesion of the photoresist. The wafers were again baked for one minute at 150°C after the photoresist coating to dry the hydrophobic layer. Subsequently a layer of 1.5 μm of photoresist was spin-coated on the wafers. Both coating steps were performed at 4000 rpm. Once the coating process finished, the wafers were backed at 115°C in order to help the adhesion of the photoresist layer. Solutions of HMDS and photoresist were filtered using a hydrophobic polytetrafluorethylen filter in order to avoid the placement of any possible aggregates on the surface of the wafers that could harm further steps [fig. A.11].

Wafers were now ready to print the electrodes pattern on them. To expose the wafers, a MA6 Mask aligner with vacuum contact exposure was used. Different exposure times were tested (5.2, 5.6 and 6 seconds) in order to find that of better performance. The light intensity was set to $30\text{mW}/\text{cm}^2$ for all the attempts. Prior to metal deposition, wafers were introduced in a solution of Microposit developer and ionised water to a ratio of 1:2 for 1 minute and 30 seconds as developing step to rinse-off the photoresist that had not been exposed. After being rinsed with deionised water and dried with nitrogen gas, the wafers were treated in a 320 PC Reactive Ion etching where a O_2 descum plasma process was performed for 1 minute (this treatment was performed only for method 1). For the wafers prepared by method 2, a UV/ozone treatment was performed. After this treatment, a 5 nm layer of chromium beneath a layer of 80 nm of gold was deposited on the coarse pattern. Metal deposition was performed in a Cryofox Explorer 600. Afterwards, a lift-off step was performed in order to remove the unwanted metal. Wafers were introduced in a solution of photoresist remover and were left in the solution overnight.

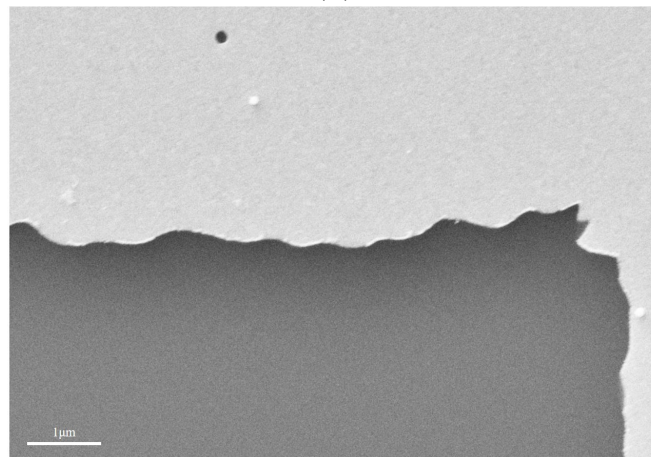
In order to cut the circular wafers in small 10 by 10 mm squares a DAD321 Disco Automatic Dicing Saw used with a diamond blade. Prior to dicing, a photoresist layer was spin-coated onto the wafers to reduce possible damage on the pattern. Once the wafers were diced, this layer was removed by first introducing the squared wafers in acetone in a sonication bath and later in a solution of ammonia, hydrogen peroxyde and deionised water (at a ratio of 1:1:1.5 respectively) for either one minute or two steps of 30 seconds. A visual assessment was done in a microscope to study the performance of the dicing step.



(a)

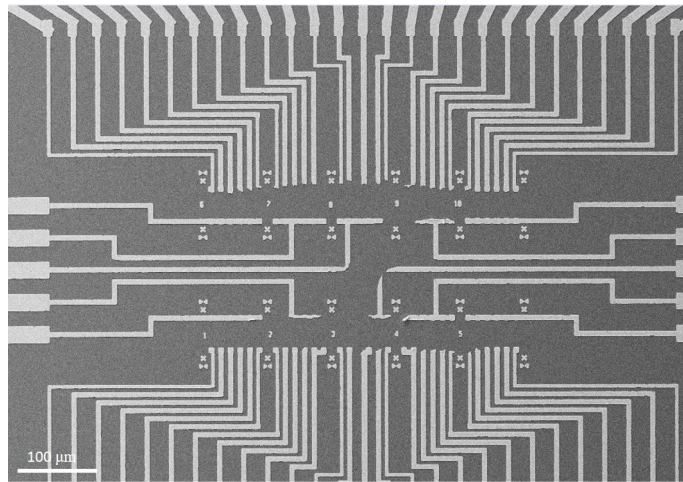


(b)

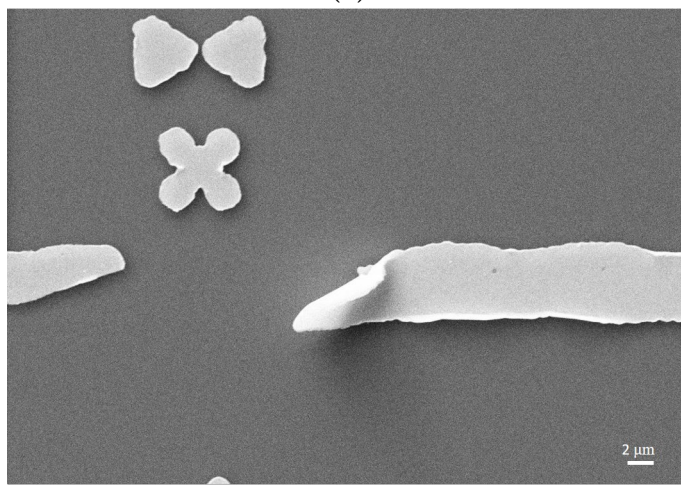


(c)

Figure A.10: SEM images of the coarse grain pattern after being washed with an ammonia solution. The pattern is broken due to the removal of the photoresist beneath the evaporated metal. HMDS and photoresist solutions were not filtered.



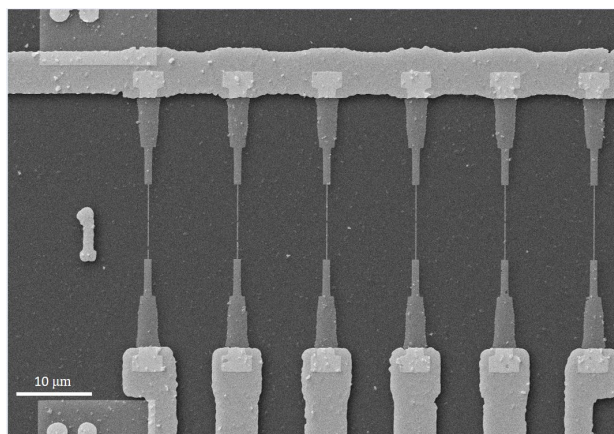
(a)



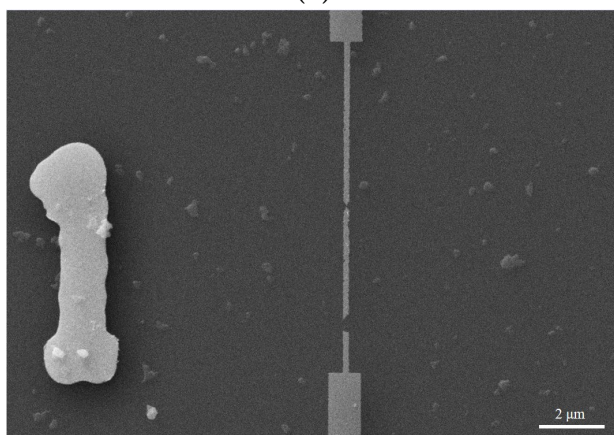
(b)

Figure A.11: SEM images of the coarse grain pattern after being washed with nitric fuming acid. HMDS and photoresist solutions were filtered with a hydrophobic filter.

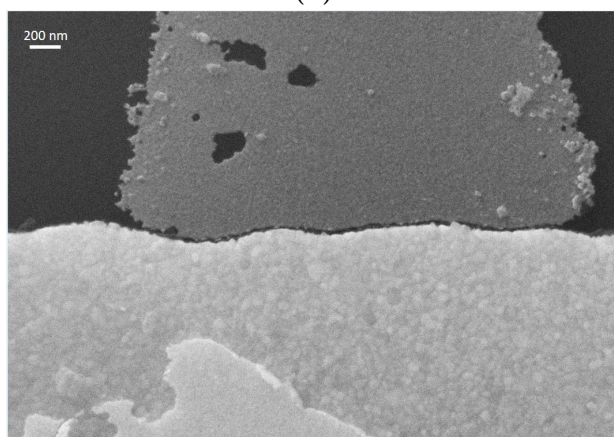
Although some of the details can already be appreciated in the SEM images just after metal evaporation, the flaws and the photoresist aggregates can be better seen once electron beam lithography had been performed on the wafers. These small photoresist aggregates can be predominantly seen in the samples that were prepared without filtering the HMDS nor the photoresist solution [fig. A.12], but can also be seen on the samples where the solutions were filtered (although in less quantity) [fig. A.13].



(a)

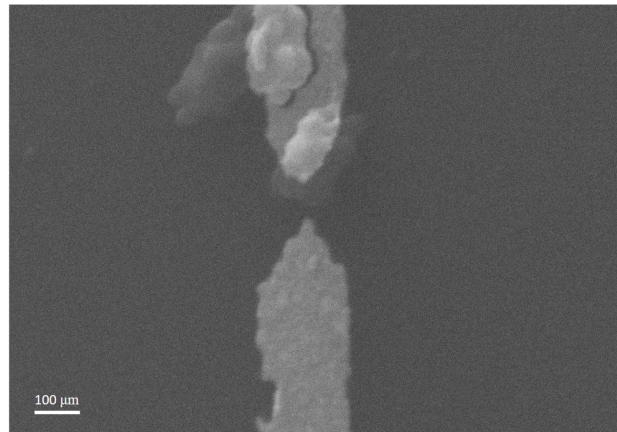


(b)

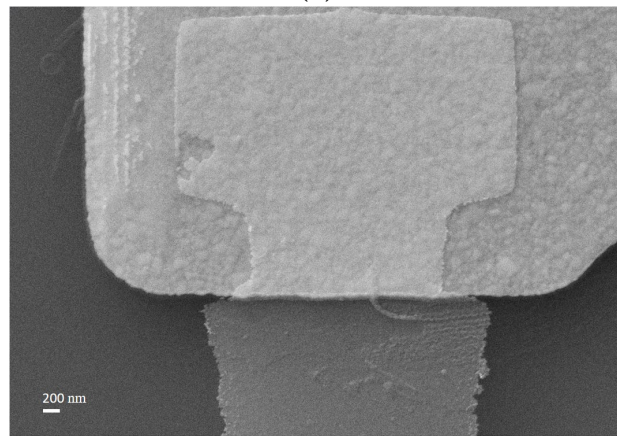


(c)

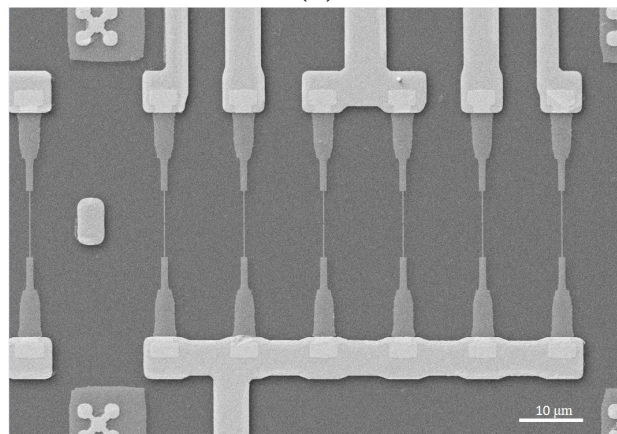
Figure A.12: SEM images of the E-beam pattern after Au evaporation had been performed. Small aggregates of organic molecules can be seen that can harm the performance of the electrodes.



(a)



(b)



(c)

Figure A.13: SEM images of the E-beam pattern after Au evaporation had been performed. These wafers were cleaned with nitric acid after being cut in the dicing saw in order to remove the aggregates.

The parameters used regarding rpm and exposure energies and times are in accordance to the ones proposed by the manufacturer. Exposure doses were slightly higher since the thickness of the photoresist layer was expected to be larger than the one expected (1.5 μm) [95]. Despite following all the manufacturer instructions, photoresist aggregates were seen in samples prepared by either methods. The presence of these aggregates indicated a thin layer of organic compounds remaining on the wafers

even after their were introduced into the developer solution. This thin layer removed the partially or totally the metal pattern printed. Different methods were attempted in order to eliminate this organic layer. While aggregates were successfully removed by filtering the HMDS and Microposit solution prior to deposition, the thin organic layer remained after either of the methods tried. Both photoresist solution were used after the expiration date what can lead to the decomposition of the photoactive substances. The loss of photoinitiator in positive resists can be spotted by observing whether bubbles are formed. N_2 is released from the photoinitiator and dissolves into the photoresist solution causing the bubbles. Plasma etching, specially using oxygen with reactive ions is commonly used to the formation of high resolution profiles [96]. Here, this strategy was used to eliminate such organic layer. Due to the instrument was out of service, only one attempt was done and it did not succeed in removing it. UV/ozone treatment is also commonly used for surface cleaning of organic molecules [97]. This strategy was also attempted with little success since the deposited metal on the coarse pattern was removed after the lift-off process.

If functional nanoelectrodes are to be built the removal of such organic layer and the aggregates is key for the achievement of a high resolution. Plasma etching should be tried again with a reduction of the photoresist layer. This can be achieved by longer exposure times. UV/ozone treatment was not sufficient for the removal of the organic contamination.